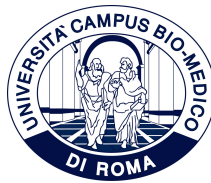


On inertial sensing of motion: validation, calibration and tracking with wearable devices in robotics and biomedical applications



A thesis presented by

Luca Ricci

in partial fulfillment of the requirements for the degree of
Doctor of Philosophy
in Biomedical Engineering

Università Campus Bio-Medico di Roma
School of Engineering

Coordinator
Prof. G. Iannello

Supervisor
Prof. E. Guglielmelli

Co-Supervisor
Dr. D. Formica

Feb 2015

Contents

Contents	2
List of Figures	4
List of Tables	5
I Background	11
1 Introduction	13
1.1 The wearable era of inertial sensors	13
1.2 Research challenges	14
1.3 Research goals	16
1.4 Contributions	16
1.5 Outline of the thesis	18
2 Inertial measurement unit	19
2.1 Sensors	19
2.2 Calibration	28
2.3 Inertial motion tracking	31
2.4 Available instrumentation	36
3 Statistical estimation	39
3.1 Introduction	39
3.2 A cost function interpretation	41
3.3 A general probabilistic framework for estimation	44

II Research focus	47
4 Validating accuracy of inertial orientation tracking	49
4.1 Problem formulation	49
4.2 Materials and Methods	52
4.3 Metric on SO3 space	60
4.4 Results	60
4.5 Discussion	66
5 Single device for navigating an omnidirectional wheeled robot	75
5.1 Problem formulation	75
5.2 Materials and methods	79
5.3 Sensor fusion	90
5.4 Results	96
5.5 Discussion	99
6 Multiple devices for upper body motion capture in children	105
6.1 Inertial motion capture of children in daily-life scenarios	105
6.2 Materials and Methods	107
6.3 Results	117
6.4 Discussions	127
7 Concluding remarks	131
7.1 Conclusions	131
7.2 Future works	133
7.3 Peer-reviewed journals	135
7.4 Peer-reviewed conferences	136
7.5 National and international conferences	136
A Quaternion algebra	137
A.1 Basic properties of quaternions	137
A.2 Spherical Linear Interpolation	138
B Orientation conversion	139
B.1 Axis and angles	139
B.2 Rotation matrix	139
B.3 Euler angles	140

Bibliography	141
---------------------	------------

List of Figures

1.1	Brief evolution of inertial sensors	15
2.1	MEMS accelerometer	20
2.2	MEMS gyroscopes	22
2.3	MEMS magnetometer	25
2.4	Allan Variance	28
2.5	IMU calibration (ellipsoid fitting)	30
2.6	Inertial navigation	31
2.7	Inertial navigation reference frames	32
4.1	Experimental setup for accuracy validation	53
4.2	Robot disturbances on magnetic field	57
4.3	Static accuracy results	61
4.4	Static convergence results	62
4.5	Dynamic accuracy results (absolute)	64
4.6	Dynamic accuracy results (relative)	65
4.7	Trends in amplitude and bandwidth dependence (Kalman Filter) .	70
4.8	Trends in amplitude and bandwidth dependence (Complementary Filter)	71
5.1	The omnidirectional wheel and its applications	76
5.2	Experimental omnidirectional robotic platform	80
5.3	Model of the experimental platform	81
5.4	Markers' cluster configuration	84
5.5	Sensors information rates	89
5.6	Sensor fusion scheme for robot calibration	93
5.7	Sensor fusion scheme for robot's velocity estimation	93
5.8	Sensor fusion scheme for robot navigation	95

5.9	Sequence of robotic platform's movements	97
5.10	Kinematic parameters estimation result (optical reference)	98
5.11	Estimate of robot velocities (optical reference)	99
5.12	Estimate of wheels' angular velocities (optical reference)	100
5.13	Kinematic parameters estimation result (IMU)	101
5.14	Estimate of robot velocities (IMU)	102
5.15	Multiple minima cost function	103
6.1	Experimental setup for human motion capture	109
6.2	Definition of reference frames on human body	111
6.3	Example of calibration protocol's functional movements	112
6.4	Configuration of simulated and real angular velocity data in space	119
6.5	Comparison of axis extraction methods	120
6.6	Comparison of frame calibration methods	121
6.7	Typical convergent behaviour of the regression algorithm	123
6.8	Comparison of functional axis estimates	124
6.9	Typical outcome of the kinematic calibration procedure	125
6.10	Human kinematic chain implementation	126
6.11	An application for real-time human motion capture	127

List of Tables

2.1	Available IMUs specifications	37
4.1	Matrix of excitations for dynamic accuracy validation: row-wise are amplitudes in and column-wise are frequencies	56
4.2	Dynamic accuracy results (absolute)	72
4.3	Dynamic accuracy results (relative)	73
5.1	Standard deviations of sensors measurements	91

6.1	Reliability index computed from the calibration protocol	122
-----	--	-----

Abstract

The class of inertial sensors have undergone a revolution in the last decades. From the technological standpoint, this transformation has brought a dramatic reduction in both size and cost after the advent of micromachined electro-mechanical system (MEMS) technology. From an application standpoint, they have spread out from the traditional aeronautical and naval fields (i.e. inertial navigation systems) to a plethora of new and different areas, e.g. automotive, robotics and clinical to name a few. Nowadays, inertial sensors are available on the market as system on chip (SoC) that are small enough to be unobtrusively attached to any system, including the human body, and their presence in consumer products has become a commonplace (e.g. in smartphones) virtually electing them as a top player in the upcoming *wearables* era.

However, miniaturized inertial sensors come with inherent limitations that are mainly found in the reduced performance in terms of noise. Besides, the more recently introduced applications are still far from being mature (e.g. human motion capture). As a consequence, there is a number of open challenges related to the use of this evolved technology and that spans from signal processing and sensor fusion of noisy measurements to the improvement of existing algorithms and expansion to unexplored areas of application.

The main objective of this work is to improve the state of the art with respect to some of these challenges. First, the dissertation examines the problem of establishing accuracy in measuring orientation for current inertial sensor fusion algorithms. A methodology based on the use of a robotic manipulator is presented and confidence intervals of static and dynamic performance are established. Then, the thesis discusses the problems of calibration and motion tracking with inertial sensors in two different contexts of application, i.e. ground mobile robotics and biomedical research.

Regarding robotics, the setup explored in this thesis consisted of an omnidirectional wheeled platform, equipped with an inertial sensor and wheel encoders, intended to be navigated in a industrial

setting. While this class of robots has superior mobility characteristics, difficulties related to their autonomous navigation prevent their widespread use in the research and industry. To overcome this limitation, a number of sensor fusion problems are presented and a solution proposed in order to self calibrate the platform and ameliorate accuracy of the navigation through robustness, e.g. against wheel slippage.

Regarding the biomedical application, inertial sensors were used to reconstruct the motion of children (6-7 years old) in a daily life scenario. To this purpose, a novel calibration procedure and algorithms are introduced to improve accuracy over state of the art methods. The outcome of this research will permit the investigation of motor disorders at an earlier stage of development than is currently possible (e.g. for the case of autism spectrum disorder).

Notation

In this thesis, scalars are denoted with lowercase letters (a), geometric vectors with bold lowercase letters (\mathbf{v}), quaternions with bold lowercase letters (\mathbf{q}), and matrices with bold capitals (\mathbf{M}). Left superscripts denote in which frame a quantity is resolved, e.g. the vector \mathbf{p} in frame A will be ${}^A\mathbf{p}$. Subscripts are generally used for annotations and indexing (\mathbf{p}_k) and multiple subscripts are separated by a comma ($\mathbf{p}_{k,i}$). In some cases, subscripts are also used to indicate points in space, e.g. $\mathbf{d}_{A,B}$ is the vector from point A to point B, or quantities computed between different reference frames, e.g. $\omega_{A,B}$ is the angular velocity of frame A with respect to frame B. The complete list of mathematical operators and sets used in this thesis is reported in the table below.

Symbol	Meaning
a	Scalar in \mathbb{R}
\mathbf{v}	Vector quantity in \mathbb{R}^3 (if not differently specified)
\mathbf{M}	Matrix with m -rows and n -columns in $\mathbb{R}^{m \times n}$
$\tilde{\mathbf{v}}$	Augmented vector in \mathbb{Q}
${}^C\mathbf{d}_{A,B}$	vector from point A to B referred to frame C
${}^{AB}\mathbf{q}$	quaternion rotating from the B -frame to the A -frame
${}^{AB}R$	Rotation matrix from the B -frame to the A -frame
\mathbb{R}	Real number space
$SO(3)$	3-dimensional special orthogonal group
\mathbb{Q}	4-dimensional quaternion space
\mathbb{Q}_1	Unit norm quaternion space
\otimes	Quaternion product
$\ \cdot\ _2$	2-norm operator
$\arg \max$	Maximizing argument
$\arg \min$	Minimizing argument
$\mathbf{vec}(\cdot)$	Matrix vectorization operator

Tesi di dottorato in Ingegneria biomedica, di Luca Ricci,
discussa presso l'Università Campus Bio-Medico di Roma in data 11/06/2015.
La disseminazione e la riproduzione di questo documento sono consentite per scopi di didattica e ricerca,
a condizione che ne venga citata la fonte.

Part I

Background

Tesi di dottorato in Ingegneria biomedica, di Luca Ricci,
discussa presso l'Università Campus Bio-Medico di Roma in data 11/06/2015.
La disseminazione e la riproduzione di questo documento sono consentite per scopi di didattica e ricerca,
a condizione che ne venga citata la fonte.

Chapter 1

Introduction

This chapter provides an introduction to the thesis by briefly explaining the context in which the present work has been carried out, exposing the current challenges and stating the goals of this research. In this setting, the main contributions are presented and the organization of the material is outlined.

1.1 The wearable era of inertial sensors

The technology to sense inertial forces acting on an object in order to determine its dynamic behaviour has been available to mankind for about a century. Despite the history of inertial sensors is relatively short, it is remarkable to observe that most of the ingredients necessary for building accelerometer or gyroscope sensors, such as fine mechanics and precise spring technologies, were available from the late Middle Ages. Originally, accelerometers were developed for being used as switches (e.g. for bomb detonators) in World War I. Instead, gyroscopes invention dates back to the early 1800 with the mechanical gyroscope designed by Johann Gottfried Friedrich von Bohnenberger and later, in the early 1900s, when they were patented for use on ships (i.e. the “gyrocompass”) [Schell, 2005]. The first commercial accelerometer intended for a broader use was fabricated in the early 1920s as the result of the reasearch by McCollum and Peters [McCollum and Peters, 1924] while the foundation of modern devices was laid in the 1940s, with the discovery of the piezoelectric and piezoresistive principles. Instead, for gyroscopes the 1960s are the years when modern types of devices were introduced, such as the vibrating-string gyro [Quick, 1964], the tuning-fork gyro [Hunt and Hobbs, 1964] and the vibrating-shell resonator and

whose principles of operation are found in current micro electro mechanical devices (MEMS). Beginning from the 1990s, advancements in MEMS technology, originally driven by the new requirements of the automotive industry (e.g. the 50g accelerometer was used in the airbag ignition mechanism), have lead to dramatic reduction in cost, weight and dimension. The consequence of this trend is that inertial sensors, originating in traditional fields such as naval and aeronautical have become widespread in many other fields of application and are even fostering creation of new fields as shown in Figure1.1.

Nowadays inertial sensors are available on the market as integrated system on chip (SoC) solutions with a dimension $< 0.5 \text{ cm}^3$ at a cost of few Euros. They have become an ubiquitous technology that can be found in cars, smart-phones or gaming consoles. Furthermore, with the incoming era of *wearables*, it is expected that they will be found with increasing frequency actually worn on the human body. Aside from the decreased dimensions, inertial sensors are becoming “smarter”, as the performance of embedded algorithms is improving, and are turning into the “silver bullet” technology for motion tracking [Welch and Foxlin, 2002].

1.2 Research challenges

The appearance on the market of miniaturized MEMS inertial sensors, that are so small and power efficient to be virtually attachable to any system (human body included) has expanded their potential for use in a myriad of applications. On the one hand, some of these applications are in the traditional fields (e.g. inertial navigation). On the other hand, nearly every month a new application is created and checked for commercial attractiveness and realizability.

However, the use of MEMS inertial sensors introduces new problems to be researched. Differently from gimballed inertial platforms (i.e. the bulkier and expensive devices used in inertial navigation systems), a common disadvantage of the miniaturized systems are the errors corresponding to this method of measurement. Consider for instance the gyroscope: the bias stability error of a consumer MEMS gyroscope and a gimballed gyroscope can have differences amounting to an order of magnitude of 7 [Fitzgerald, 2013]. As a consequence, the algorithms originally developed for motion tracking with the more performing platform generally won't work with this new class of inertial devices. A common problem is that motion information is computed by time integration of inertial quantities (i.e. acceleration and angular velocity), which, in absence of proper compensation strategies can lead to unbounded estimation errors.

1.2. RESEARCH CHALLENGES

15

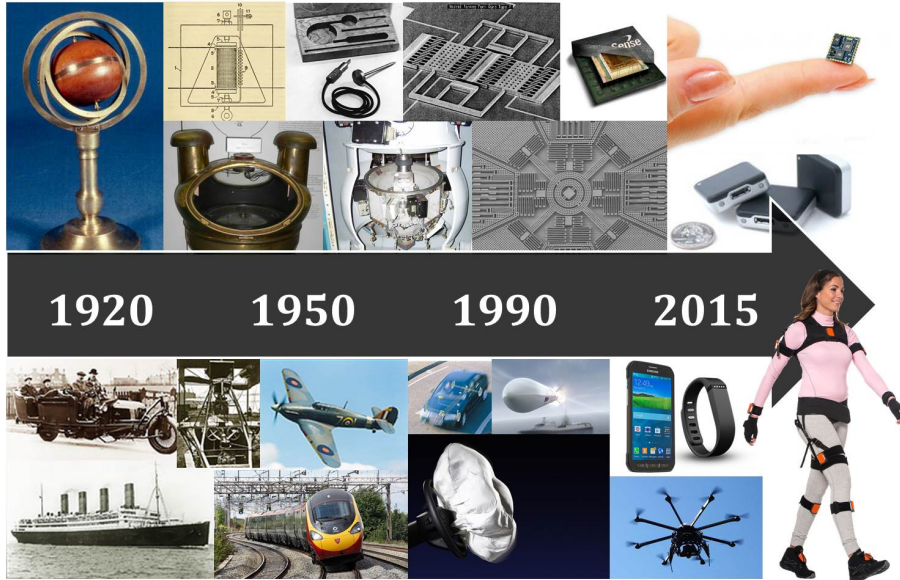


Figure 1.1: The evolution of inertial sensors from the technological (on top the arrow) and field of application (under the arrow) perspectives.

In that sense, the research challenge consists of solving signal processing and sensor fusion problems. This necessitates the development of adequate error models for MEMS inertial sensing which may be used to achieve sufficient measurements accuracy with the implementation of appropriate filtering techniques. Furthermore, the performance in terms of accuracy achievable with the use of this class of devices and related to some of the newest applications (e.g. human joint angles measurement) is still poorly investigated and an open research question.

Besides issues related to performance of the sensors and the tracking algorithms, there is vibrant activity in the research for improvement and extension of recently introduced application, e.g. in the biomedical and robotics fields. For instance, motivated by the salient role of quantifying motor functions in clinical practice and as a potential early marker for some neurodevelopmental disorders (i.e. autistic spectrum disorder [von Hofsten and Rosander, 2012]), a branch of inertial sensors' research is committed towards the development of

wearable assessment tools. In the field of robotics, inertial sensors are commonplace on different type of platforms, e.g. on unmanned aerial vehicles (UAVs) [Aragus, 2015], unmanned ground vehicles (UGVs) [Sahoo, 2015] or and autonomous underwater vehicles (AUV) [VanMiddlesworth, 2015]. One of the major inertial sensors' related research challenges here is the development of information fusion algorithms to achieve autonomous navigation.

1.3 Research goals

The main objective of this work is to improve the state of the art on inertial sensors' research.

The first goal is to determine accuracy in orientation tracking achievable with recent inertial sensor fusion algorithms, as an accurate measurement of orientation is the starting point for human motion capture with wearable inertial sensors. This topic has often been overlooked in the related literature and the absence of baseline data makes it difficult to compare algorithms' performance and understand the sources of error.

The second and third goals are related to extending the use of the inertial sensors within the field of robotics and of the biomedical applications. The second goal pertains the autonomous navigation and self calibration of an omnidirectional wheeled mobile platform. Though this class of ground mobile robots have superior mobility characteristics, its use in ground robotics' research is limited due to inherent issues related to its autonomous navigation. The aim of the research work on this topic is to demonstrate how major limitations of this kind of robots can be overcome by using an inertial sensor module. The third goal is regards achieving inertial motion reconstruction of children in a daily life scenario. This is a topic of increasing interest in the research community due to, on the one side, the high portability recently available with the introduction of wearable inertial motion capture systems and, on the other side, the relevance of the scientific quests (e.g. fine grained quantification of motor disorders, investigation of the role of communicative gestures in child development). A challenge here is the adaptation and improvement of existing procedures on adults for an use with children.

1.4 Contributions

The main contribution of this thesis are related to the research goals above mentioned and are briefly stated in order of appearance:

1.4. CONTRIBUTIONS

17

- An extensive validation of static and dynamic accuracy in tracking the orientation using state of the art sensor fusion algorithms with wearable inertial measurement unit (IMU) devices. Both the absolute and the relative accuracy are assessed under controlled and repeatable conditions. The outcome of the validation is a reliable set of confidence intervals for the accuracy in orientation tracking;
- An investigation on the impact of different variables (i.e. amplitudes and bandwidth of motion, sensor fusion algorithm, magnetic field perturbation) on the accuracy performance in orientation tracking with IMUs;
- A method for the automatic calibration of systematic sources of errors affecting the odometry of an omnidirectional wheeled robotic platform. The measurements considered by the proposed algorithm are those available from wheel encoders and an IMU, which is rigidly attached to the robot;
- A method for the autonomous dead reckoning navigation of an omnidirectional wheeled robotic platform. The navigation is formulated as a statistical sensor fusion algorithm having as input the measurements from wheel encoders and the onboard IMU. The algorithm for navigation is demonstrated to be robust against unmodelled error sources (e.g. wheel slippage);
- The design of a protocol allowing for the identification of axis of reference from functional movements adapted to the experimental use with typically developing children (6–7 yr). The protocol is devised to be used with wearable IMUs and permits the collection of redundant set of functional axis information, describing the movements of the thorax and the upper limbs. It has been extensively validated over a population of 40 children;
- A procedure for extracting axis of rotation or reference axis respectively from gyroscope and accelerometer datasets. The method doesn't need any data pre processing (e.g. segmentation) and provides a numerical quantification of the reliability of the computed axis;
- A methodology for accurate calibration of IMU sensors' body and human body's reference frames through nonlinear regression. Eventually, the procedure allows for the reconstruction of human motion given a kinematic model and the orientation measured by the IMUs.

1.5 Outline of the thesis

This dissertation is organized in two parts. Part I contains the background material to the research focus presented in Part II.

In Part I, chapter 2 introduces the inertial measurement unit (IMU) which is the main sensing element that has been used in the presented research and the principal source of information to the developed algorithms. The aim of the chapter is to provide a comprehensive overview of the different aspects related to the use of this device, which include sensor modelling, calibration and motion tracking. The present material is by no means extensive of the topic, however references for further readings are provided in the text.

In Part II, chapter 3 discusses the topic of performance in orientation tracking accuracy for state of the art sensor fusion algorithms, targeting the applications related to human motion reconstruction. This topic is mostly overlooked in the related literature and no baseline data were available at the time of this writing. The experimental setup presented comprised a robotic arm to which a set of IMUs are rigidly fixed and a protocol was devised to investigate static and dynamic performance. Alongside reporting reliable confidence intervals for accuracy, the chapter is concluded with a critical discussion of results and experienced criticalities. In chapter 4, the area of robotics application is discussed particularly surrounding the problem of autonomously navigating an omnidirectional wheeled robot in an industrial setting. The chapter introduces the use of an IMU as additional onboard sensor providing helpful information to the task at hand. It is demonstrated, through properly developed sensor fusion algorithms, how this approach is an effective solution to the task. Furthermore, the proposed approach comes with significant advantages, i.e. robustness against unmodelled disturbances (e.g. wheel slippage) and automatic calibration of the systematic sources of error associated to the robotic platform. The next chapter 5 pertains to the area of biomedical applications and explores the use of multiple IMUs to reconstruct motion in children (6-7 yr). The problem of calibrating inertial sensor and biomechanical reference frames is introduced and a novel procedure to solve it is provided. A calibration protocol suitable for an use with children is presented together with the data processing techniques developed. The outcome of the procedure is then used in combination with the sensor fusion algorithms, analysed in chapter 3, in order to achieve the human motion reconstruction. Finally, Chapter 6 concludes the dissertation and gives description of future work.

Chapter 2

Inertial measurement unit

In this work of thesis, the inertial measurement unit (commonly referred as IMU) is used throughout the text as the main source of information to the developed algorithms and methodologies. This chapter aims to provide the reader with a background of the working principles, models and motion tracking techniques related to this device. The first section discusses the individual sensing elements comprising an IMU, focusing on the models and the principal deterministic and stochastic sources of error. Next, commonly employed methodologies for in-field calibration of an IMU (removal of deterministic errors) are reviewed. The concluding section introduces the reader to the physical principles and techniques used in order to achieve motion reconstruction, pointing out criticalities and limitations.

2.1 Sensors

The term IMU identifies a class of devices that comprise a pair of tri-axial accelerometer and gyroscope in a single sensing unit. A fully equipped IMU often includes a tri-axial magnetometer in the same package. In this latter case, either the terms magnetic-IMU or M-IMU are found in the literature. An IMU is capable of measuring inertial quantities (acceleration and angular velocity) and the magnetic flux vector which, in absence of magnetic field perturbations, measures the direction of the Earth magnetic north. Since the advent of Micro Electro-Mechanical Systems (MEMS) technology in the 1990s, a trend in miniaturization of the individual sensor components (driven by the requirements of the automotive and aeronautical industries) have brought to

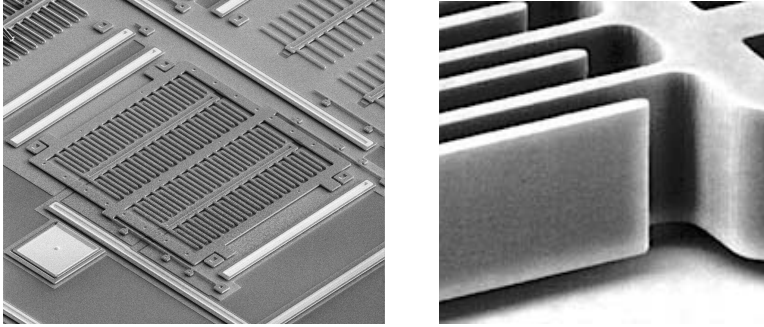


Figure 2.1: The figure reports the mechanical structure of a MEMS accelerometer (left) and a close-up view of the comb structured capacitor (right) used for measuring the displacement of the suspended mass.

market devices that are cheap ($< 100\$$ per axis) and so small ($< 2 \text{ mm}^3$) to be integrated on single System on Chip (SoC) solution. On the one hand, current IMUs are low cost, small and lightweight and are now suitable for a number of new applications (e.g. wearable devices). On the other hand, although the performance of MEMS is improving rapidly, compared to traditional technology, MEMS devices have reduced performance in terms of accuracy and bias stability. In this section the working principle and the mathematical models used to describe the behaviour of MEMS sensors included in an IMU are reported. The following material is by no means exhaustive of the topic and further details can be found in [Titterton and Weston, 2005, J.Woodman, 2009, Mohd-Yasin et al., 2009].

MEMS accelerometers

Micro-machined silicon accelerometers use the same principles as mechanical and solid state sensors. The core of the sensor consists of a suspended proof mass connected to the sensor's basement through a spring-damper link. When the sensor is subjected to an acceleration along its sensitive axis the proof mass tends to resist the change in movement owing to its own inertia. As a result, the mass moves relatively to the sensor housing in the opposite direction than is the direction of the movement. The displacement is proportional to the applied force and can be measured as a variation in capacitance of a properly designed capacitor element, as shown in Figure 2.1.

Sensor model

An accelerometer measures the external specific force (\mathbf{f}) applied to its proof mass, which is related to acceleration (\mathbf{a}) as:

$$\mathbf{a} = \mathbf{f} + \mathbf{g} \quad (2.1)$$

where \mathbf{g} denotes the Earth's gravitational acceleration. The specific force (also called proper acceleration) is defined as the difference between the instantaneous acceleration and free fall. In case of free fall, the accelerometer output will be zero. Instead, in static condition at Earth surface, specific force is heading vertically up with respect to gravitational acceleration vector and has the same magnitude. The following measurement model can be used to describe output from a tri-axial accelerometer (\mathbf{y}_a):

$$\mathbf{y}_a = \mathbf{M}_a \mathbf{S}_a \mathbf{f} + \mathbf{b}_a + \mathbf{n}_a = \mathbf{K}_a \mathbf{f} + \mathbf{b}_a + \mathbf{n}_a \quad (2.2)$$

where \mathbf{f} is the input specific force on the sensitive axes and \mathbf{n}_a is the stochastic measurement noise. The terms associated with the major sources of deterministic errors, considered by this model, are:

Fixed bias (\mathbf{b}_a): This term represents the displacement from zero on the accelerometer output when the sensed specific force (\mathbf{f}) is null. The magnitude of the bias term is independent of any motion to which the accelerometer may be subjected and it is commonly expressed as a fraction of the full scale of the accelerometer.

Scale-factor (\mathbf{S}_a): This term relates sensor output (\mathbf{y}_a) to the physical quantity to be measured (\mathbf{f}) and is modelled as a diagonal matrix:

$$\mathbf{S}_a = \begin{pmatrix} s_{xx} & & \\ & s_{yy} & \\ & & s_{zz} \end{pmatrix} \quad (2.3)$$

where s_{ij} is the sensitivity of the i -th axis accelerometer to the accelerations in the j -th axis.

Cross-coupling (\mathbf{M}_a): this term compensates for errors that arise as a result of manufacturing imperfections which determine non-orthogonality of the sensor axes. It can be modelled with a matrix:

$$\mathbf{M}_a = \begin{pmatrix} 1 & \alpha_{xy} & \alpha_{xz} \\ \alpha_{yx} & 1 & \alpha_{yz} \\ \alpha_{zx} & \alpha_{zy} & 1 \end{pmatrix} \quad (2.4)$$

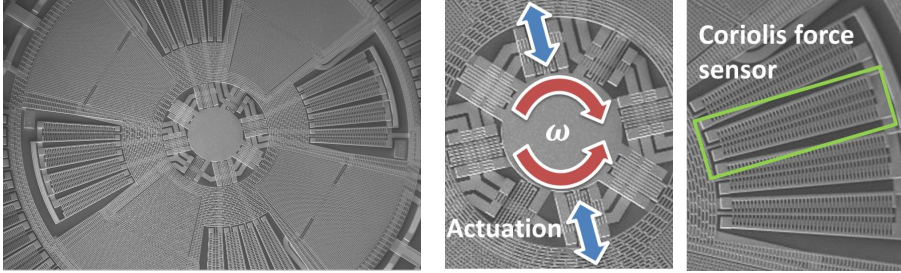


Figure 2.2: The figure reports the mechanical structure of a MEMS gyroscope (on the left). The actuation mechanism (on the center) keeps the proof mass in the center in vibration, such that angular velocities applied along the sensitive axis generate a Coriolis force measurable with capacitive sensors (on the right).

where α_{ij} denotes the rotation of the sensor i -th axis about the j -th axis in order to align with the sensor reference frame (i.e. the sensor housing). Cross-coupling is at the origin of hysteretic behaviour of accelerometer readings, as described in [Ang and Khoo, 2004]

The scale factor matrix and cross-coupling matrix are usually coupled in a single, full gain matrix (\mathbf{K}_a), as reported in the last equality of (2.2) and both the gain matrix and the bias vector are temperature dependent. Other, minor sources of error are due to non-linearities of sensor response and the supply voltage dependent ratiometric errors.

MEMS gyroscopes

Almost all reported MEMS gyroscopes devices are based on the measurement of the Coriolis force acting on a vibrating structure. When a mass (m) is moving with a linear velocity (\mathbf{v}) and its reference frame is rotated with an angular velocity ($\boldsymbol{\omega}$), a Coriolis force (\mathbf{F}_c) given by the following equation is observed:

$$\mathbf{F}_c = -2m(\boldsymbol{\omega} \times \mathbf{v}) \quad (2.5)$$

When the mass is vibrating, the Coriolis effect induces a secondary, perpendicular vibration that can be measured and related to the angular velocity exerted around the sensitive axis. Vibrating mass gyroscopes are small in dimension (shown in Figure 2.2), but have a higher noise level and are more power hungry

2.1. SENSORS

23

than the other sensors composing an IMU. Though they are still suitable in many battery-powered applications, their consumption limits their use in applications where a long-term monitoring with the use of a very small battery is required.

Sensor model

A gyroscope is a sensor capable of measuring its own angular velocity, or rate-of-turn (ω). A suitable model to describe sensor output (y_g) as a function of applied angular velocity is:

$$y_g = M_g S_g \omega + b_g + d_{g,a} + n_g = K_g \omega + b_g + d_{g,a} + n_g \quad (2.6)$$

where ω is the input angular velocity on the sensitive axes and n_g is the stochastic measurement noise. The other terms included in the model are:

Bias (b_g): This is the most critical source of error in a gyroscope and it results from the contribution of different terms:

$$b_g = b_{FB} + b_{BS} + b_{BR} \quad (2.7)$$

The fixed bias term (b_{FB}) represents the displacement from zero on the output when the input ω is null and it is often modelled as a function of temperature. The *bias repeatability* parameter (b_{BR}) is a random constant that varies for each powerup of the IMU. This is due to a number of effects, including change in the physical properties of the IMU and initial conditions of signal processing. Further, the bias of a MEMS gyroscopes has a stability component, termed *bias stability* (b_{BS}), which will vary during in-run usage due to flicker noise in the electronics, temperature, time and/or mechanical stress on the system. This behaviour is usually modeled as random walk noise. Gyroscope datasheets usually reports how stable the bias is over a certain specified period of time. This value is typically expressed in units of $^\circ/s$ or $^\circ/hr$.

Scale-factor (S_a): This term accounts for errors in the ratio of a change in the output signal to a change in the input angular velocity which is to be measured. The error is typically dependent on the magnitude of the input value and may be expressed as percentages of the measured full scale quantity or simply as a ratio. It is represented as a diagonal matrix:

$$\mathbf{S}_a = \begin{pmatrix} s_{xx} & & \\ & s_{yy} & \\ & & s_{zz} \end{pmatrix} \quad (2.8)$$

where s_{ij} is the sensitivity of the i -th axis accelerometer to the accelerations in the j -th axis.

Cross-coupling (M_g): this term compensates for errors that arise as a result of manufacturing imperfections which determine non-orthogonality of the sensor axes, expressed by the matrix:

$$\mathbf{M}_g = \begin{pmatrix} 1 & \alpha_{xy} & \alpha_{xz} \\ \alpha_{yx} & 1 & \alpha_{yz} \\ \alpha_{zx} & \alpha_{zy} & 1 \end{pmatrix} \quad (2.9)$$

where α_{ij} denotes the rotation of the sensor i -th axis about the j -th axis in order to align with the sensor reference frame.

Acceleration or g-sensitivity ($d_{g,a}$): this term is a minor source of error and it is strongly dependent on the physical structure of the MEMS gyroscope. On Coriolis effect based devices it is primarily due to device mass asymmetry. This effect can be modeled and removed from the measurements and is often included in the IMU signal condition stage before output of the measurements.

Again, the terms \mathbf{S}_g and \mathbf{M}_g are usually grouped in a single, full gain matrix (\mathbf{K}_g), as reported in the last equality of (2.6). Temperature dependence of \mathbf{K}_g is typically negligible. Instead, temperature fluctuations due to changes in the environment and sensor self heating induce significant movement in \mathbf{b}_g . Therefore, most IMUs are equipped with internal temperature sensors which make it possible to correct for temperature induced bias effects.

MEMS magnetometer

Micro-machined magnetometers included in a IMU are based on the physical principle of anisotropic magnetoresistance (AMR) and make use of a common material, permalloy, to act as a magnetometer. The electrical resistance of this specific alloy depends on the angle between the metallization and the direction of current flow which, in turn, depends on the external magnetic field's magnitude and direction. In MEMS magnetometers, multiple arrays of

2.1. SENSORS

25

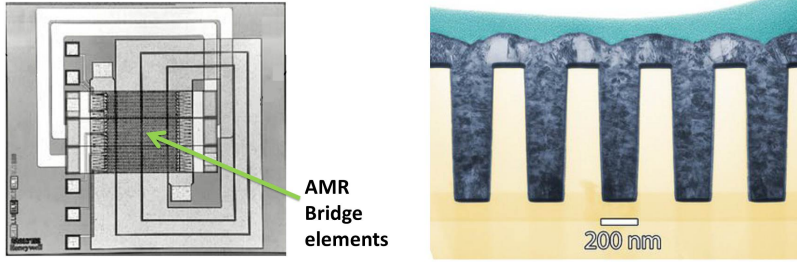


Figure 2.3: The figure shows the layout structure of the Honeywell's HMC1043 anisotropic magnetoresistance MEMS magnetometer (left) and a close-up view (right) of the chemical deposition of the sensitive material (permalloy) on a silicon wafer.

sensing element are organized in a Wheatstone bridge configuration, as shown in Figure 2.3.

Sensor model

A tri-axial magnetometer provides a measure of the local magnetic flux vector. Under unperturbed conditions, it is sensitive to the Earth's magnetic field (magnitude varying from 25 to 65 μT [NGDC,]) and plays the role of a digital compass in the IMU ensemble. A similar model to that describing accelerometers can be used for a tri-axial magnetometer (\mathbf{y}_m):

$$\begin{aligned}\mathbf{y}_m &= \mathbf{M}_m \mathbf{S}_m \mathbf{m}_m + \mathbf{b}_m + \mathbf{n}_m \\ &= \mathbf{K}_m (\mathbf{K}_{si} \mathbf{m}_m - \mathbf{o}_{hi}) + \mathbf{b}_m + \mathbf{n}_m\end{aligned}\quad (2.10)$$

where \mathbf{m}_m is the local magnetix flux acting on the sensor's sensitive axes and \mathbf{n}_n denotes the stochastic noise component. Terms associated with the major sources of systematic errors included in the model, are:

Fixed bias (\mathbf{b}_m): Sensor bias is caused by the Wheatstone bridge offset in AMR magnetometers. Also, sensor bias can be difficult to identify due to the fact that Earth's magnetic field is everywhere and it can easily be locally perturbed.

Scale-factor (\mathbf{S}_a): The magnetic scale factor error accounts for the sensitivity of the magnetic sensor axes response. Due to instrumentation

errors, the level of magnetometer sensitivity varies from one axis to the next. Therefore, it is necessary to define three individual scale factors for each axis, i.e. the entries of a diagonal matrix:

$$\mathbf{S}_g = \begin{pmatrix} s_{xx} & & \\ & s_{yy} & \\ & & s_{zz} \end{pmatrix} \quad (2.11)$$

where s_{ij} is the sensitivity of the i -th axis accelerometer to the accelerations in the j -th axis.

Cross-coupling (\mathbf{M}_g): this term compensates for errors that arise as a result of manufacturing imperfections which determine non-orthogonality of the sensor axes. It is generally expressed by the matrix:

$$\mathbf{M}_g = \begin{pmatrix} 1 & \alpha_{xy} & \alpha_{xz} \\ \alpha_{yx} & 1 & \alpha_{yz} \\ \alpha_{zx} & \alpha_{zy} & 1 \end{pmatrix} \quad (2.12)$$

where α_{ij} denotes the rotation of the sensor i -th axis about the j -th axis in order to align with the sensor reference frame.

Soft iron effect (\mathbf{K}_{si}): Soft iron effects are generated by the interaction of an external magnetic field with the ferromagnetic materials in the vicinity of the sensor. The resulting magnetic field depends on the magnitude and direction of the applied magnetic field with respect to the soft iron material. The soft iron effect is complex, nonlinear and it is also the most common source of error and the most critical parameter to calibrate for the magnetometers.

Hard iron effect (\mathbf{o}_{hi}): Hard iron error relate to a permanent magnet that is fixed in the proximity of the sensor frame. Contrary to the soft iron error, in this case, a permanent magnet generates a constant magnetic field regardless of an externally applied magnetic field. Consequently, even if the applied field is null, the sensor measures this additive magnetic field vector. The hard-iron effect acts directly on sensor bias measurement and it can be compensated much more easily than the soft-iron effect.

Allan Variance

This paragraph introduces a tool that is typically used to compare the performance characteristics of inertial sensors, i.e. the Allan Variance [Allan, 1966].

2.1. SENSORS

27

It is a time-domain method that pertains to the class of cluster analysis techniques and can be viewed as the time domain equivalent of the power spectrum. It can be used to characterize various types of the underlying random processes that give rise to the noise terms on IMU measurements. Given a data recording (\mathbf{y}) containing N samples of an observed stochastic process, sampled every T_s intervals, the following steps should be performed in order to compute its Allan Variance:

1. Divide the dataset into clusters of size $N_c < N/2$, where the number of obtained clusters is $C = \lfloor \frac{N}{N_c} \rfloor$;
2. Compute the average value for each cluster as:

$$\bar{\mathbf{y}}_k = \frac{1}{N_c} \sum_{i=1}^{N_c} \mathbf{y}_{ki} \quad , \quad k = 1, \dots, C \quad (2.13)$$

3. Then, the Allan variance of length N_c is defined as the two point sample variance between cluster averages over time, i.e.:

$$\sigma_A^2(N_c) = \frac{1}{2(C-1)} \sum_{k=1}^{C-1} (\bar{y}_{k+1} - \bar{y}_k)^2 \quad (2.14)$$

and the Allan deviation is defined as:

$$\sigma_A(N_c) = \sqrt{\sigma_A^2(N_c)} \quad (2.15)$$

The computation of the Allan Variance is repeated for different cluster sizes, that are related to the averaging time as $\tau = T_s N_c$, in order to obtain the plot shown in Figure 2.4. The minimum point on the Allan Deviation curve is used by inertial sensor manufacturers as the standard definition of bias instability. This is the best stability you could achieve with a fully modeled sensor and active bias estimation. Therefore, for the gyroscope under test the bias stability is equal to $0.05^\circ/\text{s}$ for the x-axis, $0.04^\circ/\text{s}$ for the y-axis and $0.03^\circ/\text{s}$ for the z-axis. The same analysis provides an indication on the averaging time necessary to obtain the more stable initial estimate for the gyroscope bias, which in this case is about 20 s.

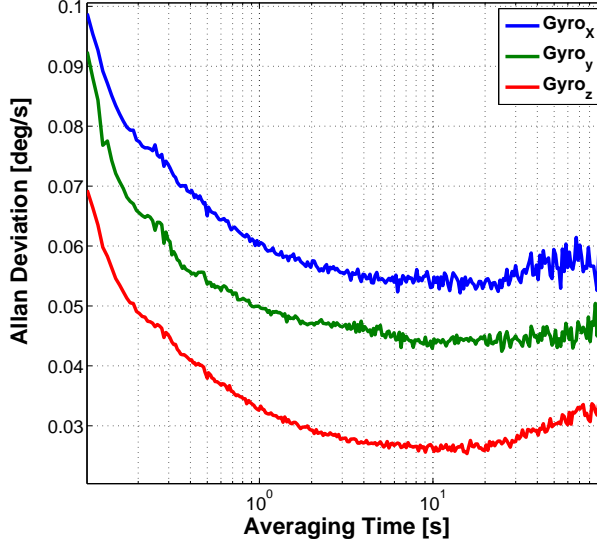


Figure 2.4: The figure reports the Allan standard deviation plots computed on the gyroscope data from the Opal IMU by APDM over a 1 hr static trial.

2.2 Calibration

The process of IMU calibration pertains to the estimation of the deterministic sources of error, introduced in the previous section, that characterize each sensing element. The basic idea is to compare the sensor output with known values generated using calibration instruments. Off the shelf IMUs are typically factory calibrated. Nonetheless, reliability of calibration parameters degrades with use or if the IMU is subjected to shocks or high intensity magnetic fields [Picerno et al., 2011]. The availability of low cost MEMS IMU and the contrast with expensive traditional calibration methodologies requiring access to sophisticated test and calibration equipment (e.g. rate table, Helmutz coil), have pushed the research towards more convenient procedures. Since calibration is a routine operation for MEMS IMUs, in this section procedures that are commonly found in the literature are reviewed.

In-field IMU calibration

The possibility to calibrate an IMU in-field is particularly appealing for a flexible usage of IMU devices. Most of these procedures are based on sensing known physical quantities that are readily available in any experimental condition. For the accelerometer and magnetometer calibration, respectively Earth's gravity and Earth's magnetic field are used as the physical standard. Calibration of gyroscopes is usually a more involved process that relies on the measurements from the other two sensors in the IMU ensemble. In order to obtain reference measurements for the calibration process, the following assumptions are made:

accelerometers: *the magnitude of the static acceleration measured must equal that of the local gravity vector* [Lötters J.C. et al., 1998];

gyroscopes: *the gravity vector measured using a static tri-axial accelerometer must equal the gravity vector computed using the IMU orientation via the integration of the angular velocities measured by gyroscopes* [Fong et al., 2008];

magnetometers: *in case of a homogeneous, uniform magnetic field, the magnitude of the vector measured using tri-axial magnetometers must equal that of the natural geomagnetic field* [Campolo et al., 2006]

Calibration of accelerometers and magnetometers boils down to an ellipsoid fitting problem, where the ellipsoid manifold is considered the geometric locus of the sensor readings. A unified, general model relating sensor voltage (\mathbf{v}_s) to the output physical quantity (\mathbf{y}) is formulated:

$$\mathbf{y} = \mathbf{K}\mathbf{v}_s + \mathbf{o} \quad (2.16)$$

where \mathbf{K} is the combination of all the multiplicative factors described in the previous section and \mathbf{o} represent the bias terms. Under the hypothesis of a uniform sensed field (gravitational or geomagnetical), the norm of the measurements (\mathbf{y}) is expected to be a constant, typically normalized to unity. This is the founding idea of the so called *scalar calibration* or *scalar checking* methods. A cost function can then be formulated, for instance as:

$$(\mathbf{y}_k - \mathbf{o})^T \mathbf{A}(\mathbf{y}_k - \mathbf{o}) = 1 \quad , \quad k = 1, \dots, N \quad (2.17)$$

where \mathbf{y}_k is the k -th vector of sensor measurements and \mathbf{A} is a sensitivity matrix related to the gains \mathbf{K} . The form of equation (2.17) is, in fact, that

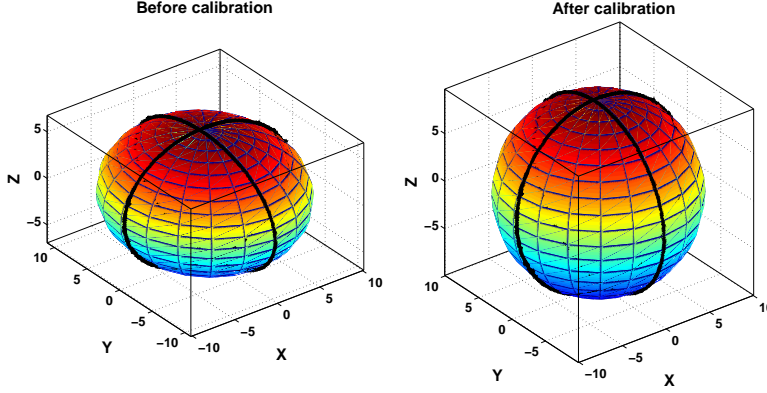


Figure 2.5: The figure reports the typical outcome of a sensor calibration procedure (specifically the least-squares method described in [Campolo et al., 2006]): uncalibrated accelerometer measurement (left) are mapped on an ellipsoid manifold. Through the estimation of the parameters describing this ellipsoid, measurements can be corrected and calibrated. After the calibration process, measurements are mapped on a sphere (right).

of an ellipsoid and the whole calibration procedure will estimate a map from this ellipsoid to a sphere, as shown in Figure 2.5. As discussed in [Bonnet et al., 2009], the fitting problem can be robustly solved either via linear [Campolo et al., 2006, Pylvanainen, 2008] or non-linear optimization [Pa et al., 2012, Elkaim, 2008]. Maximum Likelihood (ML) formulation are also found in the literature [Vasconcelos et al., 2011, Kok et al., 2012]. In [Kok et al., 2012], the IMU frame alignment is taken into account directly during the sensor calibration stage. For the case of gyroscopes calibration, the constant bias error can be estimated by taking a long term average of the gyroscopes output whilst it is not undergoing any rotation, where the duration of the recording can be inferred from the Allan Variance plot. Once the bias is known it is trivial to compensate for it by simply subtracting the bias from the output [Ferraris et al., 1995]. Bias free measurement can then be calibrated for misalignment and scale factor using the methods in [Fong et al., 2008, Tedaldi et al., 2014], which are based on correcting gyroscope based angular rotations between pairs of static configurations.

2.3. INERTIAL MOTION TRACKING

31

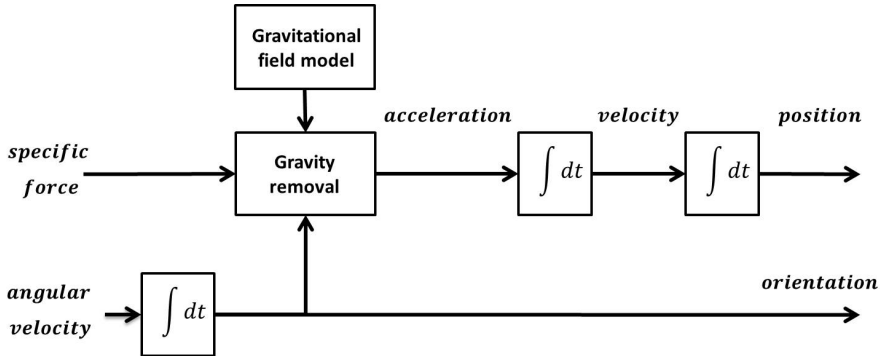


Figure 2.6: The figure illustrates the functional components of an ideal inertial navigation system: orientation is obtained from integration of measured angular velocity and it is used to remove gravity from sensed specific force. Velocity and position are then obtained respectively by single and double integration of the acceleration.

2.3 Inertial motion tracking

The measurements from an IMU can be used to track the position and orientation of the device relative to a known starting point. The underlying principles of inertial motion tracking pertains to the historical field of inertial navigation [Savage, 1998]. With the advent of MEMS devices the term ‘strapdown’ is often found alongside inertial navigation, indicating the fact that the sensor is directly attached to the body to track rather than being mechanically isolated (e.g. on a gimbaled platform). In case of inertial sensors, a navigation system must perform the following sequence of operations [Titterton and Weston, 2005], summarized in the diagram of Figure2.6:

1. determination of the angular motion of a vehicle using gyroscopic sensors, from which its orientation relative to a reference frame may be derived;
2. measure the specific force using accelerometers;
3. resolve the specific force measurements into the reference frame using the knowledge of orientation derived from the information provided by the gyroscopes;

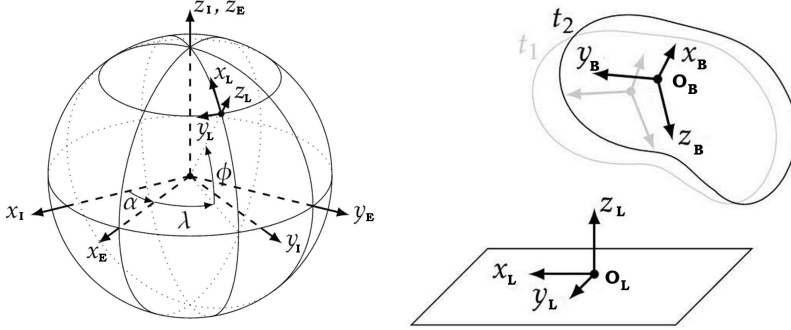


Figure 2.7: The figure illustrates the set of coordinate frames involved in the inertial navigation framework. On the left, the inertial (**I**) and the Earth's (**E**) frames are defined with respect to the Earth along with the position (latitude λ , longitude ϕ) of an hypothetical local frame (**L**). On the right, the body (**B**) at time t_1 and t_2 with respect to a local navigation frame is shown.

4. evaluate the force resulting from the gravitational field and subtract from the specific force;
5. integrate the resolved specific force measurements to obtain estimates of the velocity and position of the vehicle.

Depending on the choice of the coordinate frames with respect to which the system is navigating, each individual block will be implemented as a different set of equations, known as inertial navigation mechanization.

Coordinate frames

The coordinate frames used for mathematical formulation of inertial navigation mechanization, shown in Figure 2.7, are the following:

Body frame (B): is the coordinate frame of the moving IMU. Its origin is located in the center of the accelerometer triad and it is aligned to the casing. All the inertial measurements are resolved in this frame;

Local-Level Frame (L): this frame is defined by a plane locally tangent to the surface of the earth at the position of the IMU. This implies a

2.3. INERTIAL MOTION TRACKING

33

constant direction for gravity (straight down). The coordinate system used is Easting, Northing, Up (ENU), where Up is the normal vector of the plane, North points toward the spin axis of Earth on the plane and East completes the orthogonal system;

Inertial frame (I): this is the canonical frame for an object near the surface of the Earth. It is a non-rotating, non-accelerating frame of reference with a Cartesian coordinate system whose x axis is aligned with the mean vernal equinox and whose z axis is coaxial with the spin axis of the earth. The y-axis completes an orthogonal basis and the system's origin is located at the center of mass of the Earth;

Earth frame (E): the origin of this frame is at the Earth's center of mass. Its z-axis coincides with the inertial frame, but it rotates with respect to the i-frame at the Earth's rotation rate, which is approximately 15 degrees per hour.

The mechanization of the inertial navigation can be formulated with respect to either the Local, the Inertial or the Earth coordinate frame. The frame used as reference in the mechanization formulation is generically called the navigation frame (N). In the following, the Local frame will be chosen as the Navigation frame.

Mechanization equations

In this paragraph the dependence between sensor readings and the quantities useful for the navigation purpose, with respect to the Local-level frame (L), are briefly stated, following the original tractation reported in [Titterton and Weston, 2005]. The inertial motion tracking scheme in Figure 2.6, relating inertial quantities in the body frame (B) to position and orientation in the navigation frame (N), can be formulated with the following set of equations:

$$\begin{cases} {}^N\mathbf{p}_{k+1} = {}^N\mathbf{p}_k + \Delta T {}^N\mathbf{v}_{k+1} \\ {}^N\mathbf{v}_{k+1} = {}^N\mathbf{v}_k + \Delta T ({}^{NB}\mathbf{q}_k^* \otimes {}^B\tilde{\mathbf{f}}_{k+1} \otimes {}^{NB}\mathbf{q}_k + {}^N\mathbf{g}) \\ {}^{NB}\mathbf{q}_{k+1} = {}^{NB}\mathbf{q}_k \otimes \left(\cos \frac{\Delta T \| {}^B\boldsymbol{\omega} \|}{2}, \frac{{}^B\boldsymbol{\omega}}{\| {}^B\boldsymbol{\omega} \|} \sin \frac{\Delta T \| {}^B\boldsymbol{\omega} \|}{2} \right)^T \end{cases}$$

where the measurements from an IMU are the specific force ${}^B\mathbf{f}$, expanded to a 4-vector ${}^B\tilde{\mathbf{f}} = [0 \ {}^B\mathbf{f}]$ to perform the quaternion vector rotation, and angular velocity ${}^B\boldsymbol{\omega}$ in the device body frame (B), ΔT is the discrete time interval

from k to $k + 1$ measurement, and the quaternion representation was used to express orientations (see appendix A for details). Since IMU measurements in the body frame express motion with respect to the inertial frame, the angular velocity sensed by gyroscopes (equation (2.6)) turns out to be:

$${}^B\boldsymbol{\omega}_{I,B} = {}^{BN}\mathbf{R}({}^N\boldsymbol{\omega}_{I,E} + {}^N\boldsymbol{\omega}_{E,N}) + {}^B\boldsymbol{\omega}_{N,B} \quad (2.18)$$

where ${}^B\boldsymbol{\omega}_{N,B}$ is the actual angular velocity required for navigation and ${}^B\boldsymbol{\omega}_{I,E}$ and ${}^B\boldsymbol{\omega}_{E,N}$ are respectively the Earth rotational (about $0.005^\circ/s$) rate and the transport rate (rotation of the navigation frame with respect to the Earth frame). These latter terms are often considered negligible for the case of MEMS IMU. Also, the specific force measured by accelerometers (equation (2.2)) is given by:

$${}^B\mathbf{f} = {}^{BN}\mathbf{R}({}^N\mathbf{a}_{I,I} - {}^N\mathbf{g}) \quad (2.19)$$

where the inertial acceleration component (${}^N\mathbf{a}_{I,I}$) can be further expanded as:

$${}^N\mathbf{a}_{I,I} = {}^N\boldsymbol{\omega}_{I,E} \times {}^N\boldsymbol{\omega}_{I,E} \times {}^N\mathbf{p} + 2{}^N\boldsymbol{\omega}_{I,E} \times {}^N\mathbf{v}_N + {}^N\mathbf{a}_{N,N}$$

where ${}^N\mathbf{p}$, ${}^N\mathbf{v}_N$ and ${}^N\mathbf{a}_{N,N}$ are respectively the position, the velocity and the acceleration in the navigation frame and the formulation accounts for centripetal (first term after equal sign) and Coriolis (second term after equal sign) accelerations. Particularly, ${}^N\mathbf{a}_{N,N}$ is the quantity of interest for position tracking with an IMU.

Limiting drift in inertial tracking

The main limitations of the described inertial navigation system is that position and orientation are found by time integrating gyroscope and accelerometer signals, together with any sensor bias and noise superimposed onto them (dead reckoning approach). For the orientation estimation, direct gyroscope integration introduces a drift that grows approximately linearly with time. Instead, for the position estimation the drift issue is even more severe. On the one hand, errors on the accelerometer (detailed in 2.1) are double integrated such that any bias error results in a position drift error that grows quadratically in time. On the other hand, since position measurement is intimately related to correctness in the orientation estimation for the gravity component removal, an error of $\delta\theta$ in the tilt angle will result in an error of $\hat{\mathbf{g}} \cdot \sin(\delta\theta)$ in the horizontal components of the acceleration, which is again double integrated in order to compute position. Therefore, from a practical point of view, position accuracy

2.3. INERTIAL MOTION TRACKING

35

of inertial navigation systems is limited by gyroscopes rather than accelerometers. Generally, two are the major approaches to cope with drifts in inertial motion tracking systems: sensor fusion and modeling assumptions.

Sensor fusion

Sensor fusion is defined as the process of combining sensory data from multiple types of sensors in order to achieve a better estimate of the state of a system than would be possible when these sources are used individually. For standalone IMU devices, this concept has been heavily exploited, especially to limit drifts in the orientation estimate. The basic idea of orientation estimation with an IMU is that an orientation can be computed in two different ways: either by gyroscope signal integration or by vector observation of the gravity and Earth's magnetic field. In fact, from accelerometer (\vec{a}) and magnetometer (\vec{m}) readings a rotation matrix ${}^{NB}\mathbf{R} \in SO(3)$ from the body to a navigation frame (defined by local gravity and magnetic field) can be derived as:

$${}^{NB}\mathbf{R} = \left[\frac{\vec{a}}{\|\vec{a}\|_2} \times \frac{\vec{m}}{\|\vec{m}\|_2} \times \frac{\vec{a}}{\|\vec{a}\|_2}, \frac{\vec{a}}{\|\vec{a}\|_2} \times \frac{\vec{m}}{\|\vec{m}\|_2}, \frac{\vec{a}}{\|\vec{a}\|_2} \right] \quad (2.20)$$

The problem of combining multiple vector observation in order to estimate orientation is known in the literature as the Wahba's problem [Wahba, 1965]. There exists an entire class of methods, termed *deterministic*, dedicated to solve this problem [Shuster and Oh, 1981, Bar-Itzhack, 1996]. Both gyroscope based and deterministic approaches to measure orientation can be combined in a sensor fusion fashion. A possibility is to exploit the complementary noise characteristic, in the frequency domain, of gyroscopes and accelerometers and magnetometers. The idea is to rely on gyroscope integration in dynamic conditions (low band noise) and on vector observation in static condition (high band noise). This class of algorithms is termed *complementary* filters and examples can be found in [Mahony et al., 2008, Madgwick et al., 2011]. A second option is to combine the measurements with stochastic modeling, e.g. to use a kinematics model propagated with three axis angular velocity integrating gyroscopes. In order to limit orientation estimate drift, the state vector is usually prepended with more states that accounts for bias components. This approach is commonly formulated as a Kalman filter algorithm and examples of implementations can be found in [Roetenberg et al., 2005, Sabatini, 2011]. Finally, a thorough review of the existing literature on the topic of sensor fusion for orientation estimation with an IMU can be found in [Crassidis et al., 2007].

Modeling assumptions

In many applications where IMUs are used for tracking the motion, drifts can be reduced by exploiting extra information that comes from the knowledge of the underlying physical system model. For instance, assumptions on the type of dynamics characterizing the system can be made and used to reduce drift. A type of information commonly used for this purpose is knowledge about the time epochs when the system is in a stationary phase, i.e. when the system has a constant position and orientation. Using this information to bound the error growth is referred to as using zero-velocity updates (ZUPT). One of the best examples of implementation of this concept is NavShoe [Foxlin, 2005], where a shoe mounted IMU is used for pedestrian tracking. When a person walks, their feet alternate between a stationary stance phase and a moving stride phase. The system uses the stance phase for zero velocity updates (ZUPT), allowing to reduce the drift from cubic to linear in time. Other examples are in the field of human motion capture. Here, biomechanical modeling and assumptions are often used either to estimate human body configuration and to limit drift [Zhou and Hu, 2005, El-Gohary and McNames, 2012]. Typical assumptions regard measured accelerations and are [Luinge, 2002]:

- The bandwidth of accelerometer is limited by the inertia of the body segment to which the sensor is attached.
- The mean acceleration of a body segment, with respect to a nonrotating coordinate system, is zero, also implying the acceleration spectrum is zero for low frequencies.

The same author in [Luinge et al., 2007], proposed a technique for limiting drifts around the vertical based on the natural constraint of the elbow abduction angle. Also, periodic nature of human walking is often assumed to reduce integration drifts, e.g. in [Sabatini, 2005].

2.4 Available instrumentation

The work and the results presented in the thesis, are obtained using commercially available IMUs. In particular, the Opal sensor by APDM and the series MTi-30 produced by Xsens. The Opal is a wearable, wireless device and has been used for the validation of orientation tracking performance in chapter 4 and in the experimentation with children in chapter 6. The MTi-30 is

2.4. AVAILABLE INSTRUMENTATION

37

Table 2.1: A comparison of the Xsens MTi-30 and the APDM Opal main features

	Mti-30 (Xsens)			Opal (APDM)		
Sensor	Acc	Gyro	Mag	Acc	Gyro	Mag
Range	50 m/s ²	450 °/s	± 750 mGauss	± 2g or ± 6g	± 2000 °/s	± 6000 mGauss
Bandwidth [Hz]	375	415	-	50	50	50
Size	57 x 42 x 24 mm			48.4 x 36.1 x 13.4 mm		
Weigth	55g (cased)			< 22g		
Output rate [Hz]	Up to 2 kHz			20 to 128		
Orientation accuracy	Static: 0.2° (roll-pitch), 1.0° (yaw) Dynamic: 0.5°(roll-pitch)			Static: 1.15° (roll-pitch), 1.50° (yaw) Dynamic: 2.80°		

more rugged and cabled sensor and was used for navigation of an omnidirectional robotic platform, described in chapter 5. Measured data from the IMUs are calibrated for in-factory determined biases, gains, nonorthogonalities, and temperature drifts. Salient features of the two devices are summarized in table 2.1.

Tesi di dottorato in Ingegneria biomedica, di Luca Ricci,
discussa presso l'Università Campus Bio-Medico di Roma in data 11/06/2015.
La disseminazione e la riproduzione di questo documento sono consentite per scopi di didattica e ricerca,
a condizione che ne venga citata la fonte.

Chapter 3

Statistical estimation

In this chapter a brief introduction to the field of estimation is proposed. The purpose is to provide the reader with the basic notions, particularly with reference to the stochastic methods such as the maximum likelihood and maximum a posteriori estimators, and to introduce the general estimation framework in which part of this work of thesis has been developed. The material in this chapter is by no means exhaustive of the topic and references are given for further readings.

3.1 Introduction

In real-world problems the presence of uncertainty is pervasive. The typical scenario is that of a measurement quantity ($\hat{\mathbf{y}}$) affected by additive noise (\mathbf{e}_y):

$$\hat{\mathbf{y}} = \mathbf{y} + \mathbf{e}_y \quad (3.1)$$

where \mathbf{y} is the hypothetical exact value. In consideration of that, the theory of probability provides a consistent framework for the quantification and manipulation of uncertainty. In this framework, samples of an unknown quantity are modelled as random variables, e.g. the measurement $\hat{\mathbf{y}}$, and its behaviour is described in terms of a probability density function (**pdf**), refer to [Papoulis, 2002] for a thorough introduction to probability theory. The problem of estimation in this probabilistic framework is that of inferring information on the distribution of data, i.e. the **pdf**, from a sample of independent, identically distributed (i.i.d.) random variables. A fundamental choice to the aim of estimation is whether to make hypotheses about the underlying behaviour of the

data, i.e. assuming to be described by a model, or not. The first approach leads to the class of *parametric* estimators, which will be discussed in this chapter, while the second to the class of *non-parametric* methods.

In the typical setting of (3.1) the noise term is modelled with a **pdf** $p(\mathbf{e}_y)$. The **pdf** $p(\mathbf{e}_y)$ of the noise also determines the conditional **pdf** $p(\hat{\mathbf{y}}|\theta)$ of the measurements, given the hypothetical exact model:

$$\mathbf{y} = f(\mathbf{u}, \theta) \quad (3.2)$$

that describes the system and is parametrized with a set of θ parameters defined in a space Θ and the inputs (\mathbf{u}) that excite the system. The goal of the estimation is to infer the value of the parameters $\theta \in \Theta$ from a set of i.i.d. sensor measurements $\{\hat{\mathbf{y}}_1, \dots, \hat{\mathbf{y}}_N\}$. Mathematically, this translates into finding a mapping ϕ , the estimator, which maps the data to the parameters' values, the estimate, i.e.:

$$\hat{\theta} = \phi(\hat{\mathbf{y}}) \quad (3.3)$$

where $\hat{\theta}$ is the parameter estimate. Among the different estimators that can be found in the statistic literature [Lehmann, 1998, Hastie and Friedman, 2009], the maximum likelihood (ML) estimator and the maximum a posteriori (MAP) estimator are of particular interest and will be used in chapter 5.

Maximum Likelihood Estimator

Given a choice for the parameter values $\hat{\theta} \in \Theta$ of a data distribution, the corresponding $p(\hat{\mathbf{y}}|\hat{\theta})$ will show that some data are more probable than other. Conversely, given a set of i.i.d. data $\{\hat{\mathbf{y}}_1, \dots, \hat{\mathbf{y}}_N\}$, the likelihood that they are drawn from a distribution with $p(\hat{\mathbf{y}}|\hat{\theta})$ can be quantified as:

$$\mathcal{L}(\hat{\theta}|\hat{\mathbf{y}}) = p(\hat{\mathbf{y}}|\hat{\theta}). \quad (3.4)$$

where $\mathcal{L}(\hat{\theta}|x)$ is called the *likelihood* function.

Definition 3.1. The ML estimate is the value $\hat{\theta} = \hat{\theta}(\hat{\mathbf{y}}) \in \Theta$ maximizing $\mathcal{L}(\hat{\theta}|\hat{\mathbf{y}})$, provided it exists, i.e.:

$$\hat{\theta}_{ML} = \arg \max_{\theta} p(\hat{\mathbf{y}}|\theta) \quad (3.5)$$

The method of ML selects the set of values of the model parameters that maximizes the likelihood function. Intuitively, this maximizes the agreement of the selected model with the observed data. ML estimation gives a unified approach to estimation, which is well-defined in the case of the normal distribution and many other problems and is an asymptotically efficient estimator.

Maximum A Posteriori Estimator

In some cases there could be a priori information available on the distribution parameters to estimate, e.g. there could be a model describing the physical process that generated the dataset. This prior information can be expressed in terms of a **pdf** describing the parameters to be estimated. Mathematically, the parameter θ to be estimated is considered as the value of an random variable. The associated **pdf** $p(\theta)$ is called the prior probability. The Bayes' theorem provides a way to incorporate prior information in the estimation process:

$$p(\theta|\hat{\mathbf{y}}) = \frac{p(\hat{\mathbf{y}}|\theta)p(\theta)}{p(\hat{\mathbf{y}})} = \eta p(\hat{\mathbf{y}}|\theta)p(\theta) \quad (3.6)$$

The term on the left hand side of the equation is called the posterior. On the right hand side, the numerator is the product of the likelihood term and the prior term. The denominator ($p(\hat{\mathbf{y}})$) serves as a normalization term, denoted with a constant η , so that the posterior **pdf** integrates to unity. Thus, Bayesian inference produces the MAP estimate.

Definition 3.2. The MAP estimate is the value $\hat{\theta} = \hat{\theta}(\hat{\mathbf{y}}) \in \Theta$ maximizing the posterior $p(\theta|\hat{\mathbf{y}})$, provided it exists, i.e.:

$$\hat{\theta}_{MAP} = \arg \max_{\theta} p(\theta|\hat{\mathbf{y}}) = \arg \max_{\theta} \eta p(\hat{\mathbf{y}}|\theta)p(\theta) \quad (3.7)$$

In case of an uninformative, uniform prior **pdf**, the MAP estimate and the ML estimate are equivalent.

3.2 A cost function interpretation

The parametric estimators presented in the previous paragraphs introduced mathematical optimization problems in which the **pdf** to be maximized can be equivalently thought of as a cost function, see [Pintelon and Schoukens, 2012]. In order to estimate the unknown parameter vector, ML and MAP are restated as cost function minimization problems exploiting the equivalence:

$$\arg \max_{\theta} p(\mathbf{x}|\theta) = \arg \min_{\theta} -p(\mathbf{x}|\theta) \quad (3.8)$$

A natural log function is also applied, leading to the equivalent problem (e.g. for the ML case):

$$\hat{\theta}_{ML} = \arg \max_{\theta} p(x|\theta) = \arg \min_{\theta} -\log(p(x|\theta)) \quad (3.9)$$

In fact, the monotonicity of the log function does not affect the solution of the problem (minima and maxima are preserved) plus it has the advantage to transform product of factors into a summation of factors. The latter property is appealing in view of the solution of the problem with general-purpose optimization techniques that are found in the literature [Boyd and Vandenberghe, 2010], e.g. Newton or trust-region methods, as it make easier to compute derivatives of the cost function. In the following, the derivation of the equivalent cost function for two parametric **pdf**, i.e. a Gaussian and a Student-T, are discussed. The hypothetical scenario in which the math is developed is described by eq(3.1).

Gaussian cost function

The most common choice for describing the noise affecting a real system, e.g. noise on sensor's measurements, is that to use a Gaussian model. It can be shown that Gaussian distributed disturbing noise leads to a quadratic cost criterion. Consider the random noise vector \mathbf{e}_y of eq. 3.1 modelled with a Gaussian multivariate distribution with a zero mean $\boldsymbol{\mu}$ and a covariance matrix Σ . The measurement $\hat{\mathbf{y}}$ from the sensor is then described by a Gaussian distribution as well, i.e.:

$$p(\hat{\mathbf{y}} - \mathbf{y}) = (2\pi)^{-\frac{m}{2}} \det \Sigma^{-\frac{1}{2}} \exp\left(-\frac{1}{2}(\hat{\mathbf{y}} - \mathbf{y})^T \Sigma^{-1}(\hat{\mathbf{y}} - \mathbf{y})\right) \quad (3.10)$$

and by applying the log transformation:

$$\log(p(\hat{\mathbf{y}} - \mathbf{y})) = -\frac{m}{2} \log(2\pi) - \frac{1}{2} \log \det \Sigma - \frac{1}{2}(\hat{\mathbf{y}} - \mathbf{y})^T \Sigma^{-1}(\hat{\mathbf{y}} - \mathbf{y}) \quad (3.11)$$

If we consider the ML problem of estimating the parameters $\theta \in \Theta$ of the model in (3.2), the following optimization problem is obtained:

$$\begin{aligned} \arg \min_{\theta} \frac{m}{2} \log(2\pi) + \frac{1}{2} \log \det \Sigma + \frac{1}{2}(\hat{\mathbf{y}} - \mathbf{y}(\theta))^T \Sigma^{-1}(\hat{\mathbf{y}} - \mathbf{y}(\theta)) = \\ \arg \min_{\theta} \frac{1}{2}(\hat{\mathbf{y}} - \mathbf{y}(\theta))^T \Sigma^{-1}(\hat{\mathbf{y}} - \mathbf{y}(\theta)) = \\ \arg \min_{\theta} \frac{1}{2} \mathbf{e}_y(\theta)^T \Sigma^{-1} \mathbf{e}_y(\theta) = \arg \min_{\theta} \frac{1}{2} \|\mathbf{e}_y(\theta)\|_{\Sigma^{-1}}^2 \end{aligned} \quad (3.12)$$

where the symbol $\|\cdot\|_{\Sigma}$ was used to denote the quadratic norm operator defined as:

$$\|\mathbf{x}\|_{\Sigma} = (\mathbf{x}^T \Sigma^{-1} \mathbf{x})^{\frac{1}{2}} \quad (3.13)$$

3.2. A COST FUNCTION INTERPRETATION

43

In the minimization problem of eq. (3.12) a number of terms gave no contribution to the aim of the minimization and could be ignored. The resulting cost function is a quadratic in the error term \mathbf{e}_y and it is weighted by the covariance matrix Σ assigned to the noise. The shape of this cost function is represented in figure 5.15 of chapter 5.

Student-T cost function

In some cases experimental data are better fitted by a more heavy tailed distribution than a Gaussian. That can happen for instance because of measurement outliers from unreliable sensors, target manoeuvres in tracking applications, or errors that occur when working with linearised nonlinear systems. If it is known that some outliers in the measurements can appear (e.g. due to exceptionally large errors, a temporary sensor failure or a transmission error), then noise on measurements can be better modelled by a Student-T distribution, i.e.:

$$p(\hat{\mathbf{y}} - \mathbf{y}) = \frac{\Gamma[(\nu + p)/2]}{\Gamma(\nu/2)\nu^{n/2}\pi^{n/2}|\Sigma|^{1/2}} \left[1 + \frac{1}{\nu}(\hat{\mathbf{y}} - \mathbf{y})^T \Sigma^{-1}(\hat{\mathbf{y}} - \mathbf{y}) \right]^{-(\nu+n)/2} \quad (3.14)$$

where ν denotes the degrees of freedom of the distribution, Γ is the gamma function and n is the dimension of the vector $(\hat{\mathbf{y}} - \mathbf{y}) \in \mathbb{R}^n$. In a ML estimation framework where the parameters $\theta \in \Theta$ of the model in (3.2) are of interest, the following optimization problem is obtained:

$$\begin{aligned} \arg \min_{\theta} -\log\left(\frac{\Gamma[(\nu + 1)/2]}{\Gamma(\nu/2)\nu^{n/2}\pi^{n/2}|\Sigma|^{1/2}}\right) + \frac{\nu + n}{2} \log\left(1 + \frac{(\hat{\mathbf{y}} - \mathbf{y}(\theta))^T \Sigma^{-1}(\hat{\mathbf{y}} - \mathbf{y}(\theta))}{\nu}\right) = \\ \arg \min_{\theta} \frac{\nu + n}{2} \log\left(1 + \frac{(\hat{\mathbf{y}} - \mathbf{y}(\theta))^T \Sigma^{-1}(\hat{\mathbf{y}} - \mathbf{y}(\theta))}{\nu}\right) = \\ \arg \min_{\theta} \frac{\nu + n}{2} \log\left(1 + \frac{\|\mathbf{e}_y(\theta)\|_{\Sigma^{-1}}^2}{\nu}\right) \end{aligned} \quad (3.15)$$

where the function to be minimized has a logarithmic shape with a quadratic argument and is plotted in 5.15 of chapter 5. As the gradient of this cost function decreases the more the argument is far from the minimum, its contribution to the final solution of the minimization is accordingly reduced [Boyd and Vandenberghe, 2010]. This property can be exploited to implement an outlier detection and rejection strategy in a scenario in which multiple sources of information on an unknown quantity are available, e.g. a sensor measurement and a physical model. In fact, assigning a student-T cost to the outlier

prone source of information and a quadratic cost to the other has the effect that, in case of a strong disagreement, the outlier prone sources will be ignored in the computation of a solution.

3.3 A general probabilistic framework for estimation

In this section the results discussed in the previous paragraphs are combined into a general framework for the estimation that will be extensively used for the application described in chapter 5. The general problem addressed by this framework is that of estimating the state vector (\mathbf{x}) of a system described using a state space representation. The system is generally assumed nonlinear and affected by additive noise, i.e. formulated in discrete time as:

$$\begin{cases} \mathbf{x}_{1,k+1} = f(\mathbf{x}_k, \mathbf{u}_k) + \mathbf{v}_{1,k} \\ \vdots \\ \mathbf{x}_{n,k+1} = f(\mathbf{x}_k, \mathbf{u}_k) + \mathbf{v}_{n,k} \\ \mathbf{y}_{1,k} = g(\mathbf{x}_k, \mathbf{u}_k) + \mathbf{w}_{1,k} \\ \vdots \\ \mathbf{y}_{r,k} = g(\mathbf{x}_k, \mathbf{u}_k) + \mathbf{w}_{r,k} \end{cases} \quad (3.16)$$

where $\mathbf{x}_k \in \mathbb{R}^n$ represents the state of the system at time sample k , $\mathbf{u}_k \in \mathbb{R}^m$ is a vector of m inputs, and $\mathbf{y}_k \in \mathbb{R}^r$ is the vector of the r system responses. This framework can be specialized to target both filtering or smoothing problems.

In filtering applications the general problem specializes into finding an estimate of the current state given all the available measurements. From a mathematical standpoint, the target of the estimation is the posterior **pdf** $p(\mathbf{x}_k | \mathbf{y}_{1:k})$, where $\mathbf{y}_{1:k}$ is the set of all measurements $\{\mathbf{y}_1, \dots, \mathbf{y}_N\}$. In this framework the Markov assumption is assumed valid for the model, specifically:

$$p(\mathbf{x}_i | \mathbf{x}_{1:i-1}) = p(\mathbf{x}_i | \mathbf{x}_{i-1}) \quad , \quad p(\mathbf{y}_i | \mathbf{x}_i) = p(\mathbf{y}_i | \mathbf{x}_{1:i}) \quad (3.17)$$

For the nonlinear system formulation of (3.16) the following correspondence applies:

$$\mathbf{x}_{k+1} = f(\mathbf{x}_k, \mathbf{u}_k) + \mathbf{v}_k \Rightarrow p(\mathbf{x}_k | \mathbf{x}_{k-1}) \quad (3.18)$$

$$\mathbf{y}_k = g(\mathbf{x}_k, \mathbf{u}_k) + \mathbf{w}_k \Rightarrow p(\mathbf{y}_k | \mathbf{x}_k) \quad (3.19)$$

3.3. A GENERAL PROBABILISTIC FRAMEWORK FOR ESTIMATION 5

and the target filter **pdf** can be computed using the following recursion:

$$p(\mathbf{x}_k | \mathbf{y}_{k-1}) = \int p(\mathbf{x}_k | \mathbf{x}_{k-1}) p(\mathbf{x}_{k-1} | \mathbf{y}_{k-1}) d\mathbf{x}_{k-1} \quad (3.20)$$

$$p(\mathbf{y}_k | \mathbf{y}_{k-1}) = \int p(\mathbf{y}_k | \mathbf{x}_k) p(\mathbf{x}_k | \mathbf{y}_{k-1}) d\mathbf{x}_k \quad (3.21)$$

$$p(\mathbf{x}_k | \mathbf{y}_k) = \frac{p(\mathbf{y}_k | \mathbf{x}_k) p(\mathbf{x}_k | \mathbf{y}_{k-1})}{p(\mathbf{y}_k | \mathbf{y}_{k-1})} \quad (3.22)$$

which entails marginalization steps and the Bayes' rule for conditional **pdf**. More details on the filter theory and the aspects related to practical methodologies to compute the **pdf** of (3.22) can be found in [Gustafsson, 2013].

In smoothing problems, the general problem turns into finding the best estimate of the entire state trajectory given all the measurements. From a mathematical standpoint, the target of the estimation is the **pdf** $p(\mathbf{x}_{1:k} | \mathbf{y}_{1:k})$, where $\mathbf{x}_{1:k}$ is the set of all states $\{\mathbf{x}_1, \dots, \mathbf{x}_N\}$ and $\mathbf{y}_{1:k}$ is the set of all measurements $\{\mathbf{y}_1, \dots, \mathbf{y}_N\}$. In order to obtain a point estimate from the posterior, the MAP estimator is the natural choice. With reference to the state space formulation in (3.16), the MAP problem is expressed as:

$$\begin{aligned} \hat{\mathbf{x}} &= \arg \max_{\mathbf{x}_{1:k}} p(\mathbf{x}_{1:k} | \mathbf{y}_{1:k}) = \arg \max_{\mathbf{x}_{1:k}} p(\mathbf{x}_1) \prod_{i=2}^k p(\mathbf{x}_i | \mathbf{x}_{i-1}) \prod_{i=1}^k p(\mathbf{y}_i | \mathbf{x}_i) = \\ & \arg \min_{\mathbf{x}_{1:k}} -\log(p(\mathbf{x}_1)) - \sum_{i=2}^k \log(p(\mathbf{x}_i | \mathbf{x}_{i-1})) - \sum_{i=1}^k \log(p(\mathbf{y}_i | \mathbf{x}_i)) \end{aligned} \quad (3.23)$$

where $\hat{\mathbf{x}}$ indicates the estimated quantity and the Markov assumption of (3.17) is again assumed. This can then be turned into the following optimization problem, which accounts for the modelling equation describing the system in (3.16) as:

$$\arg \min_{\theta} -\log(p(\mathbf{x}_1)) - \sum_{i=1}^{k-1} \log(p(\mathbf{v}_i)) - \sum_{i=1}^k \log(p(\mathbf{w}_i)) \quad (3.24)$$

$$\begin{aligned} \text{s.t. } \quad & \mathbf{x}_i = f(\mathbf{x}_i, \mathbf{u}_i) + \mathbf{v}_{1,k} \quad , \quad i = 1, \dots, k-1 \\ & \mathbf{y}_i = g(\mathbf{x}_i, \mathbf{u}_i) + \mathbf{w}_i \quad , \quad i = 1, \dots, k \end{aligned} \quad (3.25)$$

where the **pdf** to be minimized are subject to (s.t.) the constraints extracted from the system model (3.16) and with parameters $\theta = \{\mathbf{x}_{1:k}, \mathbf{v}_{1:k}, \mathbf{w}_{1:k}\}$. The

use of a MAP formulation for the smoothing problem allows to straightforwardly extended the estimation to include other parameters of interest as well, e.g. alignment matrix between frames.

Part II

Research focus

Tesi di dottorato in Ingegneria biomedica, di Luca Ricci,
discussa presso l'Università Campus Bio-Medico di Roma in data 11/06/2015.
La disseminazione e la riproduzione di questo documento sono consentite per scopi di didattica e ricerca,
a condizione che ne venga citata la fonte.

Chapter 4

Validating accuracy of inertial orientation tracking

This chapter presents a systematic characterization of the accuracy in orientation tracking for wearable IMU devices, where the orientation is estimated via state of the art sensor fusion algorithms. The assessment was carried out having in mind the application to human motion tracking and use a robotic platform in order to generate controlled and repeatable conditions. The major contribution of this validation is in providing detailed information on static and dynamic performance, covering a large number of test cases, of IMU based orientation trackers. First, motivation and overview of relevant related literature is presented in pursuance of putting following material in perspective. Then, the experimental methodology is described and the results of the assessment are reported. The chapter is concluded with a critical discussion of findings and guidelines are provided in view of practical usage of IMU for orientation tracking, within the field of human related applications.

4.1 Problem formulation

Human kinematic tracking by means of wearable sensors that are directly attached to the body is establishing as a promising solution in the community of motion capture researchers. These systems are based on multiple sensing devices embedding 3D inertial sensors, i.e. accelerometers and gyroscopes, coupled with a 3D magnetic flux sensor and are typically referred in literature as IMU, or magnetic IMU (M-IMU). A part from inertial and magnetic

CHAPTER 4. VALIDATING ACCURACY OF INERTIAL ORIENTATION TRACKING

quantities, each unit can provide an estimate of 3D orientation with respect to a fixed system of coordinates by using sensor fusion techniques [Crassidis et al., 2007]. If the IMU is firmly attached on a segment of the human body, it is possible to obtain an estimate of its absolute orientation. Further on, multiple IMUs attached to multiple body segments provide relative joint orientation measurements that can be combined in order to reconstruct human kinematics [Roetenberg,]. Despite the IMU based solution to human motion capture is regarded as less accurate than stereo-photogrammetry based systems, that are historically ranked as the ‘golden standard’, it comes with inherent advantages: one above all, the possibility to continuously measure human kinematics, even outside of dedicated laboratories and with less operational constraints. Moreover, the field of application for these systems is vast, ranging from physical and biomechanical functional assessment and rehabilitation [Patel et al., 2012, Zhou and Hu, 2008], to sports as well as ergonomics [Vignais et al., 2013], movie production and gaming. Therefore, the last decade has witnessed extensive research effort committed to: the investigation of data fusion algorithms for orientation estimation with IMUs [Yun and Bachmann, 2006, Roetenberg et al., 2007, Sabatini, 2011, Fourati et al., 2012, Mahony et al., 2008, Campolo et al., 2009, Madgwick et al., 2011, Tian et al., 2013]; the definition of protocols for practical usage of wearable motion capture systems [Ricci et al., 2014],[Cutti et al., 2010],[de Vries et al., 2010],[Kontaxis et al., 2009],[Picerno et al., 2008],[Cutti et al., 2008]; the application of these systems to different scenarios [Luinge et al., 2007, Brodie et al., 2008a, Cooper et al., 2009]. Surprisingly, much less attention has been dedicated to rigorously assessing the accuracy in measuring orientation that can be achieved by using wearable IMUs under typical motion conditions found in human related applications. On the industrial side, technical specification of commercial systems reported by vendors are presented with caveats and are poorly documented, e.g. device dynamic accuracy is given without detailing the testing setup and protocol, amplitude and bandwidth of testing movements. On the research side, a variability in results is currently found in the literature, where best performance is usually matched with slow and short range movements tracking. The main contribution of this work is in providing a systematic characterization of the accuracy in orientation tracking using state-of-the-art sensor fusion algorithm with IMU based system for human motion capture under controlled and repeatable conditions. Selected algorithms are in the classes of stochastic and complementary filtering to which most of developed methods pertain. The assessment protocol that is presented comprises evaluation of both absolute (single IMU compared to reference) and relative (pairwise comparison among

4.1. PROBLEM FORMULATION

51

IMUs) accuracy in static and dynamic scenarios. For the static part, both unperturbed and after motion performance are investigated. For the dynamic part, accuracy was assessed for a number of different excitations signals, varied both in amplitude of motion and frequency content, that are selected in the range defined by human motion related literature. Also, three conditions were tested in order to individually identify performance for the *attitude* (i.e. rotation against the gravity vector) and the *heading* (i.e. rotation along the gravity vector) components of orientation, plus a third midway, mixed case generally termed in the following as *attitude and heading*. The material is organized as follows: in section 4.2 the experimental setup is described together with the experimental protocol and the data analysis procedure. In section 4.4 the outcome of the validation results for each trial is reported and, in the successive section 4.5, the chapter is concluded with a critical discussion of the findings. Beforehand, to put the the following material in perspective, next paragraph provides a brief review of the relevant literature on the topic.

Related work

Existing studies in the literature that investigate accuracy of IMU in orientation consider static and dynamic validation mostly under manually generated conditions. In [Cutti et al., 2006], Cutti et al. evaluated accuracy in orientation of 4 IMUs rigidly attached to a manually rotated plank. Mean angular velocities of $180^\circ/s$ and $360^\circ/s$ were generated with the help of a metronome and a worst case angular error for the two velocities was found to be 5.4° and 11.6° respectively. The oscillatory motion of a pendulum has also been considered for the dynamic accuracy assessment, e.g. in [Brodie et al., 2008c] and in [Godwin et al., 2009]. In both studies, an optical system was used as reference. In the first one, a worst case RMS error was found to be in the range $8.5^\circ \div 11.7^\circ$ for the IMU factory orientation estimator (Kalman filter) and much lower $0.8^\circ \div 1.3^\circ$ for the algorithm developed by the authors. In the latter, the mean RMS error range was in between 1.9° and 3.5° . A part from single device accuracy, Picerno et al. [Picerno et al., 2011] focused on consistency in orientation measurement of multiple IMUs by presenting a spot check for device assessment. They pointed out criticalities in measuring relative orientation with IMUs, reporting errors as large as 11.4° . At present, the only example of accuracy evaluation under controlled conditions, i.e. with an experimental setup and protocol capable of providing well-defined and repeatable testing movements is that of [Lebel et al., 2013]. In this work, Lebel and colleagues compared different commercial IMU based systems for motion tracking

CHAPTER 4. VALIDATING ACCURACY OF INERTIAL ORIENTATION TRACKING

against an optical system and used an instrumented gimbal table to generate static and dynamic motion conditions. Their focus was on the effect of angular velocity on orientation error and reported results suggest a significant effect of this variable for all tested devices. Mean errors w.r.t optical reference for the case of $90^\circ/s$ and $180^\circ/s$ angular velocities were found to be around 3° and 7° . Finally, a recent paper from Bergamini et al. [Bergamini et al., 2014] investigated accuracy of different sensor fusion approaches for orientation estimation with IMUs during several manual and locomotion tasks. Experimental setup consisted in two units attached to pelvis and forearm and an optical motion capture system as reference. Reported mean errors varied greatly both depending on the task and the type of rotation (heading or attitude) and ranging from about 5° for manual tasks up to 21° for locomotion.

4.2 Materials and Methods

Experimental setup

The experimental setup for this study, shown in Figure 4.1, consists of a robotic arm and a commercial set of IMUs. The robotic arm is the lightweight manipulator LWR 4+ manufactured by KUKA GmbH. It is equipped with 7 rotational joints paired with high resolution encoders and distributed along an anthropomorphic kinematic chain. Depending on the specific joint, an angular velocity ranging from a minimum of $\pm 110^\circ/s$ to a maximum of $\pm 240^\circ/s$ can be generated. Relative orientation of the robot joints is measured by absolute 16-bit magnetic encoder corresponding to an accuracy in joint orientation $< 0.01^\circ$. Also, a salient feature of the platform is its high repeatability, ± 0.05 mm (ISO 9238), according to manufacturer specifications. Joint odometry and pose of the end-effector (EE) can be retrieved from the robot up to a maximum rate of 1 kHz. The commercial set of IMUs is manufactured by APDM Inc. and composed by 6 units ("Opal" type). Each unit is a lightweight box (22 g). A real time computation of the orientation is also available via an embedded Kalman filter (KF) algorithm. The accuracy in orientation, advertised by the manufacturer, is 1.15° and 1.50° RMS for static conditions in roll/pitch and heading respectively, and 2.8° RMS for dynamic conditions. Synchronized measurements from the units can be retrieved up to a maximum rate of 128 Hz. In order to connect the IMUs to the robotic arm a proper tool was designed in Solidworks, shown in Figure 4.1, that allows the housing of the 6 IMUs and can be rigidly fixed to the robotic arm EE using plastic screws. The overall weight of the tool and the 6 units is about 1.5 Kg, a value below the maximum

4.2. MATERIALS AND METHODS

53

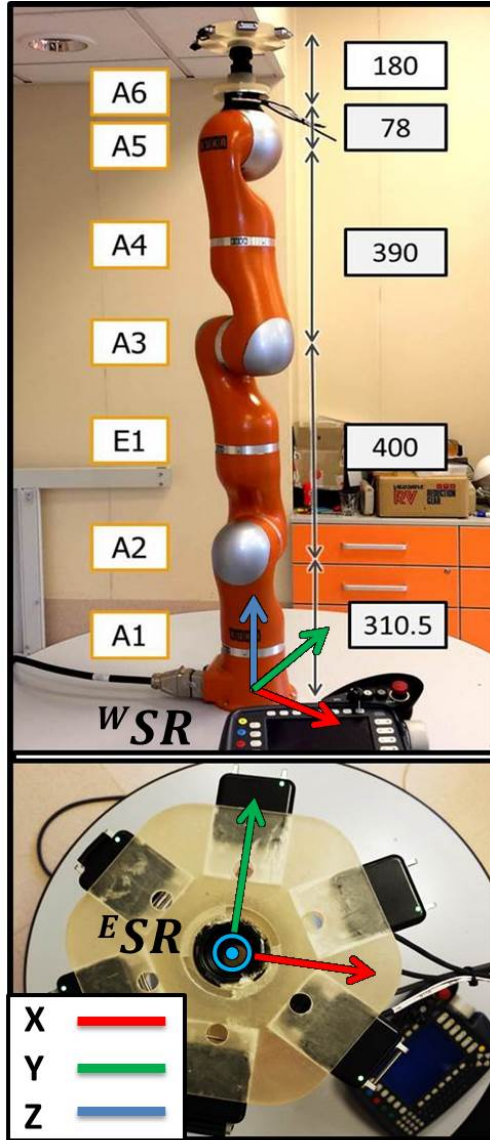


Figure 4.1: The figure shows the experimental setup for accuracy assessment. On the top, a view of the KUKA LWR 4+ robotic arm with, on the left side, the identifier of the 7 joints as specified by the manufacture and, on the right side, the length (in millimeters) of each link plus the custom devised tool attached to the EE . On the bottom, a closer view of the EE tool housing the full set of 6 IMUs.

CHAPTER 4. VALIDATING ACCURACY OF INERTIAL ORIENTATION TRACKING

payload that the robotic arm can sustain (14 Kg). The system was connected to a laptop, respectively through an Ethernet connection for the KUKA LWR 4+ and a dedicated wireless connection for the IMUs.

Sensor fusion for estimating orientation with IMU

At present, there are two main classes of algorithms of widespread use in the literature: non-linear complementary filters (CF) [Mahony et al., 2008, Campolo et al., 2009, Madgwick et al., 2011, Tian et al., 2013] and Kalman filters (KF) [Roetenberg et al., 2007, Sabatini, 2011]. The class of non-linear CF exploits the complementary spectral noise characteristics of measurement sources in order to filter out low frequency noise components from gyroscope measurements, that are due to slow time varying biases, and high frequency noise components affecting accelerometer and magnetometer in dynamic conditions. To the aim of an accuracy performance validation a recent implementation of a non-linear complementary filter that uses a Gauss-Newton algorithm (GNA) optimization, proposed in [Tian et al., 2013], was selected. The tunable parameters weights relative contribution of gyroscopes versus accelerometer and magnetometer (β), the detection thresholds for dynamic acceleration (ϵ_A) and magnetic field perturbations (ϵ_M) and were set according to recommendations by the authors ($\beta = 0.0756$ rad/s, $\epsilon_A = 0.25$ m/s² and $\epsilon_M = 2$ uT).

The class of KF algorithms represents the stochastic approach to orientation estimation. They use a state-space model description for describing the system and assumes Gaussian distribution for the noise components. This approach offers flexibility in defining the state vector to be estimated, that can easily be expanded to include sensor biases, and can also incorporate detection strategies, e.g. for compensating magnetic field disturbances [Sabatini and Member, 2006, Roetenberg et al., 2005]. Since a KF implementation tuned for human motion tracking was already available from our commercial IMU system and with known values for accuracy performance, to the purpose of validation this filter was used as representative for this class of algorithms.

Experimental protocol

The full set of 6 IMU devices were tested together for performance evaluation under repeatable and controlled conditions generated by accurate robotic manipulator. Prior to any data collection, the robot slowly rotated the attached sensors in all directions and at slow speed, in order to warm-up the electronics. Since the use of a robotic manipulator in close proximity to magnetic sensors

4.2. MATERIALS AND METHODS

55

can generally be detrimental to IMU orientation tracking performance due to perturbation of the surrounding magnetic field induced by motor driving and ferromagnetic components [Bachmann et al., 2007], a preliminary quantification of the magnetic disturbances was carried out in order to verify whether that is the case with our setup. Disturbances generated by the robot were found to be negligible and details of the procedure are reported in section 4.2.

The experimental protocol includes both a dynamic and a static accuracy assessment. The dynamic validation part of the protocol tests the IMUs under a sinusoidal excitation pattern generated for the angular displacement (θ) of the robot EE, that is:

$$\mathbf{q}_{EE}(t) = [\cos(\frac{\theta}{2}) \quad \mathbf{v} \sin(\frac{\theta}{2})] \quad (4.1)$$

$$\theta(A, t) = A \sin(2\pi ft) \quad (4.2)$$

where $\mathbf{q}_{EE}(t)$ is the time varying orientation of the EE expressed as a quaternion of angle θ and constant axis of rotation \mathbf{v} . The angle of rotation oscillates in time as a sinusoidal wave with amplitude (A) and frequency (f), that were varied in order to generate the matrix of tests reported in table 4.1. The set of frequency comprises 7 values equally spaced on a logarithmic scale in the bandwidth of human motion and range from a minimum of 0.18 Hz to a maximum of 5.6 Hz. The interval was selected in order to provide good coverage of the range of frequencies typically found in human movements, which is limited in the bandwidth up to 5 Hz, e.g. during gait [Barralon et al., 2005, Godfrey et al., 2008]. Moreover, the predominant component of the frequency spectrum for common activities of daily living (ADL) is found in the literature to be around 1 Hz and with 75% of the spectral energy below 5 Hz [Mann et al., 1989]. Instead, the choice for excitation amplitude values was limited by a safety constraint on the maximum torque that can be generated at the joint level for the given payload with the robotic arm. A set of 6 amplitudes was considered varying from a minimum of 6° to a maximum of about 36° peak to peak. A staircase pattern for the matrix of excitation is obtained and it is reported in table 4.1. All the dynamic rotations of the protocol were generated as single joint or double aligned joints mono-axial rotations. Each dynamic excitation was applied for a 20 s time duration. It was then followed by a rest period of 40 s before the application of the subsequent excitation signal. The rest period was necessary to guarantee any transitory effect from former excitation to be exhausted and the algorithm for orientation estimation to be at convergence prior the application of a new excitation. The matrix of tests was repeated for 3 different trials in which the robotic arm ${}^E\vec{Z}$ axis was aligned

CHAPTER 4. VALIDATING ACCURACY OF INERTIAL ORIENTATION TRACKING

Table 4.1: Matrix of excitations for dynamic accuracy validation: row-wise are amplitudes in and column-wise are frequencies

$^{\circ}\backslash\text{Hz}$	0.18	0.32	0.56	1.00	1.78	3.16	5.62
± 3	■	■	■	■	■	■	■
± 6	■	■	■	■	■	■	■
± 5	■	■	■	■	■	■	
± 10	■	■	■	■	■	■	
± 9	■	■	■	■	■		
± 18	■	■	■	■	■		

respectively with the ${}^W\vec{X}$, ${}^W\vec{Z}$ and $({}^W\vec{X} + {}^W\vec{Z})$ axis of the world reference frame ${}^W\text{SR}$ (see Figure 4.1) and the axis of rotation of the applied excitation signal was approximately oriented: perpendicular ($90.2 \pm 0.97^{\circ}$) with respect to the gravity, parallel ($0.9 \pm 0.56^{\circ}$) to it and midway between the two conditions ($44.7 \pm 1.27^{\circ}$). This allows to validate the IMUs performance separately for the *attitude*, the *heading* and for a mixed condition termed *attitude and heading*. Each condition was repeated for 5 times, up to a number of 90 different datasets ($3 \text{ trials} \times 5 \text{ repetitions} \times 6 \text{ IMUs}$) for each element in Table 4.1.

The static performance assessment part of the protocol explores two different static conditions for the sensing unit, denoted as PS (Pure Static) and SaM (Static after Motion). The PS test pertains accuracy evaluation when the IMU device is kept stationary for a period of 1 hour and aims to quantify the nominal stability of the orientation estimate. Instead, the SaM test evaluates static behaviour of the orientation computed by the IMUs after a dynamic excitation has been applied. The purpose of this set of tests is to determine what is the convergence of the error in the attitude and heading estimate to be expected after a dynamic condition is terminated, that is how fast the filter is capable of recovering a stable, static estimate of orientation. Specifically, excitations selected for this part of the protocol are the ones corresponding to the minimum and maximum dynamics, i.e. element (1, 1) and (6, 5) of the test matrix in Table 4.1, for the *attitude*, *heading* and *attitude and heading* trials described above. The orientation is evaluated over a period of 30 s, started after 0s from the extinction of the applied dynamic excitation. A number of 5 datasets for the 6 IMUs is collected for each trial and type of dynamics.

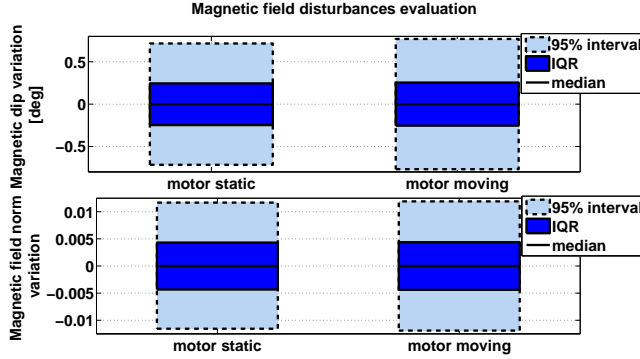


Figure 4.2: The figure reports variation of the magnetic dip angle (top) and of the magnetic norm (bottom) expressed as median, inter quartile range and 95% confidence interval. The first bar represents data obtained with no motion of the robot motors while the second are the data recorded during motor driving.

Magnetic field disturbances evaluation

In this paragraph details are reported on a preliminary experiment aimed at evaluating the effect of using the KUKA LWR 4+ robotic manipulator on the magnetic field sensed by IMU's magnetometers. Robot's housing is made of Aluminium, stainless steel (paramagnetic materials) and ABS plastic. Therefore, the only active source of magnetic field disturbance related to the use of the robotic arm is due to permanent magnets in motors and electro-magnetic waves generated by motor driving. In order to isolate this effect on the proposed sensors setup of Figure4.1, the robot was set to a fully extended configuration, namely "candle" configuration. Then, a pair of aligned robot joints (E1 and A6 w.r.t Figure6.1) were driven with a counterphase sinusoidal input. In this way the IMUs are kept static while robot motors are instead moving and perturbation nearby magnetic field. Particularly, each of the involved joint was driven with a set of sinusoidal input, sharing the same amplitude and frequency but with a 180° phase shifting. In practice, the occurrence of this condition strongly relies on the assumption that commands to the joints are sent in a synchronous way by the robot controller which, in turn, for a fixed amplitude of motion, is dependent on the frequency of the commanded excitation. The perturbation on the magnetic field was evaluated in terms of its effect on the

CHAPTER 4. VALIDATING ACCURACY OF INERTIAL ORIENTATION TRACKING

variation both of the ℓ^2 -norm of the magnetic field and of the magnetic dip angle. The latter depends on the position on Earth's surface (between 60 and 70 degrees at the actual latitude) and can be computed from the accelerometer and magnetometer measurements as:

$$\theta_{dip} = \frac{\pi}{2} - \cos^{-1}\left(\frac{\mathbf{g}_B \cdot \mathbf{m}_B}{\|\mathbf{g}\|_2 \|\mathbf{m}\|_2}\right) \quad (4.3)$$

where \mathbf{g}_B and \mathbf{m}_B are the gravity vector (measured by accelerometer in static condition) and the magnetic flux vector in sensor body frame (B). In fact, the variation of this quantities in time, defined as:

$$\Delta_{\theta_{dip}}(t) = \theta_{dip}(t) - \theta_{dip}(t - T_s) \quad (4.4)$$

$$\Delta_{\|\mathbf{m}\|_2}(t) = \|\mathbf{m}\|_2(t) - \|\mathbf{m}\|_2(t - T_s) \quad (4.5)$$

where T_s is the IMU sampling time, is the input to magnetic field disturbances compensation strategies that are typically integrated in the orientation estimation framework of an IMU, as discussed in [Roetenberg et al., 2005]. Experimental results for a 40 s motor static period followed by a 40 s counter phase motor moving (60° peak-to-peak amplitude at 0.5 Hz) are reported in Figure4.2. A slight increase in the IQR for the dip angle variation (+3%) and the magnetic field norm variation (+1%) is observed. Since distribution of $\Delta_{\theta_{dip}}$ and $\Delta_{\|\mathbf{m}\|_2}$ is not Gaussian, a Wilcoxon rank-sum test was used for the analysis of results. No statistical difference between the “motor static” and the “motor moving” groups is observed with a 5% significance level ($p > 0.95$).

Data analysis

The dataset resulting from a trial is composed by a sequence of unit norm quaternions describing IMU body frame (B) orientation with respect to a global, fixed, geo-magnetic reference frame (G), i.e. ($^{GB}\mathbf{q}$), and sampled at 128 Hz. A companion sequence of quaternions is obtained from the robotic arm, i.e. ($^{WE}\mathbf{q}$), relating the orientation of the EE frame (E) to the robot world frame (W) that is fixed on the basis of the platform as shown in Figure4.1 and sampled at 200 Hz. Prior to any performance evaluation, collected datasets from robot and IMUs were resampled at a constant rate of 128 Hz. Resampling on the quaternion space was carried out by using quaternion spherical linear interpolation (SLERP) [Shoemake1985, 1985]. Data synchronization was obtained fitting a linear model (clock offset and skew) from measurements of correlation of the angular velocity ℓ^2 -norms data from IMU and robot at different time

4.2. MATERIALS AND METHODS

59

intervals. Each measurement of correlation provides an estimate of the delay relating a pair of time instants (t_I, t_R) , respectively referred to the IMU and robot clocks. Multiple pairs were robustly fitted with a linear model using the RANSAC algorithm [Hartley and Zisserman, 2000].

The metric on quaternion space was defined as:

$$\Phi(\mathbf{q}_A, \mathbf{q}_B) = 2 \cos^{-1}(|\mathbf{q}_A \cdot \mathbf{q}_B|) \quad (4.6)$$

and can be interpreted as the length of the shortest path, i.e. a geodesic, connecting the two quaternions $(\mathbf{q}_A, \mathbf{q}_B)$ on the 4-dimensional hypersphere where they are defined (more details are reported in section 4.3). In order to consistently evaluate accuracy with this metric, IMU and robot quaternion sequences need first to be aligned in such a way they are referred to the same system of coordinate, i.e.:

$${}^{WG}\mathbf{q} \otimes {}^{GB}\mathbf{q}(t) = {}^{WE}\mathbf{q}(t) \otimes {}^{EB}\mathbf{q} \quad (4.7)$$

where the additional constant quaternions ${}^{WG}\mathbf{q}$ and ${}^{EB}\mathbf{q}$ represent relative frames misalignments. The problem of aligning reference frames from sequence of measurements of the same quantity is well described in the robotics literature, known as hand-eye calibration, and for our case the method in [Horn, 1987] was used to estimate the unknown pair $({}^{WG}\mathbf{q}, {}^{EB}\mathbf{q})$. Preprocessed datasets were analysed to extract two different performance indexes of orientation tracking: absolute accuracy and relative accuracy. Absolute accuracy (ϵ_A) determines the capability of each IMU to correctly estimate orientation against an absolute reference measure. Mathematically, it is evaluated as:

$$\epsilon_A = \Phi(\mathbf{q}_{I_i}, \mathbf{q}_{GT}) \quad , \quad i = 1, \dots, 6 \quad (4.8)$$

where, \mathbf{q}_{I_i} is the measure from i -th IMU and \mathbf{q}_{GT} is the ground truth data coming from the robotic platform. For each test on the matrix in Table 4.1, 30 datasets of absolute accuracy measures are computed (5 repetitions \times 6 IMU units).

Instead, relative accuracy (ϵ_R), accounts for differences in estimated orientation between pairs of IMUs and independently of the actual orientation value. It is a crucial parameter to consider for all applications where relative motion is of interest, e.g. for human joint angle measurement. It is computed as:

$$\epsilon_R = \Phi(\mathbf{q}_{I_i}, \mathbf{q}_{I_j}) \quad , \quad i \neq j \quad (4.9)$$

CHAPTER 4. VALIDATING ACCURACY OF INERTIAL ORIENTATION TRACKING

where, for each test on the matrix in Table 4.1, all the possible combinations of IMU pairs generate a number of 75 datasets of relative accuracy measurements ($5 \text{ reps} \times 15 \text{ measures per rep.}$).

4.3 Metric on SO3 space

Quaternions are the preferred choice for formulating orientation estimation algorithms with IMU devices as they come with advantageous properties like computational and spatial efficiency and non-singularity of representation. Quaternions avoid trigonometric functions in the filtering algorithm, making it more efficient and suitable for real-time implementation on embedded computers. Further, issues related to round-off errors, due to limited precision of practical implementations on computers, can be easily solved by re-enforcing the unit norm constraint and with a reduced computational cost (e.g. compared to the orthonormalization of a 3×3 rotation matrix). The drawback of using quaternions is that orientation is not uniquely defined as they provide a double covering of the Special Orthogonal group (SO3) where 3D orientations are defined (i.e. \pm symbol in equation (A.1)). Therefore, proper care must be taken in order to measure distance between quaternions. In this work the metric was defined as:

$$\Phi(\mathbf{q}_A, \mathbf{q}_B) = 2 \cos^{-1}(|\mathbf{q}_A \cdot \mathbf{q}_B|) \quad (4.10)$$

where the \cdot symbol denotes vector scalar product, i.e.:

$$\begin{aligned} \mathbf{q}_A \cdot \mathbf{q}_B &= q_{0A}q_{0B} - \vec{\mathbf{q}}_A \cdot \vec{\mathbf{q}}_B \\ &= (1 - \frac{\alpha}{2}) \cos(\frac{\Delta\theta_{AB}}{2}) - \frac{\alpha}{2} \cos(\frac{\theta_A + \theta_B}{2}) \end{aligned} \quad (4.11)$$

and the symbol α was used to denote the scalar product of the axis of rotation ($\vec{\mathbf{v}}_A, \vec{\mathbf{v}}_B$) and the term $\Delta\theta_{AB}$ is referred in the literature as range of motion (ROM). The function $\Phi(\cdot)$ returns a value in the range $[0, \pi]$ and it is a bi-invariant metric in the SO3 group that can be interpreted as the length of the shortest path, i.e. a geodesic, connecting two quaternions on the 4-dimensional hypersphere where they are defined [Huynh, 2009].

4.4 Results

Reported data throughout this section were displayed as the median, the inter quartile range (IQR) and the 95% range or upper bound (UB) for the data,

4.4. RESULTS

61

which is defined using the 95th quantile. This choice is motivated by the fact that, due to the characteristic of the metric on quaternion space defined in (4.6) (e.g. it only allows for positive values of the error), data distribution is skewed and it is generally not uniquely identifiable with a specific type of parametric distribution. In view of the above, data were reported in the following using more reliable measure of central tendency (median), statistical dispersion (IQR) and confidence interval (defined using quantiles).

Static accuracy

Experimental datasets were collected from the 6 IMU devices according to the described protocol for the static accuracy evaluation. In Figure 4.3, results for the PS trial are reported. Each bar represents the total distribution of the error in orientation that includes all the IMUs under test, on which both the KF and the CF algorithms were run to estimate orientation. For the absolute accuracy a median value of 0.44° (KF) and 0.25° (CF) was obtained while the UB on this error was found to be 1.18° (KF) and 1.17° (CF). For the relative accuracy slightly higher median values were obtained, 0.58° (KF) and 0.32° (CF), while the UB was found to be 1.46° (KF) and 1.04° (CF). Moreover, the IQR resulted increased passing from absolute to relative accuracy, respectively of the 20% for KF and of the 8% for the CF filter. Significance of results was

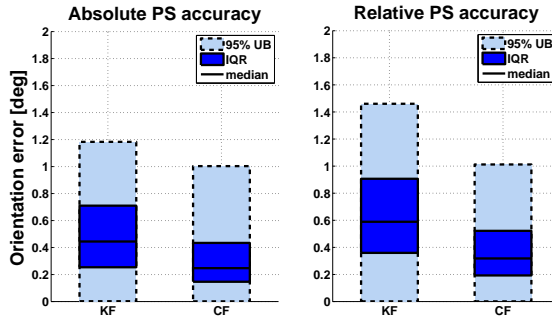


Figure 4.3: The figure reports absolute (left) and relative (right) accuracy expressed as median, inter quartile range and 95% confidence interval for the *pure static* (PS) trial of static part of the protocol. The first bar represents data obtained with the KF fusion and the second is the data obtained from the non-linear complementary filter approach (CF).

CHAPTER 4. VALIDATING ACCURACY OF INERTIAL ORIENTATION TRACKING

62

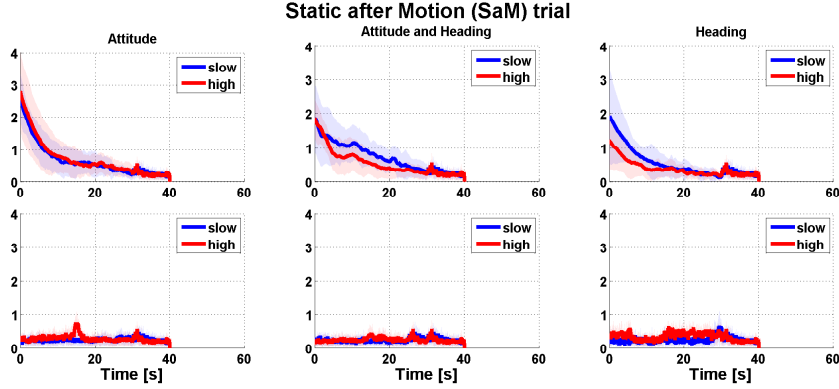


Figure 4.4: The figure reports results for the static after motion (SaM) trial defined over a time interval of 30 s starting at the extinction of the dynamic excitation. The solid line represents the median of the orientation error and the boundaries (dashed line) are its associated inter quartile range. Graphs are organized according to the type of trial (*attitude*, *attitude and heading*, *heading*), the sensor fusion algorithm selected (*KF* or *CF*) and the type of dynamic excitation considered (*slow* and *fast*).

investigated using Wilcoxon rank-sum test under the verified non gaussianity assumption of the datasets. Median values for the error of each IMU were considered in the analysis and a significant effect of the filter was found ($p < 0.05$), favouring the CF algorithm in the static case. In Figure 4.5 the results for the SaM trial part of static accuracy validation are reported. Each row in the graph is associated with either the KF sensor fusion (top) or the CF (bottom), while each column identifies one of the 3 experimented conditions for the former dynamic excitation (i.e. *attitude*, *attitude and heading*, *heading*). The plots represent the trend in convergence of the orientation error from the end of a dynamic excitation (at time 0 s) to a stable, static estimate. A neat difference in the convergence rate of the two sensor fusion algorithms used is observed: the KF algorithm takes 10 s to reach a stable estimate (within 1°) independently of the type of trial, dynamics or whether we are considering absolute or relative orientation. Instead, the CF algorithm results in a noisier (due to the optimization step), but stable convergence already at the beginning of the static stage.

Dynamic accuracy

The full set of 6 IMU devices was tested for dynamic accuracy assesment with the matrix of excitations reported in Table 4.1. Outcome of the dynamic validation is reported as grafical representation in Figure4.5 for the absolute accuracy and in Figure4.6 for the relative accuracy. Each figure displays results obtained with the KF approach, on the left column, and results obtained with the CF algorithm, on the right column. Errors are reported as the median value (black line) and the UB (colored box). Each box encodes the cumulative distribution of the error, i.e. comprising all the datasets for the specific type of trial and element of the matrix in Table 4.1. The graphical representation provides a visual overview of trends in orientation error under the different dynamic conditions specified for each trial. Besides graphical representations, numerical values for the median and the 95% UB are also provided in tables as supplementary material. Statistical analysis was performed in order to investigate the effect of the following independent variables:

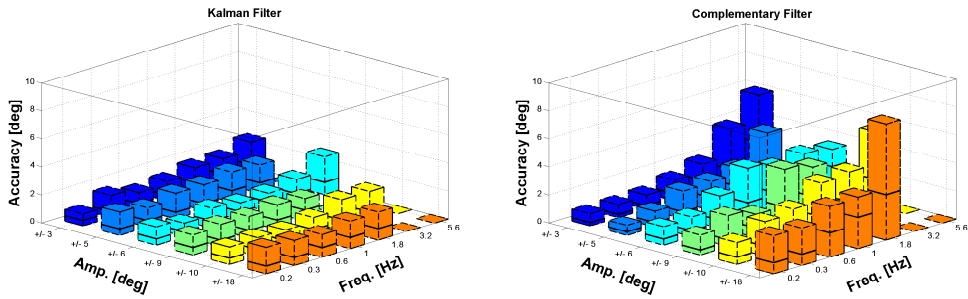
- type of sensor fusion algorithm;
- type of accuracy metric (i.e. absolute or relative);
- type of frequency;
- type of amplitude;
- type of rotation w.r.t gravity (i.e. *attitude*, *heading* or *attitude and heading* trial);

The level of significance (α) was set to 0.05 for all statistical tests. Further, median value of the error during the 20 s of dynamic excitation was considered in place of the full dataset in order to reduce the numerosity of the population to a number of 30 and 75 samples, respectively for absolute and relative error measurements, for each type of trial and element of the matrix 4.1. The statistical significance of the effects was investigated with the following procedure: first, the hypothesis of non Gaussianity was verified using a Lilliefors test. Then, for pairwise comparisons a Wilcoxon rank-sum test was used. Instead, for the analysis in case of multiple groups a Kruskal-Wallis one-way ANOVA was considered, followed by post-hoc comparisons with Tukey-Kramer correction. Considering the type of sensor fusion algorithm variable, the KF algorithm performed slightly better than the CF with respect both to the absolute accuracy (median value of 0.47° and 0.77° respectively) and to the relative accuracy (median value of 0.48° and 0.83° respectively) with a statistical significance $p < \alpha$.

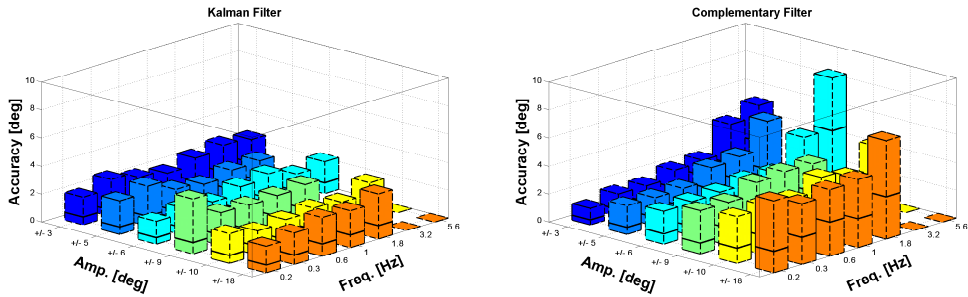
CHAPTER 4. VALIDATING ACCURACY OF INERTIAL ORIENTATION TRACKING

64

(a) *Attitude tracking trial*



(b) *Attitude and Heading tracking trial*



(c) *Heading tracking trial*

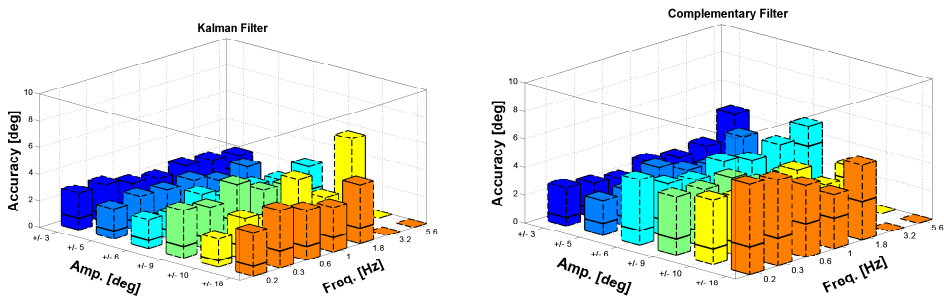


Figure 4.5: The figure shows the results for absolute accuracy obtained with the KF algorithm (left column) and CF algorithm (right column). Absolute accuracy is represented as the 95% error range (colored box) and the median value of results (solid black line).

4.4. RESULTS

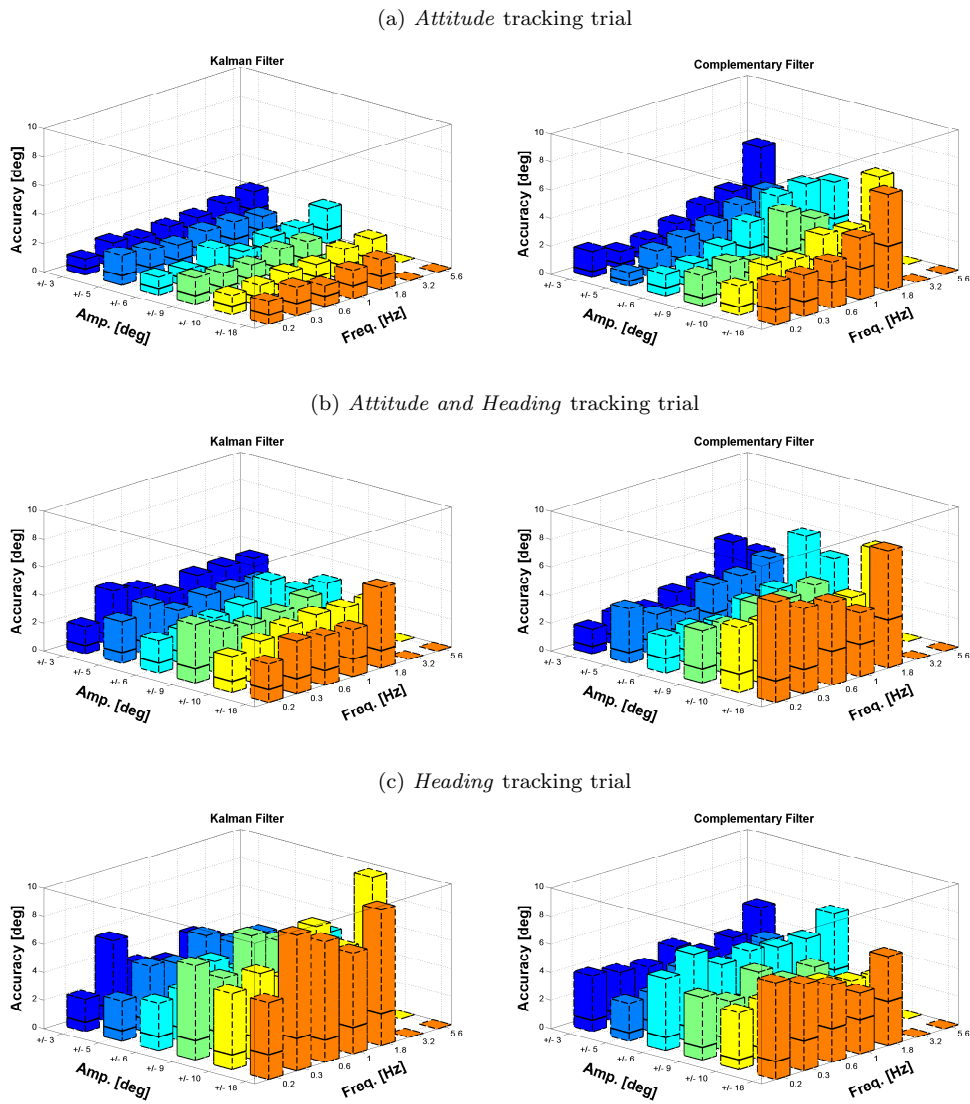


Figure 4.6: The figure shows the results for relative accuracy absolute obtained with the KF algorithm (left column) and CF algorithm (right column). Relative accuracy is represented as the 95% error range (colored box) and the median value of results (solid black line).

CHAPTER 4. VALIDATING ACCURACY OF INERTIAL ORIENTATION 66 TRACKING

Also, a significant effect was found for the type of accuracy metric variable. In this case, orientation errors to be expected from an IMU were lower when absolute accuracy was considered rather than relative accuracy. The statistical effect of the type of frequency variable on the orientation error was found to be significant ($p < \alpha$). Post-hoc analysis on the groups pertaining to this variable (i.e. the 7 frequency considered in the experimentation) identified a number of sets: elements within the same set had no significantly different effect on the orientation error while elements from different sets had. For the case of KF those sets were: $\{0.18, 0.32, 0.56, 1.00\}$ and $\{1.78, 3.16, 5.62\}$, where all the values are expressed in Hz. For the case of CF the following groups were identified: $\{0.18, 0.32\}$, $\{0.56\}$, $\{1.00, 1.78, 3.16\}$, $\{5.62\}$ and all the values are expressed in Hz. Varying the amplitude of excitation had a significant effect on the error ($p < \alpha$). Similarly to the case of the frequency variable, the post-hoc analysis produced a number of different sets, that in this case were the same for the KF and CF algorithm: $\{\pm 3\}$, $\{\pm 5\}$, $\{\pm 6\}$, $\{\pm 9, \pm 10\}$ and $\{\pm 18\}$. In addition to that, the median error in orientation tends to grow with the increasing value of frequency and amplitude considered in the protocol and independently of the sensor fusion algorithm. A visualization of this trend is displayed in Figure 4.7 and 4.8, respectively for the KF and CF algorithms. Finally, the type of trial, i.e. the orientation of the axis of rotation, was found to impact significantly the orientation error and median accuracy were 0.7° , 1.4° and 1.0° , respectively for *attitude*, *heading*, *attitude and heading* case.

4.5 Discussion

This paper presented a systematic study of IMU accuracy in estimating the orientation, in the range of movement dynamics typical of human motion. In consideration of the fact that all the present studies provide discordant results, mainly obtained without a well-controlled experimental setting and protocol, the objective of the work was to provide the scientific community with a reliable baseline for the performance achievable with this technology. Also, contrarily to most of existing studies that report sensor accuracy in terms of RMS or average errors, the results are rather presented considering a 95% UB which is computed basing on error distribution quantiles. Existing literature on the topic has proposed 2 major approaches to perform this validation: the first employs either manually operated or motor controlled mechanical systems (e.g. motorized gimbal Table [Lebel et al., 2013], pendulum [Brodie et al., 2008c, Godwin et al., 2009], plexiglas plank) while the second carries out the

4.5. DISCUSSION

67

assessment directly on human subjects [Luinge et al., 2007, Bergamini et al., 2014], usually relying on stereophotogrammetry as a reference measure. Motivation supporting the first approach is the elimination of error sources that are due to the human factor (e.g. soft tissue artifact, sensor misalignments) in order to isolate limitations inherent with the use of an IMU. Instead, the second approach to validation is motivated by providing a more realistic scenario for human motion related application. Our assessment exploits the benefits of the first approach by using a robotic platform, which guarantees controlled and repeatable experimental conditions that are more suitable for validation purpose, while generating excitations in the bandwidth typically observed in human motion (in pursuance of simulating a realistic dynamics). The presented experimental protocol comprised both static and dynamic accuracy assessment. Different level of dynamic excitation are experimented and accuracy is evaluated both as an absolute quantity, compared to orientation measured with the robotic platform, and as a relative quantity, among pairs of IMU devices. In addition, orientation is obtained via sensor fusion algorithms that pertains to the 2 major classes of approaches found in the literature, i.e. the stochastic (KF) and the complementary filter approach (CF). Though care has been taken about providing clearance from ferromagnetic objects in the experimental setting, experimentation was purposely not carried out in a so called clean magnetic environment in order to be representative of a typical use case scenario. Nonetheless, disturbances specifically induced by the use of a robotic platform were quantified and found to be negligible. Evaluation of static accuracy is performed according to two different protocol named the *Pure Static* (PS) and the *Static after Motion* (SaM). The former protocol, or slight variations to that, are often found in related literature, e.g. in [Cutti et al., 2006, Brodie et al., 2008c, Godwin et al., 2009] and partly in [Lebel et al., 2013]. Main differences with our approach are in the error metric, which is commonly based on Euler angle components and thus highly dependent on the choice of the rotation axes sequence, and in dataset time duration, 10 s in [Cutti et al., 2006], 1 s in [Brodie et al., 2008c] and 30 s in [Lebel et al., 2013]. Therefore, we are only partially provided with benchmark values from literature. Also, specifications from vendor are expressed as Euler angles and with no detail about the assessment procedure. Despite those considerations, median errors that were reported comply well with the accuracy requirement of human motion capturing for both sensor fusion techniques and are smaller than vendor's specifications for the KF case. Also, our results also suggest good stability of static orientation estimate over a period of 1 hour and, as a consequence, of estimated bias instability components (e.g. affecting gyroscope

CHAPTER 4. VALIDATING ACCURACY OF INERTIAL ORIENTATION TRACKING

sensors), which are the major source of drifts in orientation estimate. The SaM protocol aimed at answering the following question: is convergence to a stable orientation estimate affected by the type of dynamics previously applied to the IMU? The major difference observed here is in the behaviour of the two algorithms. The CF algorithm has a fast convergence, driven by the GNA regression and it is immediately stable within a level of accuracy comparable to the PS trial. Instead, the KF approach requires a static period of about 10s to reach convergence, though it proves to be virtually independent of the previous excitation's magnitude and bandwidth and of the type of trial comprised in our testing protocol. The dynamic accuracy assessment of orientation tracking comprised a set sinusoidal excitations with varying frequency and amplitude. The assumption of periodic movements to be representative of human motion repertoire is not uncommon in the literature (e.g. in human gait) and has been used as modeling assumption for sensor fusion algorithms [Sabatini, 2005]. The novelty of our protocol implies there only are dodgy benchmark data in the literature or the dynamic accuracy specifications from vendor, that comes with no information on the assessment protocol. The only similar work in the literature is that of Lebel and colleagues [Lebel et al., 2013], where two different dynamic conditions are explored by varying a constant angular velocity excitation from a value of $90^\circ/\text{s}$ to $180^\circ/\text{s}$. Despite our protocol consider peak angular velocities varying from a minimum of $3^\circ/\text{s}$ to a maximum of about $200^\circ/\text{s}$, results in [Lebel et al., 2013] are obtained using an improper metric for quaternions (not a geodesic path) and thus their reliability is questionable. Our results showed that, independently from the fusion algorithm used, dynamic of movements do have an effect on the performance of the tracker with both algorithms experimented and as a general rule of thumb, the more the bandwidth and the amplitude, the more the error to be expected. Interestingly, a decrement of performance was observed when passing from performing rotation against the gravity to rotations along the gravity axis. In the latter case, both sensor fusion algorithm heavily rely on magnetic field measurements in order to limit orientation drifts. In case the magnetic field is locally perturbed (which is likely to be the case in indoor settings [Bachmann et al., 2007]), either wrong measurement are introduced in the sensor fusion framework or, in case the perturbation is detected, no reference measure at all is available to stabilize drift on the heading. In both scenarios, orientation estimate will be prone to errors. The same effect was observed in the study from Cutti [Cutti et al., 2006] and Bergamini [Bergamini et al., 2014], where higher angular errors were experienced for the IMU attached to the pelvis that was mainly subjected to rotations along the gravity vector during a walking session. It was

4.5. DISCUSSION

69

also found that, when considering relative orientation among IMU, level of error to be expected is increased. This result is in agreement with the discussion in [Picerno et al., 2011] and is motivated by the fact that each IMU tends to sense the reference geomagnetical and gravity fields in a slightly different way, due to deviations in the sensor's calibration parameters. Also, following the discussion by the same authors, the aforementioned effect can be rather mitigated than eliminated by an initial IMUs' reference frame alignment. With reference to the performance of the two sensor fusion algorithms used, the KF proved better in dynamic trials while the CF achieved a better static accuracy and with a faster convergence rate. Though numerical values of the error in both cases are still comparable, this result can be dependent on the tuning of the filters parameter (not available for the commercial IMU KF). Concluding, on the one hand IMU based human motion tracking represent a valuable alternative to accurate stereophotogrammetry as the worsor but limited level of errors (within 10° in the experimented cases) is traded off by the greater portability and flexibility. On the other hand, the maturity of the technology and the algorithms for human applications is still poor and a lot of insight is required from the experimenter in order to properly use IMU based systems and identify sources of error (e.g. starting from a proper metric for the error itself). In fact, sensitivity to magnetic disturbance is one of the main issue related to the use of this technology for orientation tracking. Evidently from the results, magnetic field compensation strategies currently explored in the literature, based on detecting magnetic norm or magnetic dip angle variations [Roetenberg,] and implemented in the sensor fusion algorithms used in this study, are not completely effective in a complex indoor environment. A solution to remove the problem is to calibrate magnetometers in the perturbed environment. However, this approach is only valid locally in space (and time in case of a changing scenario). Also, when relative measurements are of interest, e.g. for human body joint tracking, higher errors are to be expected. In this case, domain specific assumptions, e.g. related to natural bio-mechanical constraints of the human body, can be exploited in order to limit error drifts [Luinge et al., 2007].

CHAPTER 4. VALIDATING ACCURACY OF INERTIAL ORIENTATION TRACKING

70

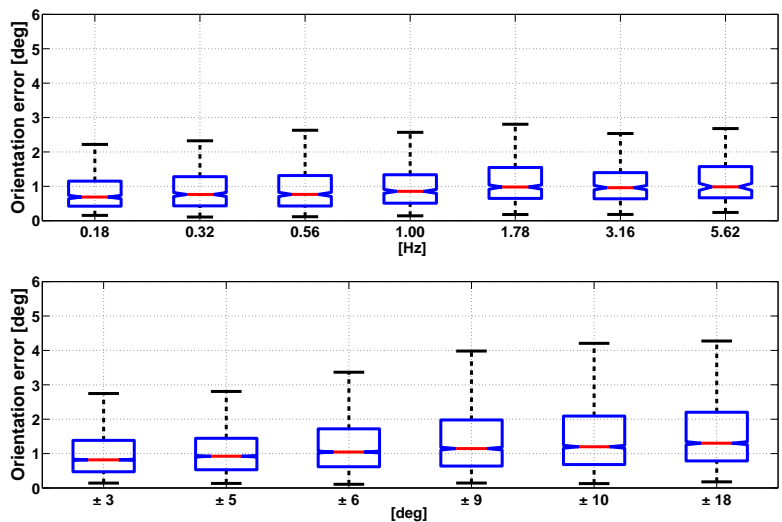


Figure 4.7: The figure reports trends in the absolute orientation error computed with the KF, for varying frequency of the excitation signal (top) and varying range of motion (bottom). Data are reported as the median value (red line), IQR (blue box) and minimum and maximum values (black whiskers). Outliers are removed from each dataset using a ± 3 IQR threshold.

4.5. DISCUSSION

71

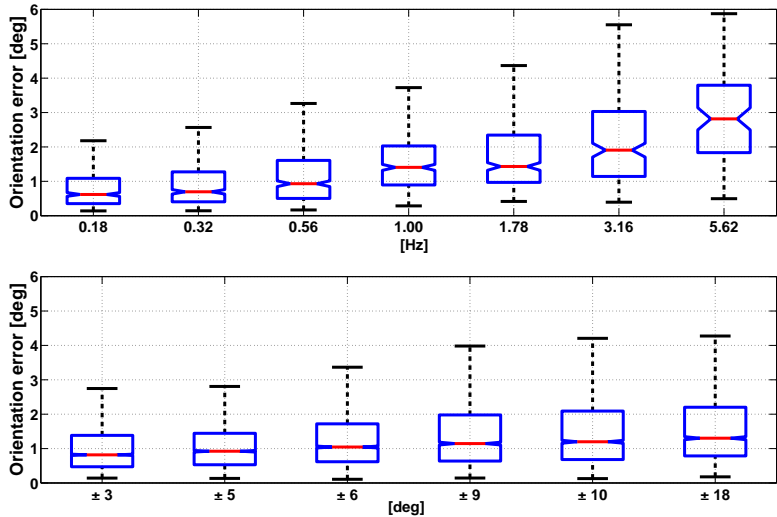


Figure 4.8: The figure reports trends in the absolute orientation error computed with the CF, for varying frequency of the excitation signal (top) and varying range of motion (bottom). Data are reported as the median value (red line), IQR (blue box) and minimum and maximum values (black whiskers). Outliers are removed from each dataset using a ± 3 IQR threshold.

Table 4.2: Dynamic accuracy table (reported values are in °)*

ABSOLUTE ACCURACY														
Attitude	0.18 Hz		0.32 Hz		0.56 Hz		1.00 Hz		1.78 Hz		3.16 Hz		5.62 Hz	
	KF	CF	KF	CF	KF	CF	KF	CF	KF	CF	KF	CF	KF	CF
±3°	0.4:1.0	0.3:0.9	0.5:1.8	0.3:1.0	0.5:1.5	0.3:1.0	0.4:1.5	0.5:1.5	0.7:2.0	0.9:2.0	0.7:2.0	1.0:3.9	0.8:2.5	2.3:5.7
±6°	0.5:1.6	0.4:1.3	0.4:1.0	0.4:1.4	0.6:1.9	0.6:2.3	0.7:1.5	1.3:3.7	0.7:1.8	1.3:3.1	0.7:1.8	1.8:3.5	1.0:3.5	2.0:3.2
±5°	0.5:2.0	0.3:0.7	0.5:1.7	0.4:1.2	0.5:1.9	0.5:2.0	0.5:2.0	0.9:2.0	0.8:2.3	1.1:2.4	0.8:2.3	1.7:4.3	—	—
±10°	0.5:1.7	0.5:1.6	0.5:1.8	0.7:2.4	0.5:2.1	1.0:2.8	0.7:1.9	1.6:4.0	0.9:2.6	2.1:4.2	0.8:2.6	3.0:6.4	—	—
±9°	0.6:1.7	0.4:1.4	0.5:1.9	0.5:2.2	0.6:2.0	0.7:1.7	0.7:2.3	1.6:4.3	0.9:2.4	1.8:3.8	—	—	—	—
±18°	0.6:2.1	0.8:2.7	0.6:2.1	0.8:2.7	0.7:1.9	1.7:3.6	0.8:2.3	2.2:3.7	0.9:2.5	3.3:8.3	—	—	—	—
AH. *	0.18 Hz		0.32 Hz		0.56 Hz		1.00 Hz		1.78 Hz		3.16 Hz		5.62 Hz	
	KF	CF	KF	CF	KF	CF	KF	CF	KF	CF	KF	CF	KF	CF
±3°	0.6:2.3	0.4:1.2	0.5:3.0	0.5:1.6	0.5:2.6	0.5:1.6	0.6:2.0	0.9:2.1	0.8:2.7	1.2:2.2	0.9:3.0	1.4:4.2	0.9:2.8	2.4:4.9
±6°	0.5:2.1	0.7:2.4	0.6:2.4	0.7:2.4	0.6:2.3	0.8:2.5	0.8:2.7	1.5:2.8	1.0:3.1	1.4:2.7	0.9:2.6	1.8:4.6	0.8:2.9	4.5:8.2
±5°	0.6:3.0	0.5:2.1	0.8:3.4	0.6:2.0	0.6:2.3	0.9:2.1	0.7:2.2	1.5:3.0	0.9:2.9	1.6:3.2	0.9:2.8	1.7:5.1	—	—
±10°	0.7:2.6	1.1:3.3	0.7:2.8	1.3:3.5	0.6:2.7	1.5:3.4	0.7:3.0	1.8:4.3	0.9:3.1	1.8:3.8	1.0:3.3	3.2:5.3	—	—
±9°	0.9:4.4	0.8:3.1	0.8:2.9	1.2:3.1	0.6:2.7	1.5:3.9	0.9:3.0	1.8:4.0	0.9:3.0	2.1:4.0	—	—	—	—
±18°	0.6:2.6	1.6:5.2	0.8:2.9	1.9:4.4	1.0:3.1	2.4:4.7	1.0:3.0	2.1:4.8	1.1:4.3	3.1:7.0	—	—	—	—
Heading	0.18 Hz		0.32 Hz		0.56 Hz		1.00 Hz		1.78 Hz		3.16 Hz		5.62 Hz	
	KF	CF	KF	CF	KF	CF	KF	CF	KF	CF	KF	CF	KF	CF
±3°	0.9:2.7	0.6:2.7	0.6:2.8	0.6:2.4	0.6:2.2	0.7:2.2	0.6:1.9	1.0:2.8	0.7:2.3	1.2:2.5	0.7:2.1	1.4:2.7	0.8:1.9	1.3:4.4
±6°	0.6:2.0	1.0:4.7	0.6:1.9	1.1:3.8	0.8:2.6	1.7:3.4	0.6:1.9	1.9:4.2	0.6:2.2	1.7:3.6	0.6:1.9	1.9:4.2	0.7:2.1	3.5:4.9
±5°	0.6:1.9	0.9:2.5	0.6:2.6	0.6:2.6	0.5:2.2	1.0:3.7	0.6:2.3	1.5:2.9	0.5:1.9	1.5:2.6	0.7:2.2	1.6:4.0	—	—
±10°	0.5:1.8	1.1:4.6	0.8:2.8	0.9:4.2	0.6:1.9	1.6:3.8	1.1:4.1	2.2:4.9	0.7:2.6	1.7:3.2	1.4:6.5	3.0:4.0	—	—
±9°	0.9:3.3	1.1:4.1	0.7:3.0	1.0:4.0	1.5:4.2	1.6:4.3	1.1:3.3	2.0:3.3	0.8:2.8	1.6:3.4	—	—	—	—
±18°	0.7:2.9	1.9:6.4	1.3:3.9	1.9:6.1	1.0:3.4	2.4:5.1	1.0:2.9	2.2:3.9	1.1:4.0	2.8:5.4	—	—	—	—

Table 4.3: Relative Accuracy Table (reported values are in °)

Attitude	RELATIVE ACCURACY											
	0.18 Hz		0.32 Hz		0.56 Hz		1.00 Hz		1.78 Hz		3.16 Hz	
	KF	CF	KF	CF	KF	CF	KF	CF	KF	CF	KF	CF
±3°	0.4:1.2	0.4:1.8	0.5:1.8	0.3:1.2	0.5:1.5	0.4:1.4	0.6:1.6	0.8:2.0	0.7:1.8	1.1:2.7	0.7:2.0	1.2:3.1
±6°	0.5:1.4	0.5:1.5	0.5:1.4	0.6:1.7	0.6:2.2	0.8:2.4	0.6:1.3	1.7:3.4	0.8:1.7	1.6:4.7	0.8:1.8	1.9:5.0
±5°	0.7:2.2	0.4:1.0	0.6:1.9	0.6:2.0	0.6:1.7	0.7:2.3	0.7:2.0	1.3:2.7	0.8:2.1	1.3:3.4	0.8:1.9	2.1:3.8
±10°	0.6:1.4	0.6:2.0	0.6:1.6	1.0:2.9	0.7:2.0	1.3:2.8	0.8:1.9	2.0:3.9	1.0:2.3	1.9:3.7	0.9:2.4	3.5:6.9
±9°	0.7:2.0	0.6:2.2	0.6:1.7	0.8:2.5	0.6:1.7	1.0:1.9	0.8:2.2	2.1:4.9	0.8:2.2	2.1:3.8	-	-
±18°	0.7:1.7	1.1:3.0	0.8:2.2	1.1:3.0	0.8:1.6	1.8:3.3	0.9:2.0	2.2:4.4	0.9:2.3	3.2:6.9	-	-
AH.*	0.18 Hz		0.32 Hz		0.56 Hz		1.00 Hz		1.78 Hz		3.16 Hz	
	KF	CF	KF	CF	KF	CF	KF	CF	KF	CF	KF	CF
±3°	0.6:2.2	0.5:1.8	0.8:4.2	0.6:2.2	0.9:3.8	0.6:2.1	0.8:2.9	1.1:2.6	1.0:3.4	1.3:2.8	1.1:3.4	1.6:5.0
±6°	0.7:2.5	1.0:2.6	0.9:2.6	0.9:2.7	0.7:2.9	1.0:2.3	1.1:3.3	1.6:3.3	1.3:4.4	1.8:3.6	1.1:3.2	2.1:6.8
±5°	0.8:3.2	0.8:3.9	0.9:3.7	0.9:2.9	0.8:2.8	1.1:2.4	0.9:3.4	1.7:3.8	1.3:3.4	1.9:3.9	1.0:3.2	2.0:4.5
±10°	0.9:2.7	1.3:4.6	0.9:3.5	1.4:4.4	0.9:4.0	1.9:4.2	1.0:4.3	2.2:4.3	1.1:4.0	2.5:4.4	1.3:3.9	2.7:7.2
±9°	1.0:4.4	1.0:3.7	1.0:3.5	1.3:3.5	0.8:3.1	2.1:4.4	1.1:3.5	1.9:4.2	1.1:4.1	2.2:4.6	-	-
±18°	0.9:3.1	1.5:7.1	1.1:4.2	1.7:6.0	1.1:3.8	2.4:5.9	1.3:3.8	2.3:4.5	1.3:6.5	3.5:8.4	-	-
Heading	0.18 Hz		0.32 Hz		0.56 Hz		1.00 Hz		1.78 Hz		3.16 Hz	
	KF	CF	KF	CF	KF	CF	KF	CF	KF	CF	KF	CF
±3°	0.7:2.2	0.8:3.9	1.0:5.7	0.6:3.6	0.9:3.5	0.8:3.4	0.9:3.1	1.2:4.2	1.1:4.4	1.1:3.2	1.0:3.2	1.3:3.6
±6°	1.0:3.3	1.0:5.1	0.9:3.5	1.0:6.3	1.2:5.0	1.4:4.9	1.1:3.7	2.0:5.3	1.1:3.6	1.8:5.0	1.0:3.6	2.2:4.9
±5°	0.7:2.5	0.6:2.7	0.9:4.6	0.7:2.7	1.2:4.2	1.1:3.9	1.3:5.4	1.3:2.8	1.2:4.5	1.3:3.3	1.1:4.5	2.0:4.1
±10°	1.0:5.1	0.7:4.1	1.7:6.0	0.9:4.2	1.4:4.9	1.4:4.5	2.3:8.2	1.7:4.5	1.6:6.0	2.0:3.9	2.7:10.3	2.0:3.6
±9°	1.4:6.4	0.9:4.4	1.3:5.1	0.9:3.6	2.1:7.3	1.9:5.1	1.8:6.3	1.5:3.9	1.5:5.5	1.5:4.2	-	-
±18°	1.7:5.2	1.3:6.9	2.3:9.4	2.2:6.1	1.6:7.8	2.4:5.5	1.9:6.9	2.4:4.3	2.2:9.4	3.1:6.3	-	-

* Accuracy is expressed as the **median value** : 95% range

**AH.: Attitude and Heading

Tesi di dottorato in Ingegneria biomedica, di Luca Ricci,
discussa presso l'Università Campus Bio-Medico di Roma in data 11/06/2015.
La disseminazione e la riproduzione di questo documento sono consentite per scopi di didattica e ricerca,
a condizione che ne venga citata la fonte.

Chapter 5

Single device for navigating an omnidirectional wheeled robot

The present chapter deals with the use of a single inertial measurement unit (IMU) as a motion tracker and focuses on the application to the class of robotic omnidirectional mobile platforms. Despite being attractive for its superior mobility capabilities, this class of robot is still of limited use in the research and industry fields due to additional difficulties related to its autonomous calibration and navigation. In the following, a novel solution is described that introduces an IMU as additional information source. It is presented a sensor fusion architecture that enables automatic calibration of the robot kinematics and improves accuracy and robustness of the motion tracking (e.g. against wheel slippage) in a dead-reckoning navigation framework. In the first section, an overview of issues related with the use of omnidirectional platforms and the motivations for the present research are provided. Then the experimental setup and the necessary mathematical modelling of the different components comprised in the system are detailed, followed by a description of the sensor fusion algorithms implemented. The chapter concluded with a discussion of the results, emphasizing the significance of the contribution to current state of the art.

5.1 Problem formulation

Mecanum or Omni-wheels provide an elegant solution for implementing omnidirectional motion capabilities on ground vehicles. The very first prototype

CHAPTER 5. SINGLE DEVICE FOR NAVIGATING AN OMNIDIRECTIONAL WHEELED ROBOT

76

(a) Omni and Mecanum wheels

(b) Airtrax Sidewinder lift truck



Figure 5.1: The figure reports the two typical mechanical layouts that are featured by an omnidirectional wheel (a): *Omniwheel* type is displayed on the top and *Mecanum* or *Swedish* wheel is displayed on the bottom. On the right (b), an example of a commercial vehicle equipped with omnidirectional wheels.

by J. Grabowiecki dates back to 1919 [?], while the modern omnidirectional wheel design was developed by Swedish inventor B. Ilon in 1973 [Ilon, 1975]. Compared to traditional wheels, their peculiar mechanical structure with extra subrollers mounted around main roller diameter (shown in Figure 5.1) allows for maximum *degrees of mobility* [Campion et al., 1996] as they can move at each time instant in any direction on the plane and without any need for reorientation. Therefore, being especially suited for tasks in environments congested with static and dynamic obstacles and narrow aisles, omniwheels have found a vast interest both documented as research papers in the literature, e.g. studying aspects related to kinematics and control [Britain and Engineering, 1987, Indiveri, 2009, Purwin and DAndrea, 2006] and exploring fields of application [Kim and Yi, 2009, Wakita et al., 2013, Wada, 2005] and advertised as commercial products, e.g. Airtrax [Vetexinc,] and youBot [KUKA,]. From a control theory standpoint, omnidirectional wheels are free from nonholonomic

5.1. PROBLEM FORMULATION

77

constraints that, on the contrary, affects conventional wheels and complicate path planning and autonomous navigation in general. However, superior mobility comes at a price. Minor disadvantages of omnidirectional type wheels regard the poor mechanical efficiency, due to the fact that not all wheels rotate in the direction of movement, and the higher losses from friction. Instead, a major disadvantage derive from the inherent slipping characteristics of the wheel which deeply affects the quality encoder based odometry. In fact, in [Killpack et al., 2010] is reported that wheel slip is very likely to occur for side-to-side translation and rotation movements. Since typical mobile robot navigation architectures highly relies on accurate odometry measurements [Martinelli et al., 2006], both by using it as the only source of information in dead-reckoning localization schemes and fused with other sensors, poorly predictable behaviour of the measurements is very detrimental to the overall performance of the localization system. For these reasons Mecanum or omniwheels are still a less attractive choice compared to conventional wheels, even for applications perfectly suited for them.

In this chapter limitations related to odometry measurements reliability are overcome by equipping a low cost, miniaturized IMU device on a custom mobile robotic platform endowed with Mecanum wheels. Specifically, the methods and algorithms developed in this chapter will address the following two problems:

Calibration: given the wheel velocities and the proprioceptive information from an inertial sensor, find the maximum a posteriori estimate for all the parameters relevant to robot kinematics;

Navigation: estimate the robot's pose relative to its environment from a set of sensor observations. This is referred as “the most fundamental problem to providing a mobile robot with autonomous capabilities” in the literature [Cox, 1991].

The material in this chapter is the first attempt in the literature to demonstrates the aiding value of an inertial sensor both in the calibration from scratch of all the parameters that are relevant to odometry and in the autonomous navigation for an omnidirectional ground platform. Despite without any external reference the position estimate is prone to drift (i.e. the inherent limitations of a dead-reckoning navigation scheme), a method to properly fuse inertial data and encoders readings in order to ameliorate navigation during position-denied updates is proposed. In addition, calibrated odometry data and inertial measurement are fused together in order to achieve robustness (e.g. against wheel

slippage) and a 3D aware motion tracking, improved w.r.t the typical assumption of a planar surface describing ground platforms configurations in space. Beforehand providing details of the method, a brief review of the relevant related literature on odometry calibration and navigation for ground vehicles is reported.

Related work

Despite a number of interesting research efforts aiming at exploiting information from an IMU in order to improve aspects related to calibration or navigation of ground vehicles is reported in the literature, none of them consider omnidirectional mobile platforms. In [Hardt von der et al., 1998] a general method for calibration based upon redundant sensor information was presented and applied to the problem of dead reckoning localization for a differential drive mobile robot. Besides odometry information available from encoders, the authors used a gyroscope and a magnetometers in order to obtain redundant information on the vehicle heading and calibrate the kinematics. Apart from redundancy, the value of inertial sensor in achieving robustness against non-systematic sources of error affecting odometry is generally recognized in the literature [Necsulescu et al., 1993, Fuke and Krotkov, 1996, Ojeda and Borenstein, 2002, Ward and Iagnemma, 2008, Yi et al., 2009] and algorithm have been proposed for different type of ground mobile platforms. In the late 90s, Borenstein and Feng presented the *Gyrodometry* method for fusing encoder based odometry with gyroscopes data [Borenstein and Feng, 1996]. The detection strategy for identifying non systematic errors (e.g. when travelling over uneven floors) was based on disagreement between the odometry readings and the gyroscopes and compensated by using only information from the latter source. Reported results on a differential-drive mobile robot suggested significant improvements of the method over bare odometry navigation. A different approach to navigation that relied only on IMU measurements and knowledge of the mobile vehicle model was presented in [Dissanayake et al., 2001]. In this work, the non-holomic constraints of a conventional wheeled mobile robot were used to improve dead reckoning navigation, by formulating them as additional input measurements to an information filter (IF) estimation framework. Though this method is not robust against slippage or vibrations, that cannot be neglected for land vehicles in most cases (e.g. in outdoor terrains), the advantage of the fusion with inertial information was demonstrated. With the purpose of extending the traditional 2D odometry approach (i.e. planar navigation surface assumption) to a real world settings (e.g. navigation over rough

terrains), Lamon and colleagues introduces the concept of *3D odometry* [Lamon and Siegwart, 2004] and applied their idea to a rover with a customly designed mechanical structure that was capable of sensing vertical displacements. They presented a method for combining information coming from an IMU and wheel encoders in order to achieve an estimate of the a rover configuration in 3D space. The sensor fusion scheme was based on an extended information filter (EIF) and they demonstrated the benefits of inertial sensing in correcting odometric errors and significantly improving the pose estimate. In a recent work by Collin [Collin, 2014] an inertial sensors was even used in place of wheel encoders as it was positioned on a car's wheel axis. Though this is an alternative approach for using an IMU on a mobile vehicle and the method proves advantages in terms of gyroscope bias removal and better odometry measurements, it has been demonstrated only for low dynamic motion on a smooth surface.

5.2 Materials and methods

Experimental setup

The setup devised in order to carry out the experiments is composed by a customly designed omnidirectional mobile robot, a commercial IMU and a number of different software and firmware components. The robot is an autonomous mobile platform powered by lead-acid batteries. Its kinematic structure consisted of four Mecanum type wheels mounted at the corners of a rectangular steel frame. Each wheel was mechanically connected to a high-torque stepper motor (model ST6918 by Nanotech) through a single stage gear reduction. Each motor was matched to an optical encoder and both were connected to a motor controller board. A CAN bus network was implemented onboard and linked the 4 motor controllers to a stack of Arduino boards, including a CAN bus shield and a Arduino UNO microcontroller board. On the latter, a customly developed firmware was flashed in order to send commands to the motor drivers (i.e. motor velocity in rate per minutes) and retrieve encoders readings at a maximum update rate of about 20 Hz. The microcontroller board was also connected to an onboard PC via USB/serial connection. The commercial IMU that was employed for the experimental trials was the Mti-30 by Xsens, whose salient features are reported in table 2.1. The unit provides measurements of magnetic flux alongside with velocity and orientation increments, that are computed from the gyroscope and accelerometer readings. A connection to the onboard PC was established via USB/serial protocol and data were streamed from the device at a rate of 100 Hz. The onboard PC was also connected via

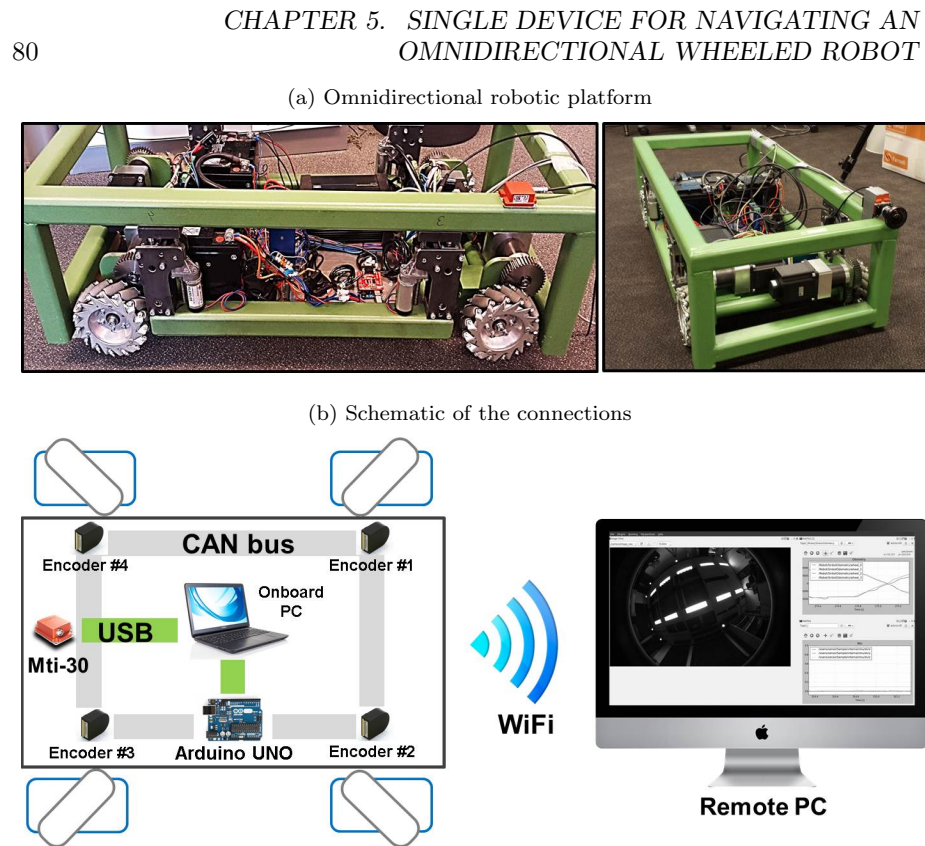


Figure 5.2: The figure shows the robotic platform devised for the experimental trials. On the top figure, two views of the platform are reported. On the bottom, a graph detailing the implemented networks of connection on the robot and with the remote PC.

WiFi to a base station for remote controlling of the robotic platform. On the software side, a number of C++ add-ons (namely *nodes*) were developed as part of the Robotic Operating System (ROS) framework [ROS,]. Implemented functionalities were relative to the interfacing with the IMU and the microcontroller, the robust data logging and the real-time visualization of measurements and a video stream from an onboard camera. Collected data logs were then imported into the Matlab environment where the proposed algorithms were

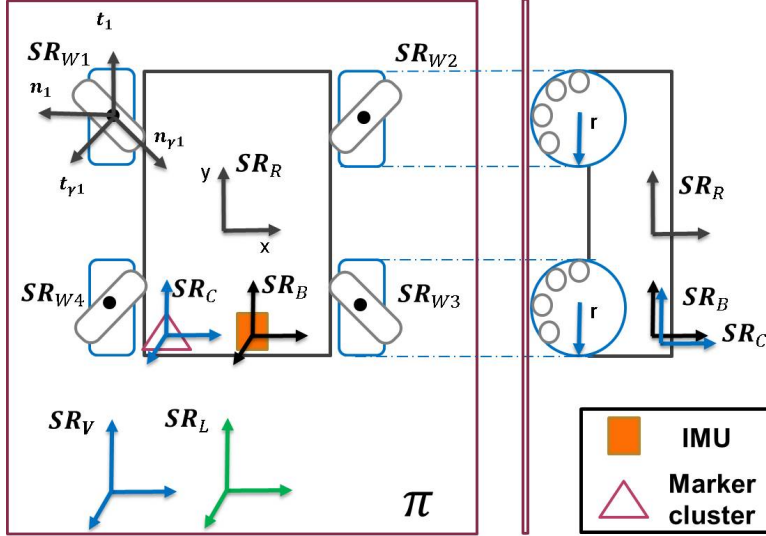


Figure 5.3: The figure reports the geometric model for our omnidirectional mobile robot.

implemented. In order to carry out the validation, all the experiments were conducted in a room equipped with a stereophotogrammetry system (Nexus by Vicon) composed by 6 IR cameras. Kinematic information of the IR markers (i.e. position and orientation w.r.t. a specified, fixed reference frame) that were attached to the robot frame were recorder at a rate of 100 Hz and exported in the Matlab environment. Finally, an overview of the platform and a diagram of the connections is shown in Figure 5.2.

Models

This paragraph introduces the mathematical models used to describe the available measurements and the kinematic characteristics of the robotic platform. All the systems of reference (SR) considered in formulation are defined in a 3D space and are reported in Figure 5.3, where the meaning of the subscripts is the following:

Body frame (B): this is the frame fixed on the IMU case that was

CHAPTER 5. SINGLE DEVICE FOR NAVIGATING AN OMNIDIRECTIONAL WHEELED ROBOT

previously discussed in section 2.3;

Local frame (L): the local navigation frame, defined upon the direction of the gravity vector and the geomagnetical field and detailed in section 2.3;

Robot frame (R): the robot frame is rigidly fixed on the robot chassis and have its origin in the geometrical center of the platform;

Wheel frame (W): the wheel frame is fixed on the robot chassis, but have its origin shifted to the wheels' centres (black dots in Figure 5.3);

Vicon frame (V): this is the reference frame with respect to IR markers measurements are expressed. It is set using a special set of markers during the initialization procedure of the stereophotogrammetric system;

Cluster frame (C): the cluster frame is built upon a set of 3 IR markers that are positioned in a rigid triangle configuration. This frame is rigidly attached to the robot chassis.

The last two introduced system of coordinates (i.e. the Vicon and the cluster frames) are only relevant to the validation part of the method. In addition, it is generally assumed that each pair of reference systems are related by an affine transformation T , such that:

$${}^B\tilde{\mathbf{y}} = {}^{BA}T \quad {}^A\tilde{\mathbf{y}} = \begin{bmatrix} {}^{BA}\mathbf{R} & {}^B\mathbf{d}_{BA} \\ 0 & 1 \end{bmatrix} {}^A\tilde{\mathbf{y}} \quad (5.1)$$

where ${}^{BA}\mathbf{R}$ indicates the rotation matrix defined in SO3 space and relating frame A to frame B, ${}^B\mathbf{d}_{BA}$ is the translation vector between the origins of frame B and A expressed w.r.t frame B and the symbol $\tilde{\mathbf{y}}$ is the homogeneous coordinates representation of a vector in 3D space, i.e. $\tilde{\mathbf{y}} = [y_x, y_y, y_z, 1]^T$.

IMU measurement model

The measurements provided by the IMU unit that will be used as input to the developed algorithms are an estimate of the current increment in rotation and in velocity and are modelled as follows. The increment in rotation ($\delta\mathbf{q} \in \mathbb{Q}_1$) is defined using the quaternion representation for the orientation, detailed in Appendix A. It is a 4-vector that relates the orientations of the body frames

5.2. MATERIALS AND METHODS

83

computed at two successive time instants. With respect to the angular velocity vector ($\boldsymbol{\omega} \in \mathbb{R}^3$) measured by the gyroscope triad, it is formalized as:

$$\delta \mathbf{q}_k = \exp\left(\frac{T_s \boldsymbol{\omega}_k}{2}\right) = \left[\begin{array}{c} \cos\left(\frac{T_s}{2} \|\boldsymbol{\omega}_k\|\right) \\ \frac{\boldsymbol{\omega}_k}{\|\boldsymbol{\omega}_k\|} \sin\left(\frac{T_s}{2} \|\boldsymbol{\omega}_k\|\right) \end{array} \right] \quad (5.2)$$

where T_s indicates the sampling time and it is implicitly assumed piecewise constant angular velocity behaviour within each discrete time interval. In a similar fashion, the increment in velocity ($\delta \mathbf{v}_k \in \mathbb{R}^3$) is a 3-vector relating the velocity of the body frames computed at two successive time instants. With respect to the specific force ($\mathbf{f} \in \mathbb{R}^3$) measured by the accelerometer triad it can be expressed as:

$$\delta \tilde{\mathbf{v}}_k = \delta \mathbf{q}_k \otimes T_s \tilde{\mathbf{f}}_k \otimes \delta \mathbf{q}_k^* \quad (5.3)$$

where the symbol \otimes denotes quaternion products and $*$ is the conjugate operator. Also, in order to carry out the quaternion and vector product $\tilde{\mathbf{f}}$ and $\delta \tilde{\mathbf{v}}$ are augmented 4-vector generated respectively from \mathbf{f} and $\delta \mathbf{v}$ as defined in (A.7). Note that velocity increments are derived from the proper acceleration and thus contain the gravity component that must be removed in order to extract the inertial velocity. In fact, the following relations were considered for propagating the inertial velocity and the orientation of the IMU body frame, both referred to the local frame (L):

$${}^L \mathbf{v}_{k+1} = {}^L \mathbf{v}_k + {}^{LB} R(\delta \mathbf{v}_k + \mathbf{e}_{v,k}) + T_s \mathbf{g} \quad (5.4)$$

$${}^{LB} \mathbf{q}_{k+1} = {}^{LB} \mathbf{q}_k \otimes \delta \mathbf{q}_k \otimes \exp\left(\frac{1}{2} \mathbf{e}_{q,k}\right) \quad (5.5)$$

where we indicated with $\mathbf{e}_{v,k}$ and $\mathbf{e}_{q,k}$ the realizations at the k -th time instant of an i.i.d Gaussian noise, respectively acting on the velocity and orientation propagation models. Furthermore, IMU sensors internal parameters are assumed calibrated except for constant biases terms acting on the gyroscopes and accelerometers and that were modelled as random walk processes:

$$\boldsymbol{\omega}_{b,k+1} = \boldsymbol{\omega}_{b,k} + \mathbf{e}_{b,k} \quad (5.6)$$

$$\mathbf{a}_{b,k+1} = \mathbf{a}_{b,k} + \mathbf{e}_{a,k} \quad (5.7)$$

where, with the same meaning as above, $\mathbf{e}_{b,k}$ and $\mathbf{e}_{a,k}$ are additive noise terms.

CHAPTER 5. SINGLE DEVICE FOR NAVIGATING AN OMNIDIRECTIONAL WHEELED ROBOT

84

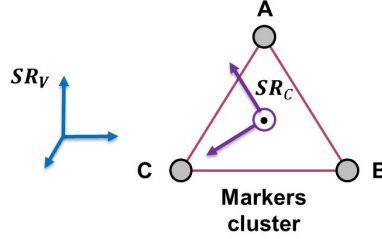


Figure 5.4: The figure shows the configuration of the markers' cluster whose position in space, w.r.t the Vicon frame (V), is used to define a local cluster frame (C) that is rigidly attached to the robotic platform.

Encoders measurement model

The raw measurement from the optical encoders, that are rigidly attached to each wheel's main hub axis, are the velocity of rotation of each motor expressed as number of steps per second (w.r.t the stepper motor). This quantity is measured before the gear reduction stage and thus a transmission ratio coefficient must be taken into account in order to extract the actual angular velocity of each wheel. The following linear relation was used to model measurements from the encoders:

$$\dot{\phi}_i = GC_{sr}s_i + e_e, \quad i = 1, \dots, 4 \quad (5.8)$$

where the term s is the step/s value measured by the i -th encoder and the quantity $\dot{\phi}$ is the i -th wheel angular velocity in rad/s. The conversions factors considered in the model are:

$C_{sr} \in \mathbb{R}$: it is the steps/s to rad/s ratio obtained from the stepper motor datasheet;

$G \in \mathbb{R}$: the transmission ratio, equal to $\frac{1}{12}$ for the robotic platform considered.

Finally, e_e is an additive noise term introduced in the measure.

Vicon measurement model

The stereophotogrammetric system measures the position in space of the IR markers w.r.t the Vicon frame. In the following tractation, the measurements

5.2. MATERIALS AND METHODS

85

of interest from this system are rather the instantaneous angular velocities and the linear velocities in the cluster frame (C). Those quantities were derived from position with the following steps. First, the local cluster frame must be defined. Given a set of 3 IR markers in triangular configuration as shown in Figure 5.4, the position of the origin (${}^C\vec{x}_O$) of the cluster frame was defined as the geometric center of the cluster, i.e.:

$${}^C\vec{x}_O = \frac{{}^C\vec{x}_A + {}^C\vec{x}_B + {}^C\vec{x}_C}{3} \quad (5.9)$$

The direction of the axis of the cluster frame were fixed by computing the rotation matrix relating the cluster frame to the vicon frame, i.e.:

$${}^{VC}\vec{R} = [{}^C\vec{x}_{B,A}, {}^C\vec{x}_{B,A} \times {}^C\vec{x}_{A,C}, {}^C\vec{x}_{B,A} \times {}^C\vec{x}_{A,C}] \quad (5.10)$$

where \vec{x}_{ij} denotes the versor connecting marker i to marker j . Given a time series of quaternions (${}^{VC}\vec{q}$), computed from the rotation matrices, the rotation increments can be obtained directly by inverting the relation presented in (5.5), i.e.:

$$\delta\vec{q}_k = {}^{VC}\vec{q}_k^* \otimes {}^{VC}\vec{q}_{k+1} \quad (5.11)$$

and the angular velocity in the cluster frame (${}^C\vec{\omega}$) can be extracted as:

$${}^C\vec{\omega}_k = 2 \frac{\log(\delta\vec{q}_k)}{T_s} \quad (5.12)$$

Instead, the linear velocity in the vicon frame can be obtained from discrete differentiation of position:

$${}^V\vec{v}_k = \frac{{}^V\vec{x}_{O,k} - {}^V\vec{x}_{O,k-1}}{T_s} \quad (5.13)$$

and from the latter, instantaneous velocity in the cluster frame (${}^C\vec{v}$) is eventually computed as:

$${}^C\tilde{\vec{v}}_k = {}^{VC}\vec{q}_k \otimes {}^V\tilde{\vec{v}} \otimes {}^{VC}\vec{q}_k^* \quad (5.14)$$

where $\tilde{\vec{v}}$ is the augmented vector of \vec{v} as defined in (A.7). As the measurements from the stereophotogrammetric system are considered as a reference to the aim of validating the algorithms, no additive noise term is considered in the model.

Robot kinematic model

In order to derive a model for describing the kinematic of the presented omni-directional mobile platform, the generalized formulation proposed in [Indiveri, 2009] was chosen as a starting point. According to the mathematical tractation there presented, an inverse differential kinematic model, i.e. that relates velocities expressed in the robot frame (SR_R) to the wheel speeds, can be derived from the following formulas:

$${}^{W_i}\mathbf{v}_{W_i} = {}^R\mathbf{v}_R + {}^R\mathbf{d}_{R,W_i} \times {}^R\boldsymbol{\omega}_R \quad (5.15)$$

$${}^{W_i}\mathbf{t}_i \cdot {}^{W_i}\mathbf{v}_{W_i} = r_i \dot{\phi}_i \quad (5.16)$$

where \cdot denotes the scalar product and, referring to the coordinate frames introduced in Figure 5.3, the following notation was used:

- $\mathbf{t}_i \in \mathbb{R}^3$ is the versor identifying the primary rolling direction for the i -th wheel;
- ${}^R\mathbf{d}_{R,W_i} \in \mathbb{R}^3$ indicated the lever arm from the robot frame to the i -wheel frame and is referred to robot frame;
- ${}^R\mathbf{v}_R \in \mathbb{R}^3$ and ${}^R\boldsymbol{\omega}_R \in \mathbb{R}^3$ are the linear and angular velocities of the robot in the robot frame;
- ${}^{W_i}\mathbf{v}_{W_i} \in \mathbb{R}^3$ is the linear velocity of the i -th wheel in the wheel frame;
- $r_i \in \mathbb{R}$ is the radius of the i -th wheel hub;
- $\dot{\phi}_i \in \mathbb{R}$ is the angular velocity measured at the i -th wheel.

Those formulas represents the relation between velocities expressed in the different frames that are defined on the robotic platforms, borrowed from classical mechanics, and the linear velocity that results from the rotation along its main axis of the Mecanum wheel. By substituting relation (5.15) into equation (5.16) and stacking into a matrix the equations for each wheel of the platform, one can derive the following formula:

$$\begin{pmatrix} \dot{\phi}_1 \\ \dot{\phi}_2 \\ \dot{\phi}_3 \\ \dot{\phi}_4 \end{pmatrix} = K' \begin{pmatrix} {}^B v_x \\ {}^B v_y \\ {}^B \omega_z \end{pmatrix} \quad (5.17)$$

5.2. MATERIALS AND METHODS

87

where the matrix K' encodes the inverse kinematic relation and is explicitly expressed as:

$$K' = -\frac{1}{r} \begin{pmatrix} n_{\gamma 1,x} & n_{\gamma 1,y} & {}^R\mathbf{d}_{R,W_1} \cdot W_1 \mathbf{t}_{\gamma,1} \\ n_{\gamma 2,x} & n_{\gamma 2,y} & {}^R\mathbf{d}_{R,W_2} \cdot W_2 \mathbf{t}_{\gamma,2} \\ n_{\gamma 3,x} & n_{\gamma 3,y} & {}^R\mathbf{d}_{R,W_3} \cdot W_3 \mathbf{t}_{\gamma,3} \\ n_{\gamma 4,x} & n_{\gamma 4,y} & {}^R\mathbf{d}_{R,W_4} \cdot W_4 \mathbf{t}_{\gamma,4} \end{pmatrix} \quad (5.18)$$

and with reference to Figure 5.3 the new terms introduced are defined as:

- $\mathbf{t}_{\gamma,i}$ is the versor identifying the sub-roller rolling direction for the i -th wheel
- $\mathbf{n}_{\gamma,i}$ is the normal versor to the i -th wheel subroller and parallel to its axis of rotation
- \mathbf{n}_i is the normal versor to the i -th wheel hub and parallel to its axis of rotation

When deriving the kinematic model above, the assumptions were made that the robot frame (R) has the z-axis orthogonal to the ground plane π (w.r.t to Figure 5.3) and that all wheels share the same radius dimension r . In practice, the latter assumption is really likely to be violated. Therefore, in agreement with the discussion in [Han et al., 2010], the presented model can be extended as follows:

$$K'' = \begin{pmatrix} 1/\alpha_{r1} & & & \\ & 1/\alpha_{r2} & & \\ & & 1/\alpha_{r3} & \\ & & & 1/\alpha_{r4} \end{pmatrix} K' \quad (5.19)$$

where the coefficient α_i accounts for variations from nominal value of the i -th radius. In view of the sensor fusion of encoder and inertial measurements, the relation given in (5.17) is expanded as:

$$\begin{pmatrix} \dot{\phi}_1 \\ \dot{\phi}_2 \\ \dot{\phi}_3 \\ \dot{\phi}_4 \end{pmatrix} = K'' \begin{bmatrix} \mathbf{I}_2 & \mathbf{0}_2 & \\ & 0 & 1 \end{bmatrix} \begin{bmatrix} \mathbf{I}_3 & {}^R\mathbf{d}_{RB} \\ & \mathbf{I}_3 \end{bmatrix} \begin{bmatrix} {}^{RB}\mathbf{R}_{xy} & \\ & {}^{RB}\mathbf{R}_{xy} \end{bmatrix} \begin{pmatrix} {}^B\mathbf{v} \\ {}^B\boldsymbol{\omega} \end{pmatrix} + \mathbf{e}_\phi \quad (5.20)$$

where the symbols $\mathbf{0}_2$ and \mathbf{I}_2 denotes the null and the identity matrix respectively and \mathbf{e}_ϕ accounts for measurements noise. The term ${}^{RB}\mathbf{R}_{xy}$ is a rotation

matrix acting along the x and y axis and compensating for any misalignment between the body frame and the robot frame z axes. Note that a term ${}^{RB}\mathbf{R}_z$ has not been included in the model as it can be demonstrated that it is not uniquely defined for the class of estimation problems presented in the next section. The linear $({}^B\mathbf{v})$ and angular velocities $({}^B\boldsymbol{\omega})$ in the formula are now computed from the IMU using the relations in (5.4) and (5.12). Refactoring the matrix products the presented relation can be rewritten as:

$$\begin{pmatrix} \dot{\phi}_1 \\ \dot{\phi}_2 \\ \dot{\phi}_3 \\ \dot{\phi}_4 \end{pmatrix} = K \begin{bmatrix} \mathbf{I}_2 & \mathbf{0}_2 \\ 0 & 1 \end{bmatrix} \begin{bmatrix} {}^{RB}\mathbf{R}_{xy} & {}^{RB}\mathbf{R}_{xy} \end{bmatrix} \begin{pmatrix} {}^B\mathbf{v} \\ {}^B\boldsymbol{\omega} \end{pmatrix} + \mathbf{e}_\phi \quad (5.21)$$

where the new matrix $K \in \mathbb{R}^{4 \times 3}$ now accounts for the lever arm term between robot reference frame and that of the IMU.

Additional modeling assumptions

In the development of the algorithms, additional constraints were exploited in order to better condition the problem. The first one was derived from the knowledge of the dynamic behaviour of the robotic systems: the wheels' motors driving can't generate any linear velocity along the vertical and any angular velocities along the roll and pitch axes w.r.t. the robot frame. This constraint was formulated as:

$$\begin{pmatrix} 0 \\ 0 \\ 0 \end{pmatrix} = \begin{bmatrix} \mathbf{0}_2 & \mathbf{I}_2 \\ 1 & 0 \end{bmatrix} \begin{bmatrix} \mathbf{I}_3 & {}^R\mathbf{d}_{RB} \\ & \mathbf{I}_3 \end{bmatrix} \begin{bmatrix} {}^{RB}\mathbf{R}_{xy} & {}^{RB}\mathbf{R}_{xy} \end{bmatrix} \begin{pmatrix} {}^B\mathbf{v} \\ {}^B\boldsymbol{\omega} \end{pmatrix} + \mathbf{e}_k \quad (5.22)$$

where the terms used are the same quantities defined in equation (5.20). In fact, this is a reasonable assumption in most cases (e.g. the navigation terrain is locally flat) and violation to this constraint are taken into account by an additive noise term $\mathbf{e}_k \in \mathbb{R}^3$. Another additional information that can be exploited for ameliorating algorithms performance is the classical zero velocity update (ZUPT), which is a well known technique for improving accuracy of inertial navigation systems (e.g. it is commonly used in pedestrian navigation algorithms). Basically, the following constraint is conditionally applied:

$$\begin{pmatrix} \mathbf{v} \\ \boldsymbol{\omega} \end{pmatrix} = \begin{bmatrix} \mathbf{0}_3 \\ \mathbf{0}_3 \end{bmatrix} + \mathbf{e}_{ZUPT} \quad (5.23)$$

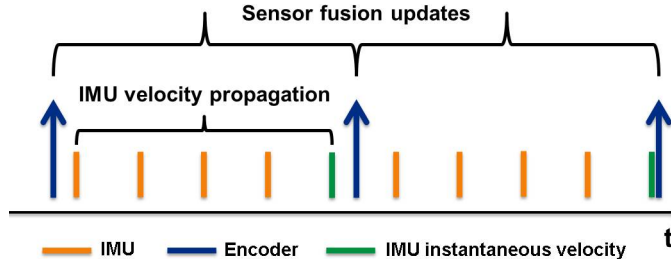


Figure 5.5: The figure represents the typical configuration in time of the measurement samples: update rates are 100 Hz for the IMU and about 20 Hz for the wheel encoders. For each update of the sensor fusion algorithm, the additional data from the IMU must be treated differently depending on whether they are used to propagate inertial quantities, i.e. relation (5.4) and (5.5), or to generate instantaneous velocities for comparison with the encoder readings, i.e. relation (5.20).

in order to reset the integration drift when a stationary configuration is detected. The detection strategy considered in the following was based on thresholding the ℓ^2 -norm of the encoders reading.

Data pre-processing

The datasets collected from the sensory systems considered are not synchronized (see Figure 5.5) and generally not even sampled at a constant rate. The latter case is true for the encoder data which are collected via the 8 bit embedded microcontroller (i.e. Arduino UNO) and false for the commercial IMU and stereophotogrammetric system. In order to meaningfully fuse the information coming from the sensors, collected datasets were pre-processed to correct for time misalignments. First, encoder measurements were resampled at a constant rate via polynomial interpolation. Then, three synchronization problems were considered in the given sequence: individual encoders' clocks alignment, encoders with the IMU's time alignment, encoders and with the optical reference system's time alignment.

The first problem arises from the fact that, on the one hand, encoders are polled sequentially by the microcontroller as they share the same communication bus, but on the other hand, a single timestamp is used for the set of readings. Therefore, it is not unlikely that wheel velocity readings belonging to

CHAPTER 5. SINGLE DEVICE FOR NAVIGATING AN OMNIDIRECTIONAL WHEELED ROBOT

90

the same timestamp correspond, in fact, to different time instants. Since the control signals used in the experiments are synchronously send to the wheels and follow the same pattern in time (a part from the sign), it is possible to synchronize encoders pairwise using correlation computed on the absolute value of the wheel angular speed. For this synchronization problem, mismatch among clocks was modelled as a constant offset.

The remaining synchronization problems, i.e. encoders with the IMU and the optical reference, are solved with the following procedure. A linear model is assumed relating each pair of different clocks, i.e. an offset and a clock skew term. This model is fitted on a number of clock correspondence pairs generated using correlation on the ℓ^2 -norms of the angular velocity of the robot, that is directly measured by the IMU and the optical reference and inferred from the wheel speed using nominal values for the parameters of the robot's kinematic model. In addition, to achieve a robust fitting against outliers the RANSAC algorithm [Hartley and Zisserman, 2000] was used to estimate clock model's parameters.

5.3 Sensor fusion

In this section a number of sensor fusion problems are presented that pertain calibration and navigation relying on a combination of measurements from the encoders, the optical reference and the IMU. The problems will be formulated as part of the general estimation framework introduced in Chapter 3. Calibration problems will be formulated either as a maximum likelihood (ML) or maximum a posteriori (MAP) estimation. The **pdf** considered in this work will be those associated to the noise terms introduced in the models of section 5.2, i.e. $\mathbf{e}_v, \mathbf{e}_q, \mathbf{e}_b, \mathbf{e}_a, \mathbf{e}_e, \mathbf{e}_\phi, \mathbf{e}_{ZUP T}$. It will generally take the form of a Gaussian multivariate distribution:

$$p(\mathbf{e}|\boldsymbol{\theta}) = \frac{1}{\sqrt{(2\pi)^n |\boldsymbol{\Sigma}|}} \exp \left(-\frac{1}{2} \mathbf{e}(\boldsymbol{\theta})^T \boldsymbol{\Sigma}^{-1} \mathbf{e}(\boldsymbol{\theta}) \right) \quad (5.24)$$

where the error $\mathbf{e} \in \mathbb{R}^n$ has a zero mean and covariance matrix $\boldsymbol{\Sigma} \in \mathbb{R}^{n \times n}$ and is conditionally dependent on a set of parameters $\boldsymbol{\theta} \in \Theta$ that characterize the model equation. As discussed in section 3.2, given the parametric statistical distribution describing \mathbf{e} , the maximization of (3.5) can be reformulated as the following minimization problem:

$$\hat{\boldsymbol{\theta}}_{ML} = \arg \max_{\boldsymbol{\theta}} p(\mathbf{e}|\boldsymbol{\theta}) = \arg \min_{\boldsymbol{\theta}} -\log p(\mathbf{e}|\boldsymbol{\theta}) = \arg \min_{\boldsymbol{\theta}} \|\mathbf{e}\|_{\boldsymbol{\Sigma}} \quad (5.25)$$

5.3. SENSOR FUSION

91

where the convexity of the negative logarithm function has been exploited and the last equality is obtained by ignoring constant terms (as they have no effect on the solution) under the assumption of a Gaussian distribution for \mathbf{e} . The symbol $\|\cdot\|_{\Sigma}$ was used to denote the quadratic norm operator defined in (3.13). A similar result also applies to the case of MAP estimation.

The navigation problem will be formulated using the state space representation detailed in chapter 3, i.e.:

$$\begin{cases} \mathbf{x}_{k+1} = f(\mathbf{x}_k, \mathbf{u}_k) + \mathbf{v}_k \\ \mathbf{y}_k = g(\mathbf{x}_k, \mathbf{u}_k) + \mathbf{w}_k \end{cases} \quad (5.26)$$

where $\mathbf{x}_k \in \mathbb{R}^n$ represents the state of the system at time k , \mathbf{u}_k is a vector of m inputs, and \mathbf{y}_k is the vector of r system responses. The system is modelled as nonlinear and stochastic, with the additive zero-mean noise terms $\mathbf{v}_k \in \mathbb{R}^n$ and $\mathbf{w}_k \in \mathbb{R}^r$, whose values for the standard deviations will be derived according to what empirically observed in the measurements and reported in table 5.1. The state estimation will be formulated either as a filtering problem, i.e. the current state given all available measurement is the object of interest, or as a smoothing problem, i.e. the trajectory of the state given all the measurement is the object of interest. Respectively, it will be solved by maximizing the posterior density $p(\mathbf{x}_k | \mathbf{y}_{1:k})$ or $p(\mathbf{x}_{1:N} | \mathbf{y}_{1:N})$ in a MAP estimation framework. In order to achieve robustness against unmodelled error sources (e.g. wheel

Table 5.1: Standard deviation of the available measurements.

	Vicon linear velocity (v)	Vicon angular velocity (ω)	IMU velocity increment (Δv)	IMU angular velocity (ω)	Encoders wheel velocity (ϕ)
Standard deviation	~ 1 mm/s	~ 1.5 °/s	~ 0.19 mm/s	~ 0.25 °/s	$< 10^{-22}$ °/s *

* virtually limited by the encoder's resolution.

slippage), the Gaussian multivariate distribution will be in some cases replaced by a Student-t multivariate distribution 3.14.

Calibration with optical reference measurements

In order to obtain an initial estimate for the kinematic calibration matrix (K), a first sensor fusion algorithm was designed for combining encoder readings with information from the optical reference system according to the scheme

92 CHAPTER 5. SINGLE DEVICE FOR NAVIGATING AN
OMNIDIRECTIONAL WHEELED ROBOT

reported in 5.6. The fusion algorithm was formulated as an optimization problem, where the vector of parameters $\theta \in \mathbb{R}^{18}$ considered was the following:

$$\theta = \begin{pmatrix} \dot{\phi}_{1[i=1:N]} \\ \dot{\phi}_{2[i=1:N]} \\ \dot{\phi}_{3[i=1:N]} \\ \dot{\phi}_{4[i=1:N]} \\ \mathbf{vec}(K) \\ {}^{RC}\psi_x \\ {}^{RC}\phi_y \end{pmatrix} \quad (5.27)$$

which comprises all wheels' angular speed measurement $\dot{\phi}_i$ from the beginning to the end of the recordings, the calibration matrix entries defined in (5.21) extracted via the matrix vectorization operator ($\mathbf{vec}(\cdot)$) and the reference frame misalignments ${}^{RC}\mathbf{R}_{xy}$, which in this case relates the cluster frame (C) to the robot frame (R), that is expressed as the individual angular component along the x and y axis, respectively ${}^{RC}\psi_x$ and ${}^{RC}\phi_y$. Referring to the scheme in (5.6), encoders readings are considered noisy and are modelled according to (5.8) while optical measurements are taken as the reference and both are combined according to the constraints introduced by relation (5.22) and (5.21). The following ML formulation results for this calibration problem:

$$\hat{\theta}_{ML} = \arg \min_{\theta} \sum_{i=1}^N \|\mathbf{e}_{e_i}\|_{\Sigma_e}^2 + \|\mathbf{e}_{k_i}\|_{\Sigma_k}^2 + \|\mathbf{e}_{\phi_i}\|_{\Sigma_\phi}^2 \quad (5.28)$$

where the cost functions introduced ($\mathbf{e}_e, \mathbf{e}_k, \mathbf{e}_\phi$) are derived from the relations (5.8), (5.22) and (5.21) and are assumed to be Gaussian. Despite a Student-t distribution would be a better representation of the errors on the encoders' measurements (\mathbf{e}_e) that can be affected by outliers, it will be shown in section 5.5 that the choice of a Gaussian or a Student-t has no effect on the calibration problem's solution.

Calibration with inertial measurements

The calibration of the robotic platform kinematics using IMU and encoders readings was devised as a two stage process: the first stage is obtaining an estimate for the quantities $({}^B\mathbf{v}, {}^B\boldsymbol{\omega})$ from the IMU measurements and the second one is to use the estimated quantities in a sensor fusion scheme similar to that of Figure 5.6, previously discussed. The first part of the procedure was

5.3. SENSOR FUSION

93

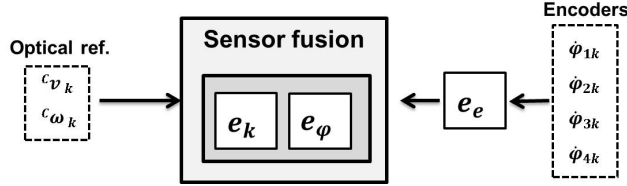


Figure 5.6: The figure reports the sensor fusion scheme used for the problem of calibrating robot kinematics using optical and encoder measurements.

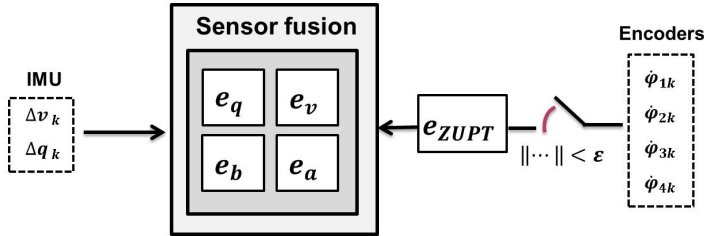


Figure 5.7: The figure reports the sensor fusion scheme, respectively implemented as a filter and a smoother, for estimating the quantities $({}^B \mathbf{v}, {}^B \boldsymbol{\omega})$.

formulated as a filtering and smoothing problem and schematically represented in Figure 5.7. The filtering problem considered the following system state vector:

$$\mathbf{x} = \begin{pmatrix} {}^L \mathbf{v} \\ {}^{LB} \mathbf{q} \\ \boldsymbol{\omega}_b \end{pmatrix} \quad (5.29)$$

where the first two elements can be combined to get the value of ${}^B \mathbf{v}_k$ (see relation (5.14)) and the third element is the gyroscope bias, used to correct angular velocity measurements. The filter architecture used the quantities measured by the IMU to propagate the state estimate forward in time, through the relations formulated in (5.4), (5.5) and (5.6). The state estimate is then corrected using a zero velocity update strategy implemented as in (5.23). The correction is only applied when the system is considered static and the detection strategy is based on a threshold (ε) on the value of the ℓ^2 -norm of wheel speeds. The assumption that the robot is idle when the wheel encoders readings are close to 0 is verified experimentally to be reasonable. The output from the filtering algorithm is used as initial value for the estimate ($\hat{\mathbf{x}}_0$) in a

smoothing problem, which considers the following state vector:

$$\mathbf{x} = \begin{pmatrix} {}^L\mathbf{v}_1 \\ \vdots \\ {}^L\mathbf{v}_N \\ {}^{LB}\mathbf{q}_1 \\ \vdots \\ {}^{LB}\mathbf{q}_N \\ \boldsymbol{\omega}_{b,1} \\ \vdots \\ \boldsymbol{\omega}_{b,N} \\ \mathbf{a}_b \end{pmatrix} \quad (5.30)$$

where the bias term (\mathbf{a}_b) is now included in the problem. The smoothing algorithm determines a state estimate by solving the following MAP optimization:

$$\hat{\mathbf{x}}_{MAP} = \arg \min_{\mathbf{x}} \|\mathbf{e}_a\|_{\Sigma_a}^2 + \sum_{i=1}^N \left(\|\mathbf{e}_{v_i}\|_{\Sigma_k}^2 + \|\mathbf{e}_{q_i}\|_{\Sigma_q}^2 + \|\mathbf{e}_{b_i}\|_{\Sigma_b}^2 \right) + \sum_{j=1}^L \|\mathbf{e}_{ZUPT_j}\|_{\Sigma_{ZUPT}}^2 \quad (5.31)$$

where the ZUPT are applied a number $L < N$ of times. After the smoothing, an estimate for $({}^B\mathbf{v}, {}^B\boldsymbol{\omega})$ is available and the same calibration procedure used with the optical measurements can be applied to obtain a value for the calibration matrix (\hat{K}), which in this case is related to the IMU body frame (B).

Navigation

The navigation of the omnidirectional robotic platform from sensor fusion of IMU and wheel encoders' measurements (which is graphically displayed in Figure 5.8) was implemented as a smoothing problem. The following state vector

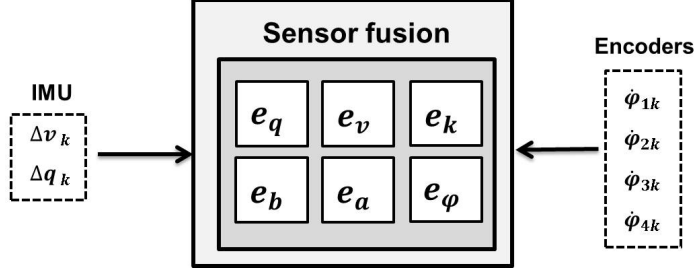


Figure 5.8: The figure shows the sensor fusion scheme used for navigation using inertial measurements.

was considered in the formulation:

$$\mathbf{x} = \begin{pmatrix} {}^L\mathbf{v}_1 \\ \vdots \\ {}^L\mathbf{v}_1 \\ {}^{LB}\mathbf{q}_1 \\ \vdots \\ {}^{LB}\mathbf{q}_N \\ \boldsymbol{\omega}_{b,1} \\ \vdots \\ \boldsymbol{\omega}_{b,N} \\ \mathbf{a}_b \end{pmatrix} \quad (5.32)$$

which is the same used for the smoother in the calibration algorithm described above. Differently, in the navigation case a value for the robot calibration matrix is available (K) and measurement from the encoders can be used in the state correction step of the algorithm through the relation expressed in (5.20). Instead, state propagation is based on the information from the IMU that is used as input to the relations (5.4) and (5.5). Since measurements have different update rates, care must be taken when combining information from different sources in the sensor fusion scheme. Particularly, robot linear and angular velocities computed from the encoders are instantaneous quantities. Therefore, instantaneous quantities must be derived from the IMU in order to evaluate the error term \mathbf{e}_ϕ of relation (5.20), i.e. only the last received IMU sample must be considered in the computation, as represented in Fig-

96 CHAPTER 5. SINGLE DEVICE FOR NAVIGATING AN
OMNIDIRECTIONAL WHEELED ROBOT

ure 5.5. Furthermore, in order to make the navigation scheme robust the term \mathbf{e}_ϕ was assigned a Student- t distribution. Therefore, the smoothing problem was solved as the following MAP optimization:

$$\begin{aligned} \hat{\mathbf{x}}_{MAP} = \arg \min_{\mathbf{x}} & \|\mathbf{e}_a\|_{\Sigma_a} + \\ & \sum_{i=1}^N \left(\|\mathbf{e}_{v_i}\|_{\Sigma_k} + \|\mathbf{e}_{q_i}\|_{\Sigma_q} + \|\mathbf{e}_{b_i}\|_{\Sigma_b} \right) + \\ & \sum_{j=1}^M \frac{\nu + n}{2} \log \left(1 + \frac{1}{\nu} \|\mathbf{e}_{\phi_j}\|_{\Sigma_\phi} \right) \end{aligned} \quad (5.33)$$

where the last cost function (\mathbf{e}_{ϕ_j}) is evaluated for a number $M < N$ of samples, due to the slower sampling rate of the encoders. Note that the navigation was here formulated as a smoothing problem. Nonetheless, for real-time operation the presented approach can be implemented as a filtering problem by introducing a marginalization step after each state propagation. Also, position was not included in the state as there was no mean to correct for integration drifts with the presented setup (dead reckoning navigation). A prone to drift estimate can be recovered via Runge-Kutta integration of the computed quantities (${}^B\mathbf{v}, {}^B\boldsymbol{\omega}$), properly rotated in the navigation frame.

5.4 Results

The omnidirectional robotic platform was remotely driven according to the sequence of movement shown in Figure 5.9. This sequence is composed by a forward/backward motion, a counter and clockwise rotation of 225° and a right/left motion and it was devised with the aim of spanning the space of all the possible direction of motion. Each movement was executed for 3 s with a 1s break time at the end and the overall duration of the experimental trial was 400 s. The experimentation was carried in a room equipped with an optical motion capture system. The IR reflective markers of the system were fixed on the robot and data from the wheel encoders, the IMU and the optical system were simultaneously collected. After pre-processing operations, datasets were elaborated according to the algorithms described in section 5.3. The first results presented pertain the computation of the initial value for the calibration matrix (K) using the optical and encoder sensor fusion scheme of Figure 5.6. In Figure 5.10 the estimated differential direct kinematic relation for the robotic platform (i.e. the relation from wheel speeds to robot velocities

5.4. RESULTS

97

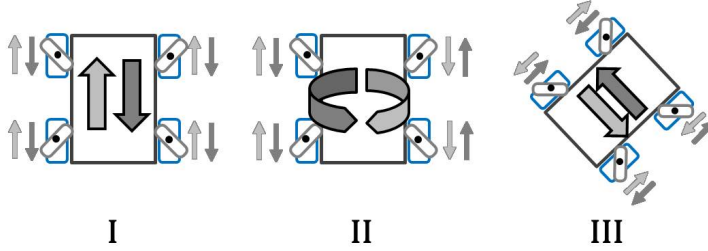


Figure 5.9: The figure represents the sequence of robot motions that is used for the experimental trial. The movements indicated with the light grey arrows are executed first in the increasing order (I,II and III), followed by those represented with dark grey arrows that are performed in decreasing order (III, II and I).

encoded by the inverse of calibration matrix K) is shown. In order to assess the repeatability of the estimate, a number of 50 different datasets were used for the computation, obtained by randomly selecting windows of 60s from the experimental trial data. Furthermore, a different initial value was used each time.

In Figure 5.11 the effect of having the K matrix calibrated on the accuracy of the odometry computed from the wheels' encoders is reported. In absence of unpredicted perturbation, e.g. terrain bumps or wheel slippage, the calibrated odometry is already an accurate estimate of the robot state variables. Instead, when slippage occurs encoders readings can generate a significantly misleading information to the aim of dead reckoning navigation. This event is shown in Figure 5.12 between times 180 s and 190 s, where the readings from the encoders are compared to the predicted values from the sensor fusion algorithm and those obtained from optical reference data (using the relation in (5.20)). Note that the reason why reference encoder data from the optical system have different level of noise on the 4 wheels is in the different distance of wheels reference frames from the cluster frame. The more the distance, the bigger the lever arm and the contribution of the noisy angular velocities measured by the optical system (see Table 5.1. Encoder measurements are predicted via the sensor fusion scheme in Figure 5.6 in which the error term e_e was in this case modelled with a Student-t distribution. Therefore, when the slippage occurs a significant difference between the predicted measurement (from the optical reference) and the correction (from encoders) is observed. Basing on that,

CHAPTER 5. SINGLE DEVICE FOR NAVIGATING AN
OMNIDIRECTIONAL WHEELED ROBOT

98

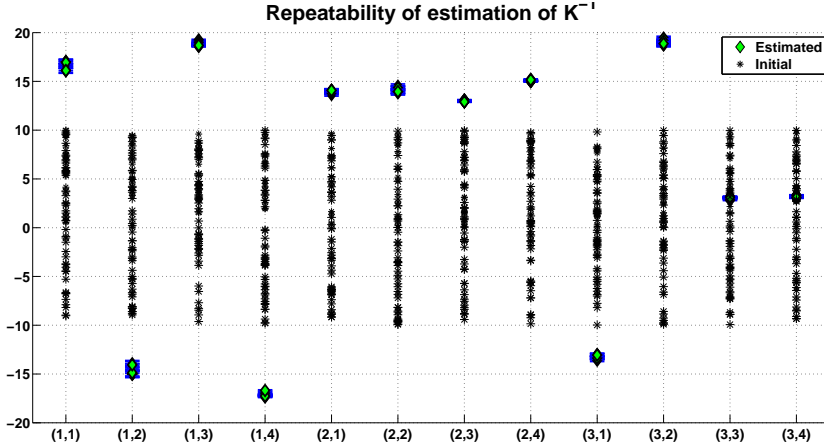


Figure 5.10: The figure reports the value (green markers) of the direct differential kinematic matrix of the robot (K^{-1}) computed via sensor fusion of optical and encoders' data. The estimation procedure was repeated for 50 different datasets that were associated to different initialization values (black asterisks).

the sensor fusion algorithm is capable of detecting the events and to reject the wrong correction. Data from the IMU and the encoders were fused in agreement with the scheme described in paragraph 5.3 in order to estimate the calibration parameters of K . Outcome of the procedure is reported in Figure 5.13, where the values obtained from the fusion with IMU data are compared to those previously obtained with the optical reference. Both datasets show a good agreement as it was expected, given the fact that the body (B) and the cluster (C) reference frame are positioned in close proximity to each other. Nominal value for the calibration matrix are also reported, that were computed from the relation in (5.18), using hand measured values for the required quantities. Finally, in Figure 5.14 the results of the sensor fusion scheme for navigation proposed in paragraph 5.3 are reported. In nominal navigation conditions (i.e. even floor and no wheel slippage) the calibrated odometry is accurate and closely match the measurements from the reference optical system. Therefore, calibrated odometry was used in the sensor fusion in order to limit the drift that would eventually occur if navigation was solely based on the integration of data from the IMU (e.g. to get velocity from specific force measurements). Instead,

5.5. DISCUSSION

99

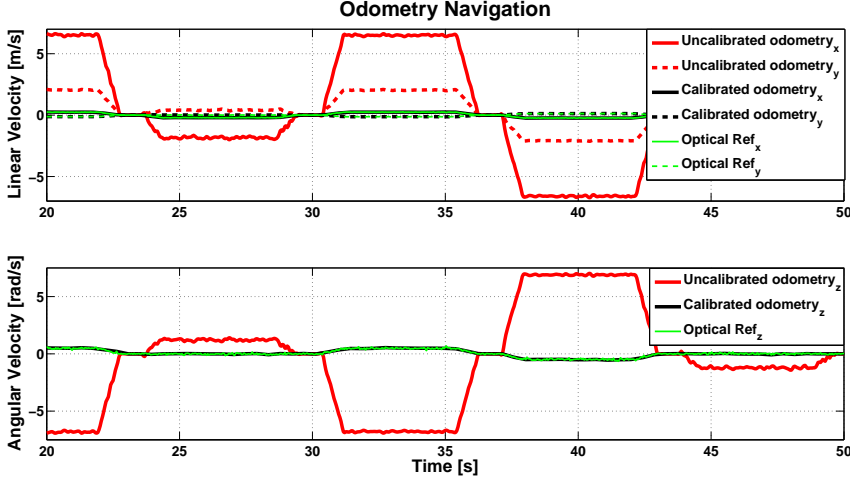


Figure 5.11: The figure reports a comparison of the linear and angular velocity w.r.t. the cluster frame (C) as predicted with the uncalibrated encoder based odometry (red line), with the calibrated odometry (black line) and as measured by the optical reference (green line).

when slippage occurs, the usual detection and rejection strategy is applied and calibrated odometry corrections are rejected. For the whole (expectedly short) duration of the slippage, the sensor fusion algorithm behaves in fact as an inertial navigation system.

5.5 Discussion

In this chapter a novel approach to autonomous navigation and calibration of an omnidirectional robotic platform, designed to be flexible and robust, is presented. The method requires only the presence of an IMU as additional onboard sensor and proposes a fusion of inertial information with the readings from wheel encoders. The presented algorithms allows for calibrating systematic sources of error (robot kinematics) in view of obtaining accurate odometry information. In addition, inertial based navigation is used to correct for wheel slippage, which is the main source of non systematic errors affecting dead reckoning navigation of ground robotic platforms. Though errors in position were

CHAPTER 5. SINGLE DEVICE FOR NAVIGATING AN OMNIDIRECTIONAL WHEELED ROBOT

100

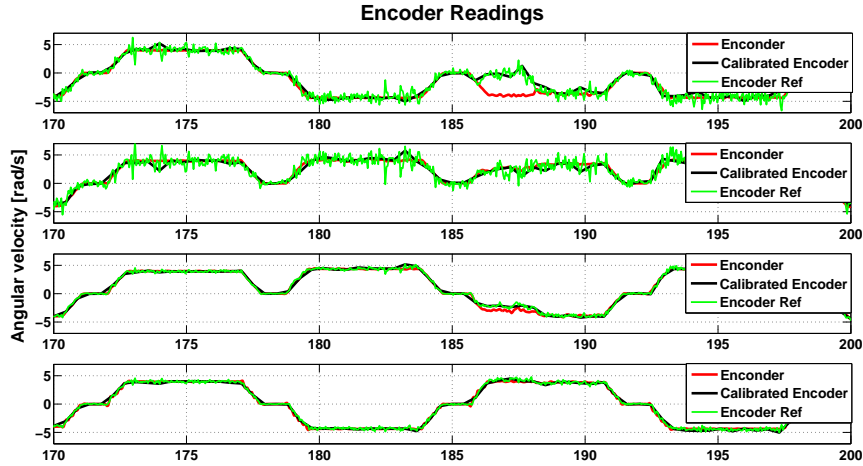


Figure 5.12: The figure reports a comparison of the wheel encoders' data as measured by the sensors (red line), predicted by the estimation algorithm (black line) and predicted using optical reference data (green line). Note that between time 185 s and 190 s a slippage event occurs (1st row) leading to significant deviation of the measurements from the predicted values.

not reported, a significant difference in navigation accuracy between odometry based and the presented method is expected in the long run, basing on the intuition that wheel slippage introduces an offset in the estimated heading that cannot be recovered. This is the first time in the literature that an inertial sensor is used in combination with encoders for autonomous calibration and navigation of an omnidirectional wheeled platform.

In the presented material, a number of relations were derived linking the measurements from the two different sensors type and the a priori knowledge on the kinematical characteristics of the robot. Those relations were used to constrain different optimization problems aiming at calibrating the encoder based odometry and at making the navigation robust against unmodelled events. The latter result was achieved by using the Student-t distribution to model error terms of the relation in which such spurious events can occur (i.e. the wheel encoder measurement model in (5.8) and the encoder to inertial relation (5.20)). The t-distribution is a natural choice of model for such data and it provides

5.5. DISCUSSION

101

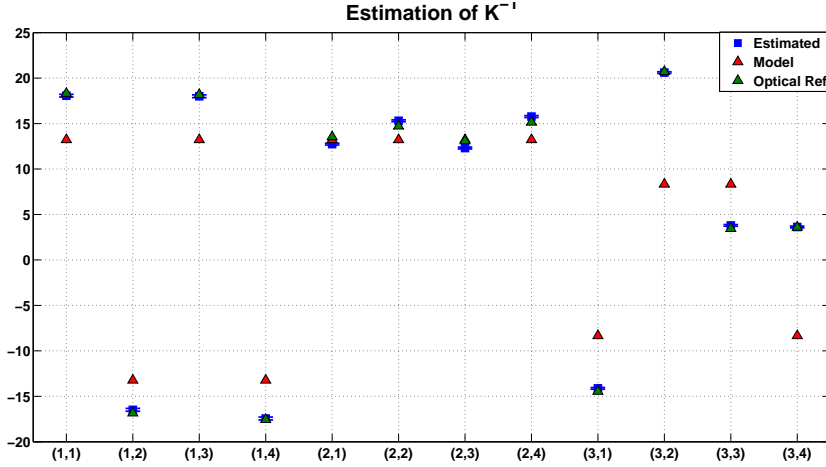


Figure 5.13: The figure reports the value (blue markers) of the direct differential kinematic matrix of the robot (K^{-1}) estimated via sensor fusion of IMU and encoders' data and compared to the value from the optical sensor fusion (green markers) and to the nominal (red markers), obtained by using measured robot dimension in the model described in (5.18).

a parametric approach to robust statistics. In the proposed navigation algorithm, the Student-t implements an implicit outlier detection and rejection scheme that was proved to be effective for the proposed task. Instead, for the calibration problem the choice of a t-distribution over a Gaussian had no effect on the solution of the problem. This result is motivated by the particular experimental conditions that are verified in practice and that brings to the fusion of noisy Gaussian distributed data (poor information content) with highly informative but outlier prone Student-t distributed data. Basically, in that case the fusion algorithm is provided with a multimodal distribution, that results in a multiple minima optimization problem. As a consequence, the algorithm will arbitrary pick either of the two sources of information. However, the estimation of the calibration parameters does not depend on which minima is chosen and the Student-t distributed error could have equivalently been modelled as a Gaussian distribution. This multiple minima situation is graphically displayed in Figure 5.15. Another aspect related to calibration that deserve further in-

CHAPTER 5. SINGLE DEVICE FOR NAVIGATING AN OMNIDIRECTIONAL WHEELED ROBOT

102

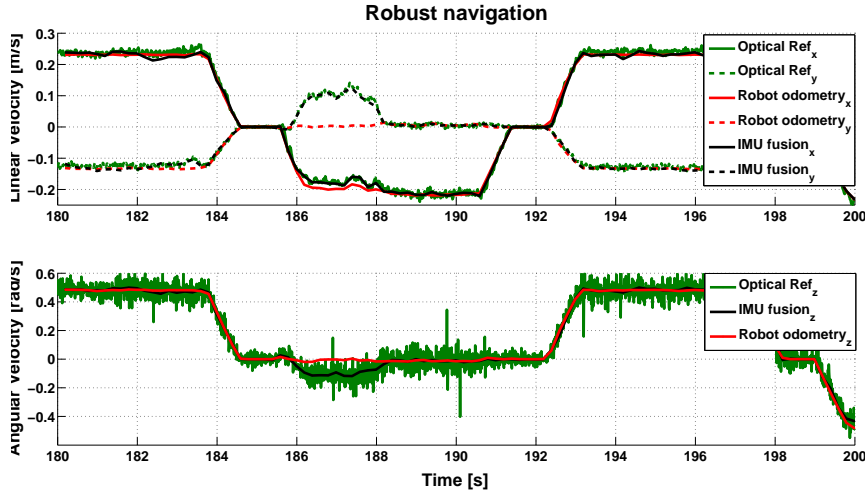


Figure 5.14: The figure reports an example of robust navigation (against wheel slippage) achieved through combination of IMU and encoders data with the proposed sensor fusion algorithm.

vestigation is that of observability of the calibration matrix in dependence to the type of robot motions. Despite in the proposed experimental trial the selected sequence of movements (that spanned all the space of possible direction of motion that can be generated by the robot) proved effective for the task of calibration, mathematical conditions that guarantee observability should be investigated as part of future research endeavour. In addition, the processed experimental trial was performed on a reasonably even terrain and it is leaved as object to the future research exploring adaptations of the method to the case of bumpy terrains or outdoor settings.

Concluding, the general framework introduced in the previous chapter 3 is here adapted to a specific application in the field of robotics. Nevertheless, the flexibility of the method makes it well adaptable to other classes of problems where a inertial sensor measurements can be combined with other sensors' types or different models. For instance, the good dead-reckoning navigation performance that can be achieved with a single IMU in the short term makes the presented fusion suitable for the general class of the kidnapped robot problems. Furthermore, all the camera or depth camera based simultaneous localization

5.5. DISCUSSION

103

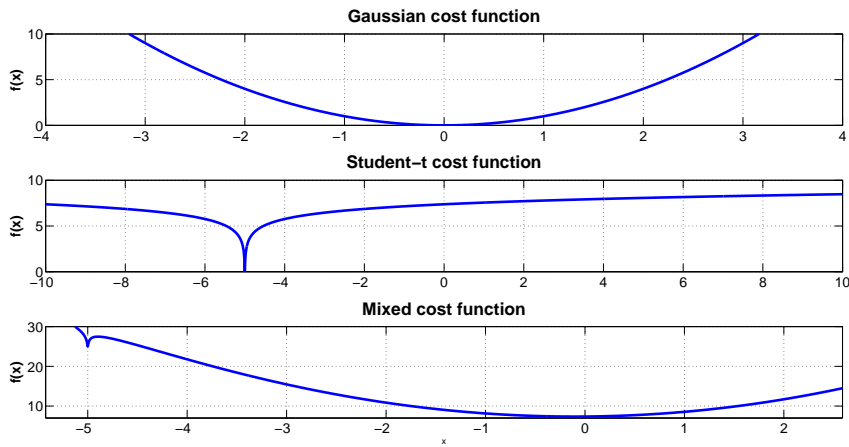


Figure 5.15: An example of multiple optimization minima originating from the combination (3rd row) of a poorly informative Gaussian cost function (1st row) and a highly informative Student-t cost function (2nd row).

and mapping (SLAM) algorithms have to cope with a highly likelihood of the presence of outliers in the measurements (e.g. generated by variation in the environment light conditions or scattering and reflections). For this class of problems the combined use of an IMU and the fusion scheme presented could provide significant improvements in performance.

Tesi di dottorato in Ingegneria biomedica, di Luca Ricci,
discussa presso l'Università Campus Bio-Medico di Roma in data 11/06/2015.
La disseminazione e la riproduzione di questo documento sono consentite per scopi di didattica e ricerca,
a condizione che ne venga citata la fonte.

Chapter 6

Multiple devices for upper body motion capture in children

This chapter deals with inertial motion capture with children and presents a methodology that can be used to solve the problem of calibrating inertial sensor and bio-mechanical model reference frames. The calibration step is a preliminary and key operation in order to achieve human motion reconstruction from inertial measurement units, as it allows converting measurements from the sensors into useful human kinematics information. First, a protocol of functional movements, studied to be suitable for an use with children (tested on 6–7 years old subjects), is described. Then, a strategy to extract functional axes together with a reliability metric is detailed. Eventually, calibration is achieved through a proper cost function fed to a non linear optimization algorithm. Calibrated data and a human kinematic model can be used in combination to reconstruct human motion.

6.1 Inertial motion capture of children in daily-life scenarios

The possibility to capture and quantitatively measure children's motion repertoire in a daily life scenario is of great interest for a number of reasons. Clinical evaluation tools to measure motor skills in children are to date able to offer qualitative rather than quantitative evaluation (i.e. studies using standardized measures have difficulties in providing fine-grained details on children movements characteristics). Examples of widely spread test to measure motor skills

CHAPTER 6. MULTIPLE DEVICES FOR UPPER BODY MOTION
CAPTURE IN CHILDREN

106

in children are the Gross Motor Function Measure, the Movement ABC or the 10 Meter Walk Test [Henderson and Sugden, 1992, Russell et al., 2000, Crock et al., 2001]). Therefore, the lack of reliable, objective measurements foster the interest in the development of tools to accurately capture information on children's motion skills in real life environments. For instance, it would be of key importance in the rehabilitation of children with a chronic health condition, such as cerebral palsy, to guide and evaluate interventions, to monitor progress and also to provide families with an objective feedback [Gilmore et al., 2010]. Besides, quantitative motion evaluation can support standard clinical rating scales, providing clinicians with enriched information on patients' health [Zhang et al., 2012]. Furthermore, research studies on the role of motor and communicative gesture (e.g. gestures) have highlighted the importance of assessing motor characteristics of children's behaviour [Pettenati et al., 2009, von Hofsten, 2004]. Also, in children with autistic spectrum disorder (ASD) or "at high-risk" for ASD, appropriate motion evaluation tools may be of relevance for early diagnosis and intervention [von Hofsten and Rosander, 2012, Taffoni et al., 2009, Campolo et al., 2012].

A considerable number of systems for human motion capturing is commercially available at present. Despite the technologies and the approaches are many, exhibiting different performance characteristics and operating on entirely different physical principles, no 'silver bullet' currently exists [Welch and Foxlin, 2002]. Among the plethora of choices, wearable technologies have the potential to meet the requirements for this specific application, as reported in [Bonato, 2003, Bonato, 2005]. Particularly, IMU based wearable motion tracking systems provide inertial measurements (i.e. acceleration, angular velocity and magnetic flux density) aside an accurate 3D-orientation estimate, thanks to sensor fusion algorithms (for a comprehensive review on this topic see [Sabatini, 2011]), and are the selected choice for this study.

In order to obtain a precise tracking of the kinematics of human joints, the fulfilment of a calibration protocol is strictly required. The aim of this research work was to define such a calibration procedure to capture the kinematics of upper limbs and thorax in children. The presented method allows the construction of meaningful functional frames (**FF**), in the sense of being representative of real physiological motions, on the human body and the estimation of the calibration matrix relating each IMU's sensor frame (**SF**) to the associated FF of the individual body segment. A typical calibration protocol is composed by the following steps: (1) a series of fixed reference postures and/or functional movements that the subject under experimentation is asked to perform, (2) the definition of both an FF on each body segment of interest and a

mapping between each axis of the FF and each reference postures/functional movements, (3) the computation of the transformation matrix between each FF and its corresponding SF. Despite existing literature proposes procedures for kinematic tracking of both upper and lower limbs [Luinge et al., 2007, Cutti et al., 2008, Cutti et al., 2010, de Vries et al., 2010, Kontaxis et al., 2009], no study to date has provided a calibration protocol specifically designed to be used with children. In fact, existing procedures does not take into consideration the constraints related to an use of wearable inertial technology with children, e.g. the fact that a particular care in the choice of movements to perform is required. Therefore an ad-hoc design is required. Based on the outcomes from a previous study [Ricci et al., 2013], we have built a calibration protocol which defines an ameliorated set of reference postures/functional movements, a new way to estimate reference axes from sensors' data and introduces a novel methodology to compute the transformation matrix. The experimental procedure has been validated in simulation and tested in typical development (TD) children. Further, it has been administered by non-technicians in a daily life scenarios (e.g. at school or at home) as its application does not require any particular expertise.

The following sections are organized as follows: section 6.2 provides an introduction of the motion tracking system architecture, including hardware and software components that have been employed and developed, and offers a detailed description of the proposed calibration protocol alongside data analysis methodology; section 6.3 reports the results from simulations and experimental sessions, plus an example on how to reconstruct motion after the proposed procedure. Eventually, section 6.4 discusses the results and presents the study conclusions.

6.2 Materials and Methods

System Architecture

The experimental setup is comprised of a set of IMUs and a custom developed software for data acquisition. On the hardware side, 5 wireless sensing units (SU) are used, chosen among the number of commercially available systems. In Particular, we selected the Opal by APDM Inc. in reason of their smaller dimension and lower weight (22 g) that makes them particularly suitable for the target application on children. Each SU contains an IMU, a micro SD for robust data logging and a wireless radio transceiver. The orientation information is computed via an embedded Kalman filter, in the form of a quaternion (more

CHAPTER 6. MULTIPLE DEVICES FOR UPPER BODY MOTION CAPTURE IN CHILDREN

details on quaternion are reported in Appendix A) relating the orientation of a local, gravity and geomagnetic established frame (L) to the sensor frame (S), i.e. ${}^L S \mathbf{q}$. An access point is provided to gather synchronized sensor data and make them available to a PC in real-time.

On the software side, a C++ GUI application for agile system managing and data collection was developed using the Qt cross-platform framework. Stream of synchronized data can be collected at the maximum rate of 128 Hz. Within the software functionalities, each IMU device can be tagged with the identifier of the human limb to which it is attached in order to store this information in the logs. The software also implemented tools for real-time data plotting and 3D motion visualization in a virtual reality (VR) environment; the VR environment embeds a simple kinematic model of a 3D character, which is rendered using the OGRE graphic engine [OGRE,]. An overview of the described experimental setup is shown in Figure6.1.

Calibration protocol

This section describes the calibration protocol for the kinematic tracking of thorax and upper limbs motion in children. Beforehand providing details and in order to clear out what will follow, the entire procedure is briefly reported.

The proposed methodology was tested on a group of 40 primary school children (average age is 6.9 ± 0.65 years old, the minimum is 6.0 and the maximum is 8.0 and the group is composed by 22 females and 18 males). Informed consent was obtained from all children's parents, as required by the Institutional Review Board at the italian National Research Council (CNR). The experimentation session took place at the school, thus capturing motion in an environment familiar to the children.

Before starting the experimentation session, IMU accelerometers calibration was assessed following the procedure described in [Campolo et al., 2006]. Also, all IMUs were kept idle on a plank for a period of 20 seconds, in order to estimate and remove gyroscope constant bias. After that, each sensor was fixed to the corresponding body segment of interest using Velcro straps. During the procedure, the mapping sensor-body segment was stored in the data logs through the developed software interface.

The calibration protocol requires the 5 SUs to be attached to the following spots on the body: centrally on the thorax (sternum), latero-distally on the right and left upper arm, and near the wrist on the right and left forearm, as shown in Figure6.2. On each body spot an arbitrarily defined and body fixed FF was set. The FF is a right handed system of coordinated made of

6.2. MATERIALS AND METHODS

109

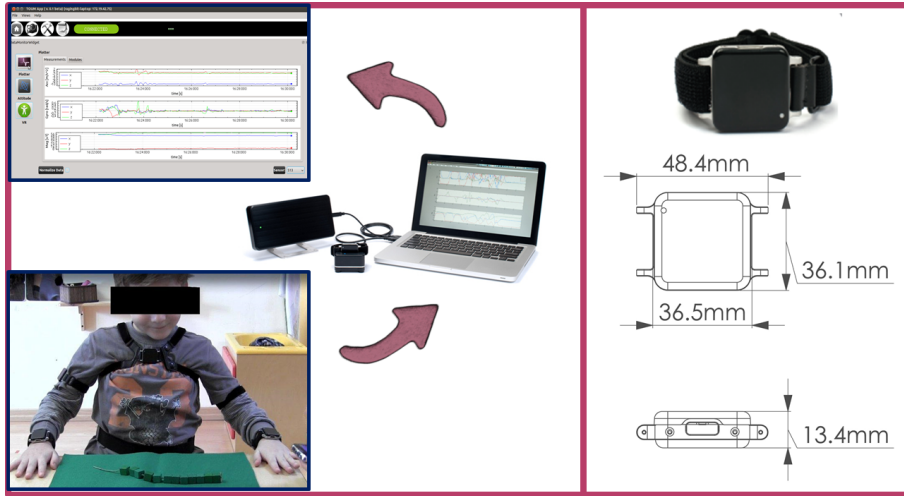


Figure 6.1: The experimental setup comprises 5 SUs that are attached to the upper body at predefined spots (thorax, distally on the upper arm and forearm) and a PC for data collection. Synchronized data from the SU are wireless received on the PC and processed via custom developed software (GUI is visible on the top left). Each sensing unit is a wristwatch sized box fixed on the body segments via Velcro straps (on the right).

orthogonal axes that are descriptive either of the degrees of freedom associated to the body limb, e.g. the axis of rotation for a flexion–extension movement, or of the anatomical structure of the segment itself, e.g. the longitudinal axis. Finally, each SU is matched with a corresponding FF. The actual calibration procedure articulates in a series of 4 successive steps:

- step 1** The participant, while wearing the SUs, completes a predefined list of movements and adopts a set of stances, separately comprising the thorax, the upper limbs or the forearms. Each movement in the list is associated with and aims to estimate an axis of the defined FFs;
- step 2** The information is collected from the SUs and pre-processed in order to remove bias from the gyroscopes and extract the direction of both the gravity vector of the axis of rotation of the limb, respectively during the stationary postures and movements;

110 *CHAPTER 6. MULTIPLE DEVICES FOR UPPER BODY MOTION
CAPTURE IN CHILDREN*

- step 3** An estimate of each axis of the FFs, relative to the corresponding SF, is obtained from the pre-processed data applying singular value decomposition (SVD). Moreover, associated to the estimates there is a measure of the reliability of the computed axis;
- step 4** Given the set of FFs axes and their estimates in the SFs, a regression algorithm, namely Levenberg Marquardt (LM), is applied to compute the transformation between each pair of systems of coordinates. Also, the reliability indices computed at step 3 are used to properly condition the regression algorithm.

The final purpose of the whole calibration procedure is to define the transformation between each SF and the corresponding FF arbitrarily fixed on the body, i.e. the rotation matrix \mathbf{R}_{SF}^{FF} . Eventually, its estimation allows the transition from the orientation information of the SUs to the kinematic description of the upper body.

Calibration movements

The first part of the calibration itself consists of a set of stationary postures and mono-axial, functional movements that participant has to perform. This approach relies on the two procedures that are commonly referred in the literature as "reference" and "functional" method, respectively [Kontaxis et al., 2009]. The aim of this first step of the protocol is to allow the identification of, at least, a pair of non-aligned axes on each FF of the body segments of interest. These axes are representative of certain directions of interest on the body, i.e. the transverse axis of a body segment, or of physiological motion, i.e. the axis of rotation of the shoulder joint during flexion-extension of the upper arm. For the kinematic tracking of the thorax and upper limbs in children, we propose the following calibration movement:

- **Thorax**

TS : Gravity vector measured in supine position with arms alongside the body and hand palms facing down (5 seconds)

TR : Rotation of the thorax around the transverse plane perpendicular axis while holding a bar (3-4 reps.), the movement is shown in the top left frame of Figure6.3

TFE : Flexion-Extension from standing position with legs opened at shoulder-width (3-4 reps.)

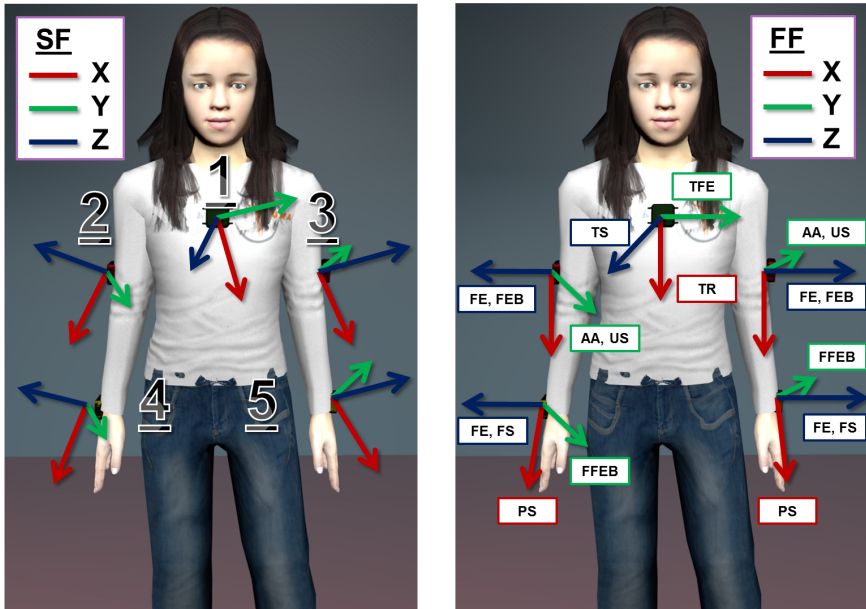


Figure 6.2: The figure shows the position of the SUs on the body segments (1 - Thorax, 2 - Right Upper Arm, 3 - Left Upper Arm, 4 - Right Forearm, 5 - Left Forearm) with their associated sensor frames (on the left) and a possible assignment of the body fixed FF (on the right). On the right, a possible assignment of the FF on the body is reported. Note that each movement in the calibration protocol list is matched to an axis in the FFs (refer to section 6.2 for the meaning of the acronyms).

- **Upper arm**

US : Gravity vector measured in supine position with arms alongside the body and hand palms facing down ((5 seconds)

AA : Ab-adduction from standing position with legs opened at shoulder-width (3-4 reps.), see bottom right frame of Figure6.3

FE : Flexion-Extension from standing position with legs opened at shoulder-width (3-4 reps.)

CHAPTER 6. MULTIPLE DEVICES FOR UPPER BODY MOTION
CAPTURE IN CHILDREN

112

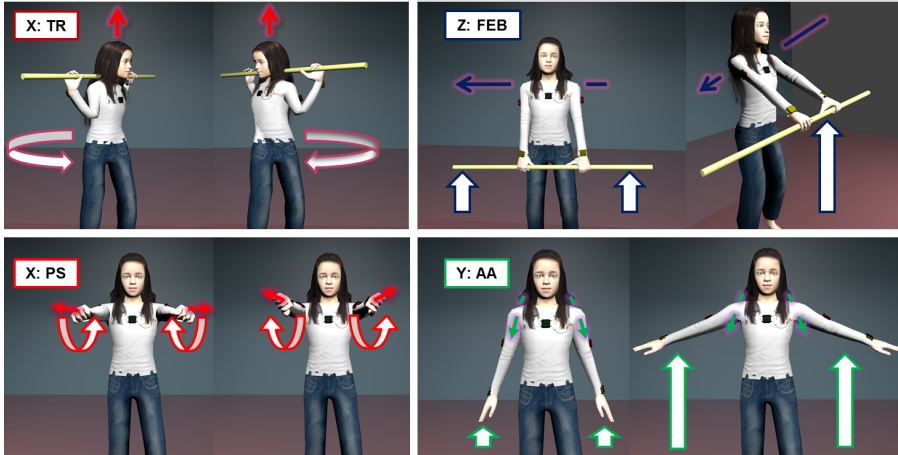


Figure 6.3: A subset of the calibration movements to be performed in the protocol. Clockwise from the top left we have: TR associated to the x-axis of FF_{Thorax} ; FEB of the upper arm associated to the z-axis of $FF_{Upperarm}$; AA of the upper arms associated to the y-axis of $FF_{Upperarm}$; PS of the forearms associated to the x-axis of $FF_{Forearm}$.

FEB : Flexion-Extension while holding a bar with hands at shoulder breadth with an adducted thumb grasp as shown in the top right frame of Figure6.3 (3-4 reps.)

- **Forearm**

FS : Gravity vector measured in supine position with arms alongside the body and hand palms facing down (5 seconds)

PS : Prono and supination movement with arms fully extended and hands closed (3-4 reps.), see bottom left frame of Figure6.3

FFEB : Flexion-Extension while holding a bar with hands at shoulder breadth and with upper arms close to the body (3-4 reps.)

All calibration movements were proposed to children as a short gym exercise. An adult played the role of coach and children were asked to observe one movement sequence before proceeding to execute the movement together with the coach. The reported list of movements and stationary postures identifies a

set of no less than 3 non-aligned axes for each body segment FF. The above list describes a single run of the calibration protocol and the complete experimental trial is composed of a set of 3 trials.

Data collection

Aiming at identifying meaningful axes for each body segment, we are interested in collecting two kinds of information during the protocol trials, i.e. accelerometers readings for the posture part and gyroscopes readings for the dynamic part. In fact, static accelerometers readings measure the direction of the gravity vector while the subject is lying in supine position with hand palms facing down. The gyroscopes, beforehand pruned from any constant bias, capture the angular velocity vector during movements and allow to identify the direction of the axis of rotation itself. In order to guarantee high signal-to-noise ratio of gyroscope measurements, a lower bound on the minimum angular velocity accepted in the data was set to the 30% of the maximum value. Each single measurement from accelerometers or gyroscopes is a vector of data in \mathbb{R}^3 made of the three axis sensor readings.

Reference axis identification

In order to estimate reference axes, datasets from each movement or reference pose were organized in the following measurements matrices, ${}^S\mathbf{A} = [{}^S\mathbf{a}_1, {}^S\mathbf{a}_2, \dots, {}^S\mathbf{a}_N]^T \in \mathbb{R}^{N \times 3}$ and ${}^S\mathbf{\Omega} = [{}^S\boldsymbol{\omega}_1, {}^S\boldsymbol{\omega}_2, \dots, {}^S\boldsymbol{\omega}_N]^T \in \mathbb{R}^{N \times 3}$, which consist of the N stacked readings from the accelerometers and the gyroscopes, respectively. After that, we applied singular value decomposition (SVD):

$$\begin{aligned} {}^S\mathbf{A} &= \mathbf{U} \boldsymbol{\Sigma}(\sigma_i) \mathbf{V}^T \\ {}^S\mathbf{\Omega} &= \mathbf{U} \boldsymbol{\Sigma}(\sigma_i) \mathbf{V}^T, \quad i = 1, 2, 3 \\ \mathbf{U} &\in \mathbb{R}^{N \times N}, \quad \boldsymbol{\Sigma} \in \mathbb{R}^{N \times 3}, \quad \mathbf{V} \in \mathbb{R}^{3 \times 3} \end{aligned} \quad (6.1)$$

where \mathbf{U} and \mathbf{V} are the orthonormal matrices coming out from the decomposition and containing an orthogonal basis for \mathbb{R}^N and \mathbb{R}^3 spaces, respectively. $\boldsymbol{\Sigma}$ is a diagonal matrix with the singular values on the main diagonal (σ_i). Based on the hypothesis of a stationary posture during the static part and a uni-axial movement during the dynamic part of the calibration protocol, the desired axis of reference will correspond to the right singular vector associated to the highest singular value ($\sigma_1 > \sigma_2 > \sigma_3$), i.e. the first column of \mathbf{V} .

This result can be explained adding the following considerations. In the ideal case of a flawless, mono-axial movement and noiseless measurements, the

CHAPTER 6. MULTIPLE DEVICES FOR UPPER BODY MOTION CAPTURE IN CHILDREN

114

angular velocity vectors will lay on a line in 3D Euclidean space, i.e. they are contained in a subspace of dimension 1. Instead, during the static part of the protocol the projections of the gravity vectors on each axis of the SF is assumed to be constant. Again, this implies that noise free accelerometers' readings are described by a subspace of dimension 1, specifically a point. Therefore, both \mathbf{A}^S and $\mathbf{\Omega}^S$ are expected to be rank 1 matrices in the ideal case. In practice, given the objective inability for a human being to perform a perfect mono-axial joint rotation, physiological movements while lying supine (e.g. movements due to breathing) and noise on the sensors' measurements, \mathbf{A}^S and $\mathbf{\Omega}^S$ will be full-rank. Therefore, what can be achieved with SVD is a robust discrimination between the useful information and disturbances, so to identify the underlying 1-rank submatrix with its vector basis, i.e. the axis of rotation.

In addition, the outcome of a singular value decomposition is used to define an index of the reliability for the computed axis, given by the following expression:

$$\rho = \frac{\sigma_1}{\sum_{i=1}^3 \sigma_i}, \quad \left[\frac{1}{3} \leq \rho \leq 1\right] \quad (6.2)$$

which is a dimensionless quantity representing the ratio of the largest singular value (σ_1) and the sum of all the diagonal entries of the Σ matrix. This index provides an indication about the quality of the collected dataset, in terms of how data distributes along directions orthogonal to the computed axis of reference. In the ideal case, ρ should be the unity. In the practical one, the higher the value of ρ , the more reliable is the collected dataset.

By applying this procedure to all the dataset captured during step 1 and 2, the outcome will be a set of pairs composed by an axis estimates and the corresponding reliability index (${}^S\vec{v}$, ρ), for any movement in the calibration list. Further, for each FF defined on the body segments of interest a set of at least two non-aligned axis estimates is available.

Transformation matrix computation

With the purpose of estimating the 3D rotation matrix (\mathbf{R}_{SF}^{FF}) relating each SF to its corresponding FF, the axes estimates together with their reliability indices are used in the Levenberg-Marquardt (LM) algorithm. In the following, without loss of generality, we describe the method for the case of the thorax segment ($\mathbf{R}_{SF}^{FF_{Thorax}}$), where exactly 3 axis estimates are available from the protocol, and will provide means to generalize the method to the other body

segments. As a first step, we construct the following vectors:

$$\vec{\mathbf{r}}^{FF} = \begin{bmatrix} \vec{\mathbf{x}}^{FF} \\ \vec{\mathbf{y}}^{FF} \\ \vec{\mathbf{z}}^{FF} \end{bmatrix}_{9 \times 1}, \quad \vec{\mathbf{v}}^{SF} = \begin{bmatrix} \vec{\mathbf{x}}^{SF} \\ \vec{\mathbf{y}}^{SF} \\ \vec{\mathbf{z}}^{SF} \end{bmatrix}_{9 \times 1} \quad (6.3)$$

where $\vec{\mathbf{r}}^{FF}$ is the set of canonical versors for the FF, i.e. $\vec{\mathbf{x}}^{FF} = [1 \ 0 \ 0]^T$, $\vec{\mathbf{y}}^{FF} = [0 \ 1 \ 0]^T$, $\vec{\mathbf{z}}^{FF} = [0 \ 0 \ 1]^T$, and $\vec{\mathbf{v}}^{SF}$ contains their corresponding estimates expressed in the SF. As shown in Figure 6.2, each versor in FF is ideally associated with a functional axis, e.g. $\vec{\mathbf{y}}^{FF}$ represents the thorax flexion-extension movement. The vectors $\vec{\mathbf{r}}^{FF}$ and $\vec{\mathbf{v}}^{SF}$ are related by the matrix:

$$\mathbf{Q} = \begin{bmatrix} \hat{\mathbf{R}}_{SF \ Thorax}^{FF} & & \\ & \hat{\mathbf{R}}_{SF \ Thorax}^{FF} & \\ & & \hat{\mathbf{R}}_{SF \ Thorax}^{FF} \end{bmatrix} \in \mathbb{R}^{9 \times 9} \quad (6.4)$$

which is a block diagonal matrix having the rotation matrix estimate repeated on the main diagonal. In the ideal case, when the estimates in $\vec{\mathbf{v}}_{est}^{SF}$ are orthogonal and right-handed and \mathbf{Q} contains the true \mathbf{R}_{SF}^{FF} , then the equality $\vec{\mathbf{r}}^{FF} = \mathbf{Q} \vec{\mathbf{v}}^{SF}$ is verified. In the real case, the versors composing $^{SF}\vec{\mathbf{v}}_{est}$ will most likely be not-aligned, rather than orthogonal. Thus we can define the following error function:

$$\boldsymbol{\epsilon} = (\vec{\mathbf{r}} - \mathbf{Q}(\hat{\mathbf{R}}) \vec{\mathbf{v}}) \quad (6.5)$$

where the symbol $\boldsymbol{\epsilon}$ is the vector of residuals. In order to properly condition the LM algorithm, we used the following cost function:

$$\mathbf{C}(\hat{\mathbf{R}}) = \boldsymbol{\epsilon}^T \mathbf{W} \boldsymbol{\epsilon} \quad (6.6)$$

where we introduced a matrix \mathbf{W} of weights build up from the reliability indices, associated to the $^{SF}\vec{\mathbf{v}}$ elements, and defined as:

$$\mathbf{W} = \begin{bmatrix} \rho_x \mathbf{I}_{3 \times 3} & & \\ & \rho_y \mathbf{I}_{3 \times 3} & \\ & & \rho_z \mathbf{I}_{3 \times 3} \end{bmatrix} \quad (6.7)$$

If no weights are used, i.e. $\mathbf{W} = \mathbf{I}$, the rotation matrix computed with the LM algorithm will be optimal in the sense of the least squares, i.e. minimizing the sum of squared residuals coming from equation (6.5). The advantage of introducing a matrix \mathbf{W} of weights, lies in the possibility to guide the optimization process in order to achieve a better fitting along the directions associated

CHAPTER 6. MULTIPLE DEVICES FOR UPPER BODY MOTION

116

CAPTURE IN CHILDREN

to the most reliable axes. Besides, the non-linear regression formulation will generate a rotation estimate expressed in the form of a unit norm quaternion, i.e. $\hat{\mathbf{q}}_{SF\ T_{thorax}}^{FF} = [q_0 \ \tilde{\mathbf{q}}]^T$. In order to convert quaternion back to a rotation matrix in the regression the following conversion formula must be used:

$$\mathbf{R}(\mathbf{q}) = \begin{bmatrix} q_0^2 + \mathbf{q}_x^2 - \mathbf{q}_y^2 - \mathbf{q}_z^2 & 2\mathbf{q}_x\mathbf{q}_y - 2q_0\mathbf{q}_z & 2\mathbf{q}_x\mathbf{q}_z + 2q_0\mathbf{q}_y \\ 2\mathbf{q}_x\mathbf{q}_y + 2q_0\mathbf{q}_z & q_0^2 + \mathbf{q}_y^2 - \mathbf{q}_x^2 - \mathbf{q}_z^2 & 2\mathbf{q}_y\mathbf{q}_z - 2q_0\mathbf{q}_x \\ 2\mathbf{q}_x\mathbf{q}_z - 2q_0\mathbf{q}_y & 2\mathbf{q}_y\mathbf{q}_z + 2q_0\mathbf{q}_x & q_0^2 + \mathbf{q}_z^2 - \mathbf{q}_x^2 - \mathbf{q}_y^2 \end{bmatrix}. \quad (6.8)$$

which avoids singularity issues when computing the Jacobian of the cost function. The k -th iteration step (Δ_k) of the LM regression algorithm is computed as:

$$\Delta_k = (\mathbf{J}_k^T \mathbf{W} \mathbf{J}_k + \lambda \text{diag}(\mathbf{J}_k^T \mathbf{W} \mathbf{J}_k))^{-1} \mathbf{J}_k^T \mathbf{W} \boldsymbol{\epsilon}_k \quad (6.9)$$

where \mathbf{J} is the Jacobian of the error function and λ is a damping parameter, which modulates the algorithm's behaviour. The error Jacobian can generally be computed as:

$$\mathbf{J} = \partial (\text{vec } \boldsymbol{\epsilon}) / \partial (\text{vec } \mathbf{q})^T \quad (6.10)$$

where the term *vec* indicates the vectorization operator which, for a matrix $A \in \mathbb{R}^{m \times n}$, is defined as:

$$\text{vec } A = [a_{11} \ \dots \ a_{m1} \ \dots \ a_{12} \ \dots \ a_{m2} \ \dots \ a_{n1} \ \dots \ a_{mn}]^T \quad (6.11)$$

Note that for the regression step the more efficient expression by Marquardt for the Fisher matrix ($\mathbf{F} = \mathbf{J}^T \mathbf{W} \mathbf{J} + \lambda \text{diag}(\mathbf{J}^T \mathbf{W} \mathbf{J})$) is used, which reduces the overall convergence time of the algorithm. After each iteration, estimated quaternion ($\hat{\mathbf{q}}$) has to be normalized in order to enforce the unit-norm constraint, which guarantees the estimate to be in the special orthogonal group $\text{SO}(3)$. Also, as an exit criterion for the regression, a lower bound on the percentage variation of the cost function is used (ε) and evaluated as:

$$\left| \frac{C(\hat{\mathbf{R}})_{k+1} - C(\hat{\mathbf{R}})_k}{C(\hat{\mathbf{R}})_k} \right| < \varepsilon \quad (6.12)$$

Beyond the presented case of the thorax, the method can be flexibly scaled according to the number of vector estimates available, with the caveat of a minimum of 2 estimates in order to unambiguously identify a rotation matrix. In the general case of a number N of estimates, the presented matrices and vectors will have the dimension:

$${}^{FF}\tilde{\mathbf{r}} \in \mathbb{R}^{3N \times 1}, \ {}^{SF}\tilde{\mathbf{v}} \in \mathbb{R}^{3N \times 1}, \ \mathbf{Q} \in \mathbb{R}^{3N \times 3N}, \ \mathbf{W} \in \mathbb{R}^{3N \times 3N} \quad (6.13)$$

Algorithm 1 Calibrate sensor to body segment frames

```

1: procedure CALIBRATE( $\mathbf{A}, \vec{\mathbf{r}}, \mathbf{q}_0$ )
2:   for  $t:=1$  to  $N$  do  $\triangleright$  compute axes estimates and  $\rho$  for the  $N$  trials
3:      $U\Sigma V^T = \text{svd}(\mathbf{A}_t)$ 
4:      $\vec{\mathbf{v}}_t = V_{(1:3,1)}$ 
5:      $\rho_t = \Sigma_{1,1}/(\Sigma_{1,1} + \Sigma_{2,2} + \Sigma_{3,3})$ 
6:   end for
7:    $\vec{\mathbf{v}} = [\vec{\mathbf{v}}_1^T \dots \vec{\mathbf{v}}_N^T]^T$   $\triangleright$  stack axes estimates in a column vector
8:    $\mathbf{W} = \text{diag}(\rho_1, \dots, \rho_N)$ 
9:    $\hat{\mathbf{q}}_k = \mathbf{q}_0$ 
10:  while  $|(C_{k+1} - C_k)/C_k| > \varepsilon$  do  $\triangleright$  regression stop condition
11:     $\epsilon_k = (\vec{\mathbf{r}} - \mathbf{Q}(\hat{\mathbf{q}}_k) \vec{\mathbf{v}})$ 
12:     $\mathbf{J}_k = \partial(\text{vec } \epsilon_k)/\partial(\text{vec } \mathbf{q}_k)^T$ 
13:     $\Delta_k = (\mathbf{J}_k^T \mathbf{W} \mathbf{J}_k + \lambda \text{diag}(\mathbf{J}_k^T \mathbf{W} \mathbf{J}_k))^{-1} \mathbf{J}_k^T \mathbf{W} \epsilon_k$ 
14:     $\hat{\mathbf{q}}_{k+1} = \hat{\mathbf{q}}_k - \Delta_k$ 
15:     $\hat{\mathbf{q}}_{k+1} / \|\hat{\mathbf{q}}_{k+1}\|$ 
16:  end while
17:  return  $\hat{\mathbf{R}}(\hat{\mathbf{q}}_{k+1})$   $\triangleright$  The calibration matrix is  $\hat{\mathbf{R}}$ 
18: end procedure

```

Concluding, the algorithm steps are summarized in 1 and further details on the theory of LM algorithm and its implementations can be found in [Hartley and Zisserman, 2000].

6.3 Results

In this section results obtained with the proposed procedure are reported. First, the method is validated in simulation using artificially generated datasets and its performance is compared with another approach from the literature [de Vries et al., 2010]. Then, results on real datasets from a population of 40 children are detailed.

Simulation results

To the purpose of validating the proposed method, a simulated trial was devised to be representative of a typical experimental setting. The trial consists in a set of 3 functional movements along different, orthogonal axes of rotation. Each

CHAPTER 6. MULTIPLE DEVICES FOR UPPER BODY MOTION
CAPTURE IN CHILDREN

118

individual movement is repeated for 3 times and a time series of synthetic gyroscope readings, to be representative of real data obtained from functional movements, is generated with the following sequence of steps. First, a value for the calibration matrix $\hat{\mathbf{R}}_{FF}^{SF}$ is set. The columns of this matrix are the versors ($\vec{\mathbf{v}}_i$) representing the functional axes of rotation in the SF (i.e. the ones to be identified by the SVD analysis). Around each individual axes, a sinusoidal pattern for the angular velocity (\mathbf{w}_i) is assumed. Amplitude and frequency of oscillation are set, accordingly to experimental observation, to a value of 3 rad/s and 0.5 Hz, i.e.:

$$\mathbf{w}_i(t) = 3\sin(\pi t)\vec{\mathbf{v}}_i, \quad i = 1, \dots, 3 \quad (6.14)$$

and a duration of 10 s is hypothesized for each angular velocity recording. Upon generated datasets a noise term ($\boldsymbol{\nu}$) is superimposed distributed as a zero-mean Gaussian with a standard deviation $\sigma = 6$ mrad/s, where this value is obtained from the gyroscopes used in the experimentation. As the axis of rotation during a functional movement is hardly a constant (plus noise), another disturbance term is introduced that accounts for deviation of the axis itself during the simulated motion. This is expressed as a unit norm quaternion (\mathbf{q}_{rand}^*) that rotates the functional axis about an orthogonal direction ($\vec{\mathbf{a}}$) by an angle θ . The latter is randomly selected and can have a maximum value of 45° . Instead, the axis can be any direction on the plane orthogonal to $\vec{\mathbf{v}}_i$. In order to generate data with a different quality level, in terms of mono-axiality of the movement, the incidence of this type of rotational disturbance is varied among the 3 datasets comprised by each individual functional movement. Synthetic measurements are implemented as:

$$\begin{aligned} \tilde{\mathbf{w}}_{mi}[kT] &= \mathbf{q}_{rand}^*(\theta, \vec{\mathbf{a}}) \otimes \tilde{\mathbf{w}}_i[kT] \otimes \mathbf{q}_{rand}^*(\theta, \vec{\mathbf{a}}) + \boldsymbol{\nu}, \quad i = 1, \dots, 3 \\ \tilde{\mathbf{w}} &= [0, \mathbf{w}^T]^T \end{aligned} \quad (6.15)$$

where \mathbf{w}_m is the simulated angular velocity measurement, the symbol \otimes denotes quaternion product and the angular velocity vector (\mathbf{w}) is appended with an extra 0 component in order to carry out vector rotation with quaternions, as defined in A.6. An example of simulated dataset is shown in Figure 6.4. In the following tractation, simulated dataset will be used to validate the methods with respect to the ability to robustly identify reference axis from gyroscope datasets and to estimate the correct calibration matrix.

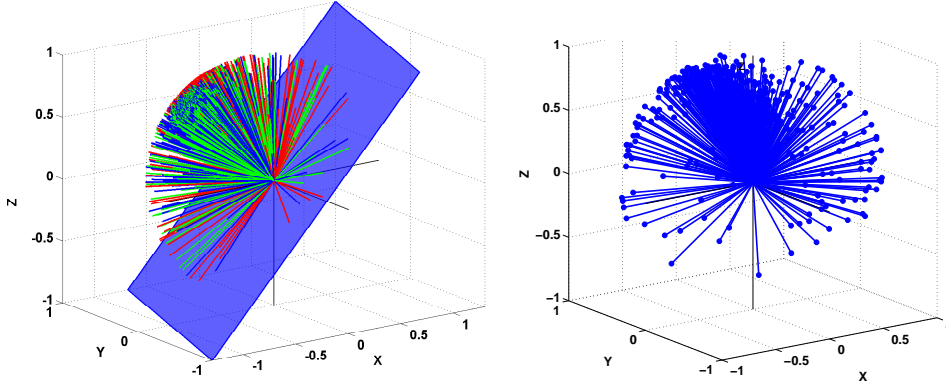


Figure 6.4: The figure reports spatial dispersion of the axis of rotation obtained from a simulated gyroscope dataset (on the left), where data are segmented and normalized. The same plot is also displayed for a set of normalized, segmented gyroscope measurements from an experimental trial (on the right). In the simulated case, the true axis of rotation is known and it is displayed as its normal plane.

Reference axis identification

Proposed method for axis identification, based on SVD, is compared with the recent procedure proposed in [de Vries et al., 2010]. The latter is based on repeated averaging of datasets and requires data segmentation in order to invert the negative half-wave of the sinusoidal angular velocity pattern. An axis of rotation was set and 100 different datasets were generated according to the formula in (6.15). For each individual dataset, its axis of rotation is estimated with both methods and an error is computed using the metric:

$$\Phi(\vec{v}, \vec{r}) = \text{acos}(\vec{v} \cdot \vec{r}) \quad (6.16)$$

where \vec{v} is the estimated axis, \vec{r} is the reference and \cdot denotes vector dot product. Results are shown in Figure 6.5, both as the individual errors (top plot) and their difference (bottom plot), and better performance of the proposed method is observed. In addition, a statistical analysis using Student's t-test on the errors, beforehand tested for Gaussianity, confirmed the significance of the result ($\rho < 0.05$).

CHAPTER 6. MULTIPLE DEVICES FOR UPPER BODY MOTION
CAPTURE IN CHILDREN

120

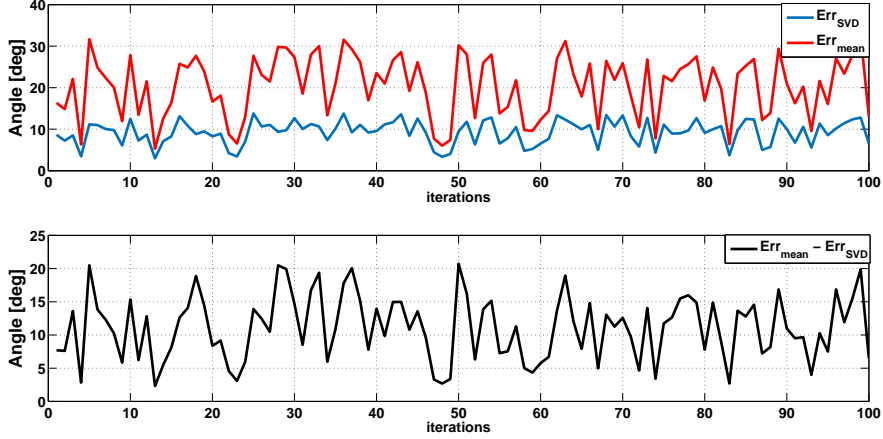


Figure 6.5: The figure compares the proposed method to identify axis of rotation, based on SVD, to the method described in [de Vries et al., 2010], based on averaging. The error is represented as the angular distance between the estimated axis and the known reference. The bottom plot reports difference between errors with the two methods.

Transformation matrix estimation

The whole calibration procedure described in this chapter is compared with the recent method proposed by de Vries and colleagues [de Vries et al., 2010], demonstrated on adult subjects. The latter is based on averaging the individual datasets comprising each functional movement session in order to obtain multiple axes estimates. The functional axis is extracted from the multiple estimates via an extra averaging operation. Also, a dispersion parameter is computed, which quantifies repeatability of the functional axis estimate itself. Better axes, differed according to this parameter, are then used for the calibration matrix estimation and the remaining are discarded. A number of 100 different simulated trials were generated according to the procedure above mentioned (see 6.3) and the two methods were applied. Estimated calibration matrices (\hat{R}) were compared to the ground truth using the metric:

$$\Phi(R, \hat{R}) = \text{acos}\left(\frac{\text{trace}(R^T \hat{R}) - 1}{2}\right) \quad (6.17)$$

6.3. RESULTS

121

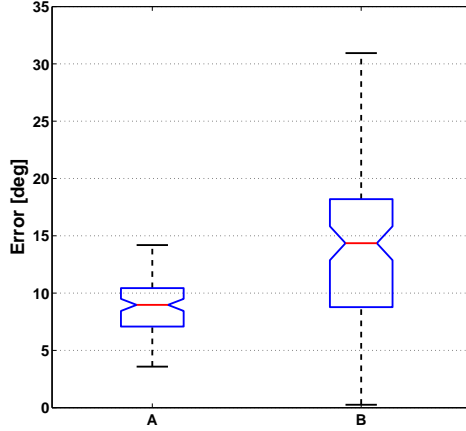


Figure 6.6: The figure shows a boxplot of the errors in the estimated calibration matrix with the proposed method (A) and the procedure described in [de Vries et al., 2010] (B). Errors are reported as the median value (red line), the interquartile range (blue notch) and the maximum and minimum values (black whiskers in the figure).

which represent the geodesic distance on the $SO(3)$ space, where rotation matrices are defined. Results are reported in Figure 6.6 as a boxplot showing the median, interquartile range and maximum and minimum values of the error. Simulations reveal a higher repeatability of the proposed method and a major robustness against the presence of highly disturbed (in the sense of formula (6.15)) datasets in the functional movement recordings. Finally, a statistical analysis using Student's t-test on the errors, beforehand tested for Gaussianity, confirmed the significance of the better performance of the proposed method ($\rho < 0.05$).

Experimental results

Experimental data were collected on the group of 40 children with methodology described above. The recorded calibration movements were processed in order to extract reference axes together with their reliability measure (ρ) of the estimate. In table 6.1 the values of the proposed reliability index are reported, where the reliability parameter is expressed as the mean value \pm standard devi-

122 CHAPTER 6. MULTIPLE DEVICES FOR UPPER BODY MOTION
CAPTURE IN CHILDREN

Calibration Movement	Thorax	Upper Arm L	Upper Arm R	Forearm L	Forearm R
<i>Supine on the ground</i>	0.98 ± 0.007	0.98 ± 0.023	0.98 ± 0.015	0.98 ± 0.029	0.98 ± 0.020
<i>Thorax rotation on the transverse plane</i>	0.84 ± 0.038	-	-	-	-
<i>Thorax flexion-extension</i>	0.84 ± 0.038	-	-	-	-
<i>Forearm flexion-extension with bar</i>	-	-	-	0.80 ± 0.056	0.79 ± 0.067
<i>Upper arm flexion-extension with bar</i>	-	0.68 ± 0.048	0.69 ± 0.041	0.75 ± 0.068	0.76 ± 0.076
<i>Upper arm flexion - extension</i>	-	0.65 ± 0.044	0.67 ± 0.040	0.60 ± 0.054	0.62 ± 0.055
<i>Upper arm abb-adduction</i>	-	0.62 ± 0.049	0.64 ± 0.040	0.56 ± 0.051	0.58 ± 0.046
<i>Forearm prono-supination</i>	-	0.73 ± 0.104	0.74 ± 0.089	0.88 ± 0.057	0.89 ± 0.057

Table 6.1: The table reports values obtained for the reliability index ρ relative to each calibration movement. The index is a dimensionless number in the range $[\frac{1}{3}, 1]$ and it is reported mean \pm SD computed over a population of 40 subjects.

ation evaluated over the whole group of subjects. The set of axes estimates and ρ values are eventually passed as input to the LM algorithm. The identity rotation, i.e. $\hat{\mathbf{q}}_0 = [1, 0, 0, 0]$, is set as initial condition for the regression and a value of $\lambda = 0.001$ is selected for the damping factor of the LM algorithm, which is a typical assumption for this parameter (refer to Appendix A6 in [Hartley and Zisserman, 2000]). Moreover, we set the convergence criterion lower threshold to $\varepsilon = 10^{-4}$. Given those initialization values, the number of iterations the algorithm undergoes in the average case before attaining convergence is the following, again expressed as mean and standard deviation:

- Thorax FF: 6.34 ± 0.561 iterations
- Upper arm FF (left and right): 8.36 ± 0.767 iterations
- Forearm FF (left and right): 7.30 ± 0.863 iterations

6.3. RESULTS

123

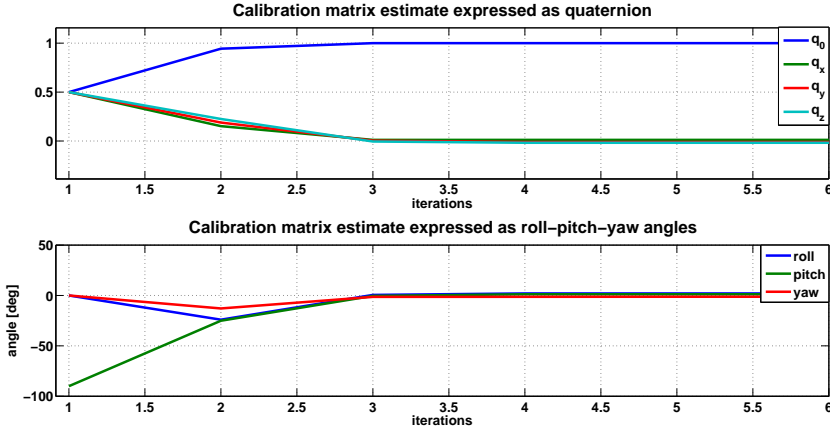


Figure 6.7: The figure reports the typical converging behaviour of the LM algorithm. On the left, the trend of the \mathbf{R}_{SF}^{FF} matrix estimate relative to the FF_{Thorax} is shown, respectively expressed in the form of a unit norm quaternion (top) and as Euler roll, pitch and yaw angles (bottom).

As an example of the converging behaviour of the LM algorithm, we reported the case of the thorax FF rotation matrix in Figure6.7. Besides, in this particular case we stressed the algorithm performance giving random initialization values as input and we still observed the attainment of convergence after a moderate number of iterations (6 in the case of Figure6.7).

With the purpose of gaining further insight into the behaviour of our regression algorithm, we focused on the error function, particularly on the vector of residuals ϵ . As formalized in equation (6.5), this vector is made of the Euclidean differences between each FF canonical axis (i.e. the versors $\hat{\mathbf{x}}$, $\hat{\mathbf{y}}$ and $\hat{\mathbf{z}}$) and its corresponding estimate, both expressed in the FF system of coordinates. The aim of the regression algorithm would be that of mitigating these differences, by making matched pairs of vectors ($\vec{\mathbf{v}}_{ref}, \vec{\mathbf{v}}_{est}$) pointing to approximately the same directions in \mathbb{R}^3 space, i.e. the closer as possible in accordance with the mathematical constraints associated to the rotation matrix $\hat{\mathbf{R}}_{SF}^{FF}$ (e.g. orthogonality of the column vectors). In our weighted formulation of the LM algorithm, some pairs of vector are expected to get closer than others, depending on the value of their reliability index. In addition, the pairs that get closer are also the ones that mostly affect the computation of the transfor-

CHAPTER 6. MULTIPLE DEVICES FOR UPPER BODY MOTION
CAPTURE IN CHILDREN

124

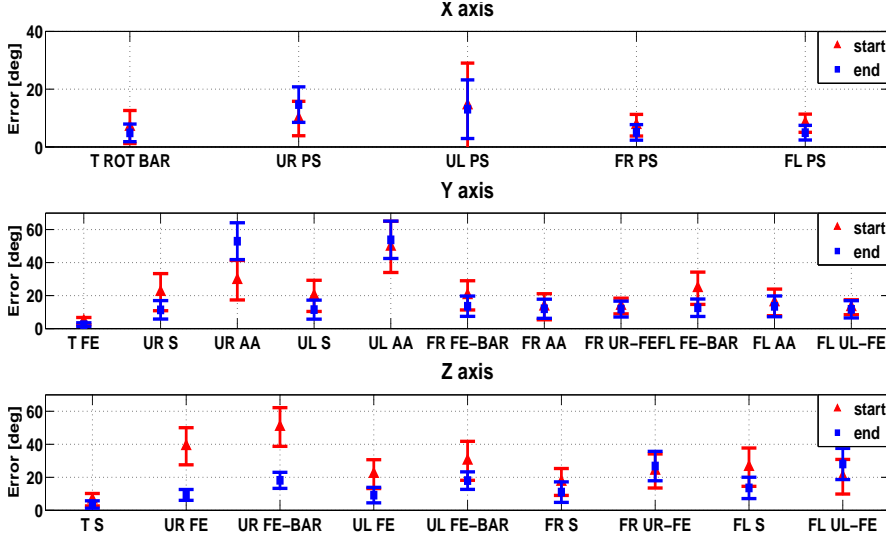


Figure 6.8: Comparison of the differences between pairs $(\vec{v}_{ref}, \vec{v}_{est})$ of axes estimates and their FF matches, computed at the beginning and at the end of the LM regression (refer to section 6.2 for the meaning of the acronyms). As a distance metric we considered the angle between each pair of vectors, computed as the arccosine of their dot product (see relation (6.16)).

mation matrix $\hat{\mathbf{R}}_{SF}^{FF}$. In order to visualize this effect, we made a comparison of the values of these differences at the first step, when $\hat{\mathbf{R}}_{SF}^{FF} = \mathbf{I}_{3 \times 3}$, and at the convergence of the regression algorithm, $\hat{\mathbf{R}}_{SF}^{FF} = \underset{\mathbf{R}}{\operatorname{argmin}}(\mathbf{C}(\mathbf{R}))$. As a distance metric we considered:

$$\mathbf{d}(\vec{v}_{ref}, \vec{v}_{est}) = \operatorname{acos}(\vec{v}_{ref}^T \vec{v}_{est}) \quad (6.18)$$

that is the angle between each pair of vectors. The analysis was extended to the whole set of 40 children and we reported the results, expressed as mean and standard deviation, for each movement in Figure6.11. As a further result, in Figure6.9 an example of kinematic reconstruction of the joint angles for the forearm and the upper arm during the flexion–extension movement is presented. As an outcome of the calibration procedure, minimal kinematic cross-talk is expected when the user perform movements involving only one axis, as in the

6.3. RESULTS

125

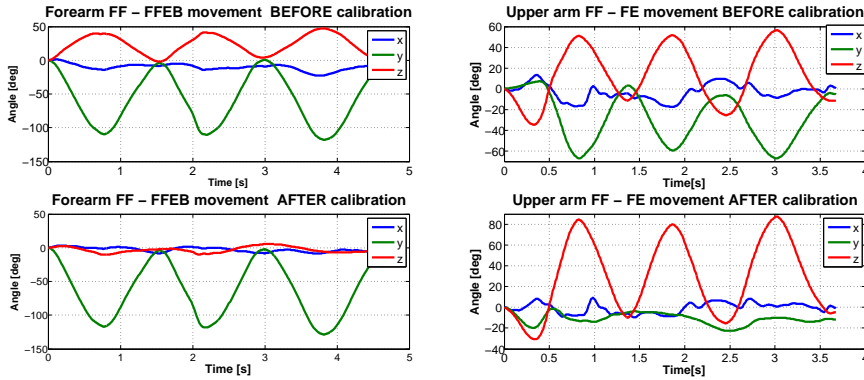


Figure 6.9: The figure reports example of kinematic calibration for the right forearm and upper arm. Reduced kinematic cross-talking is observable on the bottom plots that display angular velocities during the flexion-extension (FE) movement and the supported forearm flexion-extension (FFEB) w.r.t the FF.

case reported. We observed a general reduction in the range of motion of the angles that are not associated with the motion: in the case of the forearm, the range of motion resulted decreased of 45% and 70%, respectively for the x and z axes, and increased of 8% for the y axis; in the case of the upper arm, the range of motion resulted decreased of 38.7% and 69.7%, respectively for the x and y axes, and increased of about the 30% for the z axis.

Upper body kinematic tracking

The result reported in this section is relative to the use of wearable IMU devices, that are capable of measuring 3D orientation, combined with the presented calibration procedure, that allows estimating a calibration matrix between the sensor reference frame and the human body functional frames, in order to track upper body kinematics in real time. A part from the aforementioned components, the missing elements to achieve the motion capturing are a kinematic model of the upper body and a pre-defined reference pose, used to initialize the tracking.

CHAPTER 6. MULTIPLE DEVICES FOR UPPER BODY MOTION
CAPTURE IN CHILDREN

126



Figure 6.10: The figure shows the kinematic chain implemented for the avatar used for motion reconstruction of the upper body kinematics. All joints are set as ball in a socket type. Orientation data from the wearable IMUs are mapped to the movable segments (in red) through the estimated calibration matrix.

Kinematic modeling of upper body

The human upper body is kinematically modelled as a chain of segments connected through ball in a socket type joints, i.e. no physiological motion constraint is introduced. Despite this assumption is a poor choice in terms of the capacity of the model to be a realistic representation of the human body, it comes with the advantage of introducing no extra artifact in the mapping between IMU measurements and human motion. Therefore, any issue related to calibration, drifts of the sensors or soft tissue artifacts are easily identifiable. The model is composed of 5 segments (left forearm, left upper arm, thorax, right upper arm, right forearm), shown in Figure6.10. It has been created with the Blender 3D animation suite [Blender,] and then exported to the OGRE graphics engine [OGRE,] which is used to implement the virtual environment of the developed software platform. Data stream from the IMU devices are received in real time by the software components and orientation, expressed as unit norm quaternion (\mathbf{q}_s), is converted into motion of a virtual avatar limbs as:

$$\mathbf{q}_a(t) = \mathbf{q}_i^* \otimes \mathbf{q}_c^* \otimes \mathbf{q}_s^*(t_r) \otimes \mathbf{q}_s(t) \otimes \mathbf{q}_c \quad (6.19)$$



Figure 6.11: The figure reports a screenshot of the software platform developed during a real time motion reconstruction session, using the calibration data from the procedure presented in this chapter. The video is available at <http://youtu.be/QQWP0kd4sOU>.

where \mathbf{q}_a is the orientation of the avatar's limb and \mathbf{q}_c is the constant calibration matrix, expressed as a quaternion. The remaining terms are respectively the initialization pose for the limb (\mathbf{q}_i), w.r.t a global reference frame which is defined into the OGRE engine, and $\mathbf{q}_s(t_r)$ is the value of the orientation from the IMU at the reset time t_r . In fact, for practical implementation of the tracking, both the subject and the avatar must have the same initial stance and, once this condition is achieved, IMU measurements should be resetted to the identity quaternion.

6.4 Discussions

In this chapter a novel calibration protocol for the kinematic tracking of the thorax and upper limbs with IMU wearable sensors, designed to be used with children is presented. This method allows a user to define functional coordinate systems (FF), that are fixed on the body segments, and to estimate the relation between a IMU sensor's frame and its corresponding body segment's FF. The proposed calibration procedure itself is composed by a sequence of functional movements and a methodology to elaborate sensor data, in order to compute a rotation matrix relating each SF to the corresponding, arbitrarily defined

128 *CHAPTER 6. MULTIPLE DEVICES FOR UPPER BODY MOTION
CAPTURE IN CHILDREN*

FF (i.e. \mathbf{R}_{SF}^{FF}). Selected movements have the twofold purpose of identifying a sufficient number of non-aligned axes on each defined FF, at least 2, and conforming to the constraints of being easy to perform and short in duration, in order to avoid children's fatigue and to reduce overall duration of experimental sessions.

In fact, as highlighted in a previous study [Ricci et al., 2013] and as it is also observed during the experimentation, some movements are easier to perform for children (6-7 yo) than others: as an example, the thorax lateral flexion, used in similar calibration protocols with adults [de Vries et al., 2010], resulted an improper choice for children. Furthermore, given the difficulty to maintain children's attention for a long time compared to adults, the calibration protocol was designed in order to limit duration while maintaining a substantial number of functional axis estimates, as suggested in [Luinge et al., 2007]. In addition, the protocol was presented to the child as a game of imitation: an adult plays the role of the coach and the subject is asked to mirror his movements. This experimental methodology is specific for an usage with children as it brings the twofold benefit of: (i) making it easier for children to understand how the movements should be performed; (ii) having an adult checking the correctness of the movement. No difficulties were encountered in the experimentation with the proposed list and in all but the thorax case a redundant number of functional axes were identified, with respect to the minimum of two non-aligned axes that is required in order to estimate a rotation matrix. Moreover, a novel data analysis approach eliminates the typical need of a segmentation process, which usually involves a rest period between any two phases of a rotation movement, e.g. to differ the flexion from the extension phase, as reported in [de Vries et al., 2010, Luinge et al., 2007, Cutti et al., 2008]. Thus, with the presented methodology the duration of this part of the protocol is further reduced (i.e. total duration is 15 minutes).

In view of the necessity that may arise to prune the list of movements to the minimum of 2 axes per FF, a reliability index (ρ), that is defined basing on the outcome of a singular value decomposition, as reported in 6.2, was introduced to qualify the estimated axes, as reported in table 6.1. The index of reliability is computed from measurement matrices containing repetitions (from 9 to 12) of the same functional movement or reference posture and thus gives an indication about the precision of the child's performance. In the ideal case of a noiseless sensing units, the maximum value of the index is the unity and it is obtained when exactly the same axis of rotation is involved in each repetition of the movement. Instead, the minimum value of the index ($\rho = \frac{1}{3}$), is mathematically obtained in the case when each repetition of the movement

6.4. DISCUSSIONS

129

belongs to a different axis of rotation and those axes are orthogonal, e.g. that would be the extreme case in which a subject is asked to perform three times a flexion-extension of the upper arm and he instead performs first a flexion-extension, then an ab-adduction and finally a prono-supination. Further, high precision in the execution of a movement translates in a high repeatability of the estimated reference axis. The proposed list of movements deliberately included the same physiological movement (i.e. flexion and extension) executed with or without the support of a rigid bar. The reason for that is the possibility to evaluate if, as expected from intuition, the introduction of an external support to further facilitate children coordination improves the reliability of some movements. From the reported table, the reliability index indicates the supported movement is more repeatable than the unsupported one. Also, statistical analysis using a paired t-test on the normally distributed reliability datasets confirmed significance ($p < 0.05$) of the result both for the forearm FFs and for the upper arm FFs. In Figure 6.11 a visualization of the residual distance between vector pairs $(\vec{v}_{ref}, \vec{v}_{est})$, as defined in 6.18, at the beginning and at the end of the LM regression and for each movement in the calibration protocol is proposed. We observe a general trend of the pairs of axes estimates and corresponding FF reference axes to reduce their angular distance at the end of the regression. If more than one estimate for the same FF axis is available, the regression algorithm will favour the one with the higher reliability value. For instance, this is true for the case of the supine posture ($\rho = 0.98$ and $\rho = 0.99$) versus the abduction and adduction movement ($\rho = 0.62$ and $\rho = 0.64$) of the upper arms on the Y axis estimation of the associated FF. The thorax resulted the body segment with the overall highest reliability and with the lowest residual distance between the pairs $(\vec{v}_{ref}, \vec{v}_{est})$ in the rotation matrix estimation, respectively 5.39° , 2.56° and 2.86° for the x, y and z component. This is due to a proper choice of the calibration movements for the thorax, with reference to both the repeatability and the fact that the set of axes estimated during each movement/reference pose are close to an orthogonal frame. Moreover, this result is in accordance with what discussed in [de Vries et al., 2010], where the functional frame built on the thorax also prove to be the most compatible with the anatomical frame defined by the ISB recommendations [Wu et al., 2005]. The prono-supination of the forearm is the most reliable movement for the functional part of this specific FF and its associated axis is the most repeatable, in agreement with similar studies in literature [de Vries et al., 2010, Ricci et al., 2013]. Also, the residual angular distance for the pairs $(\vec{v}_{ref}, \vec{v}_{est})$ amounts to 4.68° for the left and 4.72° for the right forearm.

The standard way to estimate the rotation matrix \mathbf{R}_{SF}^{FF} in the current liter-

CHAPTER 6. MULTIPLE DEVICES FOR UPPER BODY MOTION
CAPTURE IN CHILDREN

130

ature [de Vries et al., 2010],[Luinge et al., 2007],[Wu et al., 2005],[Cutti et al., 2008] is that of using a single pair of non-aligned axis estimates to get an orthonormal frame via successive vector products. This method is referred in literature with the name of TRIAD (TRi-axial Attitude Determination) algorithm and was originally proposed as a solution to the Wahba's problem [Wahba, 1965]. Our approach to \mathbf{R}_{SF}^{FF} estimation overcomes the known limitations of the TRIAD algorithm, in the sense that it is capable of accommodating more than two axis estimates, it is not sensible to the order at which the axis estimates are considered and, more importantly, can exploit all the available information (i.e. both the axis direction and its repeatability measure). As an outcome to the method we reported in Figure 6.9 an example of kinematic reconstruction for the right upper limb. Though the evidence of a substantial reduction in kinematic cross-talking for single joint movements with the proposed calibration methodology, future research endeavour should focus on comparison with data collected using optical motion capture systems, which are still ranked as the golden standard for motion capture, for a validation on experimental data. In the meanwhile, meaningful motion reconstruction results obtained with the proposed procedure are in favour of the effectiveness of the method.

Finally, the presented method only requires the subject to be able to perform simple calibration movements in order to enable the estimation of the relations among reference frames. Despite this requirement is met in most of the applications, it is still possible to imagine scenarios in which it may not be feasible to ask the subject to perform even simple but controlled movements, e.g. when dealing with motor or cognitive impaired subjects. For those cases, a possible solution could be that of using additional instrumentation in order to perform the initial calibration procedure. Among the range of possibilities, depth cameras (e.g. Microsoft Kinect) could be a promising choice. This class of devices is now available at low cost, feature a high portability and allow a reasonably accurate reconstruction of human body kinematics [Fernández-Baena et al., 2012]. The latter can be combined with kinematic information from the uncalibrated IMUs in order to infer the required calibration parameters. The challenge there is to infer a proper mapping between the two different sensing modalities, accounting for the relative reference frames and the way they are defined, the functional limitations and the different types of sources of error affecting the systems.

Chapter 7

Concluding remarks

The evolution of inertial sensors has brought to an ubiquitous presence of this technology in an increasing number of devices. Aside from inertial quantities, advancements in the algorithms that are embedded within these sensors are transforming them into attractive solutions for motion tracking. As a result, inertial sensors have a widespread use in a plethora of different and novel areas of application, including biomedical and robotics.

In consideration of that, the purpose of this dissertation is twofold: on the one side, it proposes to investigate the performance in tracking achievable using this technology. On the other, it extends the use of inertial sensors in the area of robotic navigation and of human motion capture. The presented work aims and accomplishes the research goals stated in Section 1.3: an extensive validation of accuracy in orientation tracking with wearable inertial sensors providing comprehensive information on error ranges and major sources of disturbance; the autonomous self calibration and navigation of an omnidirectional wheeled robotic platform equipped with an onboard inertial sensor; the calibration of human body fixed reference frames from wearable inertial sensors' readings, in view of meaningfully reconstructing motion of children from inertial orientation information.

7.1 Conclusions

This dissertation thesis presented innovative methods and results aimed at supporting the improvement over state of the art and the extension of the field of application for wearable inertial sensors.

A first contribution of this work was to establish a reliable baseline for accuracy in orientation tracking to be expected from inertial sensors: this information was not available in the literature at the time of this writing. The assessment was carried out using an accurate robotic manipulator in order to generate controlled and repeatable testing conditions. Both static and dynamic accuracy were validated. For the latter, a number of different periodic motions were generated with a bandwidth picked in the range of frequencies that are commonly found in human motion studies. Additionally, inertial measurements were processed using two different sensor fusion approaches for orientation estimation, that were selected among the most relevant classes of algorithms in the literature. Results showed that the worst case absolute accuracy to be expected is within about 8° for the whole set of experimented conditions. For some application relative accuracy computed between two inertial devices is of interest, e.g. for multiple segment tracking or human joint angle measurement. In that case, it was found that accuracy slightly degraded to a worst case upper bound of about 10° . Further, it was shown that accuracy is also dependent on the bandwidth and the amplitude of the movement: as a general rule of thumb, the magnitude of the error is proportional to the dynamics. Interestingly, a decrement of performance was also observed when passing from performing rotations against the gravity to rotations along the gravity axis. In the latter case, the orientation computed via sensor fusion is more sensitive to magnetic field perturbations. Though perturbations are potentially compensated for by the fusion algorithms, it was found to be still one of the main issue in determining performance of orientation tracking for this technology.

A second contribution discussed in this dissertation pertains to the autonomous navigation of an omnidirectional wheeled robotic platform. Two novel methods were introduced in order to achieve, respectively, robot self calibration of the systematic sources of error of the odometry and robust dead reckoning navigation (e.g. against wheel slippage). The methods were tested on an experimental robotic platform that was designed, having in mind the eventual application in an industrial setting. The importance of this contribution to state of the art research on robotic navigation lies in the fact that this class of robots, that feature a superior mobility on the ground, has been traditionally overlooked, both in the research and industrial areas, due to the additional difficulties that are introduced by the use of omnidirectional wheels (i.e. they are prone to slippage). Furthermore, currently explored approaches to navigation mainly rely on exteroceptive optical sensors (e.g. cameras or laser) which makes them liable in case of occlusions. The presented methods exploit only information coming from proprioception and the knowledge

7.2. FUTURE WORKS

133

of parametric models characterizing the robot and the sensors. From different experimental trials, it was demonstrated how the use of an inertial sensor as additional onboard sensor (strapped down to the robot frame) combined with the proposed sensor fusion methods lead to a significant improvements of performance in navigation. This in consideration of the fact that, with traditional odometry based navigation, when wheel slippage occurs, an error is introduced in the robot heading estimate. Error on the heading in turn, builds up into an error on the position estimate that grows unbounded with the traveled distance.

A third and final novel result presented in this thesis is the design of a calibration protocol for the kinematic tracking of the thorax and upper limbs with inertial wearable sensors adapted to be used with children. The protocol consisted of a series of functional movements and reference poses, intended to generate a number of highly informative inertial datasets to the final aim of defining reference frames that describe upper body kinematic chain. Together with the protocol, two methods for extracting functional axis from inertial recordings and defining reference frames on human body segments were presented. The proposed approach to axis extraction requires no preprocessing of the inertial datasets. Aside from the direction of the axis, it also indicates the reliability of the estimate. Both information are used in a properly tailored nonlinear regression algorithm that generates the body fixed reference frames. The two methods were extensively validated in simulation and their improvement in performance with respect to state of the art approaches was demonstrated. Moreover, the calibration protocol was extensively tested on a population of 40 children (6–7 yr). Note that the experimentation was carried out in unstructured daily life setting (i.e. a school). Results showed a substantial reduction in kinematic cross-talking for single joint movements with the proposed calibration methodology. Though a comparison with optical reference should be considered as a future research endeavour, the effectiveness of the method was also demonstrated via visually verified motion reconstruction results.

7.2 Future works

This dissertation spanned over various aspects related to the use of wearable inertial sensors and therefore different potential directions for future works can be identified.

In chapter 4 the topic of validating the state of the art technology performance in tracking was addressed. A part for the detrimental effect of movement

dynamics on the performance, which could be mitigated or adjusted by tuning of the algorithms' parameters, the major limitation to tracking are the magnetic field variations. Though compensation strategies have been proposed in the literature, in practice they prove not so effective in complex indoor environments. In view of that, future research endeavours could address investigating methods for better compensating against magnetic perturbation (e.g. by detecting the disturbance and automatically recalibrating magnetometers) or for exploiting the complexity in the magnetic field pattern to the aim of navigation (e.g. magnetic SLAM).

In chapter 5 inertial navigation with an omnidirectional robotic platform was explored. Here the future challenge could be that of pushing the limits of the proposed approach. Inertial sensors proved to be the natural complement to optical encoders. The latter output very neat but prone to outliers (e.g. during wheel slippage) 2D data. Instead, inertial measurements are noisier, prone to integration drift but enrich the 2D odometry information with 3D data, practically enabling the ground robot to sense the terrain on which it is navigating. The impression is that the combination of the two information sources could prove effective in a number of different scenarios (e.g. in outdoor terrains) other than the one experimented in this work.

Finally in chapter 6 methodologies for defining reference frames on human body, particularly suitable for use with children, were presented. In this case, directions for future works are already established. In fact, the collection of inertial datasets of children was carried out as part of a more extensive research project (i.e. the TOUM [TOUM,]), that was ultimately aiming at analyzing motor behavior during gesture production in children. Particularly, part of doctoral activities were committed to collecting inertial datasets of children performing different ad-hoc motor tasks and motor assessment tests. In addition, experimentation was carried out on a group of typically developing children and a group of children affected by autistic spectrum disorder (ASD). In consideration of that, future research will address analysis of inertial and kinematic information that can now be extracted from the data as a result of the developed calibration procedure.

List of publications

Parts of this dissertation thesis have been previously published or submitted for publication.

7.3 Peer-reviewed journals

L. Ricci, F. Taffoni and D. Formica. “The orientation error of IMU: investigating static and dynamic accuracy targeting human motion.” *IEEE Transaction on Neural Systems and Rehabilitation Engineering*, [SUBMITTED].

L. Ricci, D. Formica, L. Sparaci, F.R. Lasorsa, F. Taffoni, E. Tamilia and E. Guglielmelli. “A New Calibration Methodology for Thorax and Upper Limbs Motion Capture in Children Using Magneto and Inertial Sensors.” *Sensors*, 14(1):1057–1072, 2014.

F. Taffoni, E. Tamilia, V. Focaroli, D. Formica, L. Ricci, G. Di Pino, G. Baldassarre, M. Mirolli, E. Guglielmelli and F. Keller. “Development of goal-directed action selection guided by intrinsic motivations: an experiment with children.” *Experimental brain research*, 232(7):2167–2177, Lug 2014.

E. Tamilia, F. Taffoni, D. Formica, L. Ricci, E. Schena, F. Keller and E. Guglielmelli. “Technological solutions and main indices for the assessment of newborns nutritive sucking: a review.” *Sensors*, 14(1):634–658, 2014.

7.4 Peer-reviewed conferences

L. Ricci and D. Formica. “Dynamic accuracy assessment of data-fusion techniques for wearable, inertial and magnetic based human motion capture.” *In Proceedings of IEEE SENSORS*, pages 2215–2218, Valencia, Spain, Nov 2014.

L. Ricci and D. Formica. “An experimental protocol for the definition of upper limb anatomical frames on children using magneto-inertial sensors.” *In Proceedings of 35th IEEE International Conference on Engineering in Medicine and Biology Society (EMBC)*, pages 4903 –4906, Osaka, Japan, Jul 2013.

E. Tamilia, F. Taffoni, E. Schena, D. Formica, L. Ricci and E. Guglielmelli. “A new ecological method for the estimation of Nutritive Sucking Efficiency in newborns: Measurement principle and experimental assessment.” *In Proceedings of 35th IEEE International Conference on Engineering in Medicine and Biology Society (EMBC)*, pages 6720–6723, Osaka, Japan, Jul 2013.

7.5 National and international conferences

L. Ricci, D. Formica and E. Guglielmelli. “Validation of wearable magnetoinertial tracking system accuracy with a robotic arm.” *In Proceedings of Congresso del Gruppo Nazionale di Bioingegneria*, Pavia, Italy, Jun 2014.

Appendix A

Quaternion algebra

This appendix briefly introduces unit norm quaternions as a way to represent orientation in 3D space. Their most basic properties are hereby stated, without proof. For more details, see e.g. [KUIPERS, 1999]. Quaternions are a generalization of complex number to a 4-dimensional space (\mathbb{Q}_1), and are defined as:

$$\mathbf{q} \doteq (q_0 \ \vec{\mathbf{q}})^T \doteq (q_0 \ q_x \mathbf{i}, \ q_y \mathbf{j}, \ q_z \mathbf{k})^T \doteq \pm \left(\cos\left(\frac{\theta}{2}\right) \ \vec{\mathbf{v}} \sin\left(\frac{\theta}{2}\right) \right)^T \in \mathbb{Q}_1 \quad (\text{A.1})$$

where q_0, q_x, q_y, q_z are real numbers, \mathbf{v} and θ are respectively the axis and the angle of rotation and the primitive elements $\mathbf{i}, \mathbf{j}, \mathbf{k}$ satisfy the following property:

$$\begin{aligned} \mathbf{i}^2 &= \mathbf{j}^2 = \mathbf{k}^2 \\ \mathbf{ij} &= -\mathbf{ji} = \mathbf{k} \\ \mathbf{jk} &= -\mathbf{kj} = \mathbf{i} \\ \mathbf{ki} &= -\mathbf{ik} = \mathbf{j} \end{aligned} \quad (\text{A.2})$$

A.1 Basic properties of quaternions

1. The *conjugate* of a quaternion is defined as:

$$\mathbf{q}^* \doteq (q_0 \ -\vec{\mathbf{q}})^T \quad (\text{A.3})$$

2. The *addition* (*subtraction*) between quaternions is defined as:

$$\begin{aligned}\mathbf{q}_A \pm \mathbf{q}_B &\doteq (q_{0A} + q_{xA}\mathbf{i} + q_{yA}\mathbf{j} + q_{zA}\mathbf{k}) \pm (q_{0B} + q_{xB}\mathbf{i} + q_{yB}\mathbf{j} + q_{zB}\mathbf{k}) \\ &\doteq (q_{0A} \pm q_{0B}) + (q_{xA} \pm q_{xB})\mathbf{i} + (q_{yA} \pm q_{yB})\mathbf{j} + (q_{zA} \pm q_{zB})\mathbf{k}\end{aligned}\quad (\text{A.4})$$

3. The *quaternion multiplication* is defined as:

$$\begin{aligned}\mathbf{q}_A \otimes \mathbf{q}_B &\doteq (q_{0A} + q_{xA}\mathbf{i} + q_{yA}\mathbf{j} + q_{zA}\mathbf{k})(q_{0B} + q_{xB}\mathbf{i} + q_{yB}\mathbf{j} + q_{zB}\mathbf{k}) = \\ &\quad (q_{0A}q_{0B} - q_{xA}q_{xB} - q_{yA}q_{yB} - q_{zA}q_{zB}) + \\ &\quad (q_{0A}q_{xB} + q_{xA}q_{0B} + q_{yA}z1 - q_{zA}q_{yB})\mathbf{i} + \\ &\quad (q_{0A}q_{yB} - q_{xA}q_{zB} + q_{yA}q_{0B} + q_{zA}q_{xB})\mathbf{j} + \\ &\quad (q_{0A}q_{zB} + q_{xA}q_{zB} - q_{yA}q_{xB} + q_{zA}q_{0B})\mathbf{k}.\end{aligned}\quad (\text{A.5})$$

4. The *vector rotation* of $\mathbf{v} \in \mathbb{R}^3$ by a quaternion $\mathbf{q} \in \mathbb{Q}_1$ is defined as:

$$\mathbf{q} \otimes \tilde{\mathbf{v}} \otimes \mathbf{q}^* \quad (\text{A.6})$$

where $\tilde{\mathbf{v}} \in \mathbb{Q}$ is an augmented 4-vector generated from the original 3-vector as:

$$\tilde{\mathbf{v}} = \begin{bmatrix} 0 \\ \mathbf{v} \end{bmatrix} \quad (\text{A.7})$$

5. The natural *logarithm* of a quaternion is defined as:

$$\log \mathbf{q} = \left(\log \|\mathbf{q}\| \quad \frac{\vec{\mathbf{q}}}{\|\vec{\mathbf{q}}\|} \cos^{-1} \frac{q_0}{\|\mathbf{q}\|} \right) \quad (\text{A.8})$$

A.2 Spherical Linear Interpolation

The spherical linear interpolation [Shoemake1985, 1985] between two quaternions \mathbf{q}_A and \mathbf{q}_B is defined as:

$$\text{slerp}(\mathbf{q}_A, \mathbf{q}_B, t) = \mathbf{q}_A \frac{\sin(1-t)\Omega}{\sin \Omega} + \mathbf{q}_B \frac{\sin t\Omega}{\sinh \Omega}. \quad (\text{A.9})$$

where Ω is the angle subtended by the two quaternions, i.e.:

$$\cos \Omega = \mathbf{q}_A \cdot \mathbf{q}_B \quad (\text{A.10})$$

Appendix B

Orientation conversion

There are different possible parameterizations to describe orientation. This appendix provides the conversion formulas between the unit norm quaternions and the other orientation representations used throughout this dissertation.

B.1 Axis and angles

A unit norm quaternion can be decomposed into an axis (\hat{n}) and angle (θ) representation as:

$$\theta = 2 * \cos^{-1}(q_0) \quad , \quad \hat{n} = \frac{\hat{q}}{\|\hat{q}\|} \quad (\text{B.1})$$

An axis and angle representation can be found combined into a rotation vector $\mathbf{r} = \hat{n}\theta$. In this case, conversion from and to a quaternion is given:

$$\mathbf{q} = \exp\left(-\frac{1}{2}\mathbf{r}\right) \quad , \quad \mathbf{r} = -2\log(\mathbf{q}) \quad (\text{B.2})$$

where the quaternion logarithm is defined in A.8.

B.2 Rotation matrix

A unit norm quaternion \mathbf{q} can be converted to a rotation matrix \mathbf{R} in SO3 with the following relation:

$$\mathbf{R} = \begin{pmatrix} q_0^2 + q_x^2 - q_y^2 - q_z^2 & 2q_xq_y - 2q_0q_z & 2q_xq_z + 2q_0q_y \\ 2q_xq_y + 2q_0q_z & q_0^2 - q_x^2 + q_y^2 - q_z^2 & 2q_yq_z - 2q_0q_x \\ 2q_xq_z - 2q_0q_y & 2q_yq_z + 2q_0q_x & q_0^2 - q_x^2 - q_y^2 + q_z^2 \end{pmatrix}. \quad (\text{B.3})$$

where the elements of the quaternion are defined according to

B.3 Euler angles

Euler angles are a minimal parametrization of the orientation that use a sequence of three rotations around coordinate axes. A popular sequence derived from the aeronautical field is termed roll–pitch–yaw. In this case, one rotates first an angle ψ about the z-axis (yaw), then an angle θ around the y-axis (pitch) and finally an angle ϕ around the x-axis (roll). Those angles can be derived from a unit norm quaternion as:

$$\psi = \tan^{-1} \frac{2(q_0q_z - q_xq_y)}{1 - 2(q_y^2 + q_z^2)} \quad (\text{B.4})$$

$$\theta = \sin^{-1}(2(q_0q_y + q_zq_x)) \quad (\text{B.5})$$

$$\phi = \tan^{-1} \frac{2(q_0q_x - q_yq_z)}{1 - 2(q_x^2 + q_y^2)} \quad (\text{B.6})$$

Bibliography

- [Allan, 1966] Allan, D. (1966). Statistics of atomic frequency standards. *Proceedings of the IEEE*, 54(2).
- [Ang and Khoo, 2004] Ang, W. and Khoo, S. (2004). Physical model of a MEMS accelerometer for low-g motion tracking applications. In *Proceedings of the 2004 International Conference on Robotics & Automation*, number April, pages 1345–1351.
- [Aragus, 2015] Aragus, G Paz, C. G. D. P. G. P. (2015). Quaternion-based Orientation Estimation Fusing a Camera and Inertial Sensors for a Hovering UAV. *Journal of Intelligent and Robotic Systems*, 77(1):37–53.
- [Bachmann et al., 2007] Bachmann, B. Y. E. R., Yun, X., and Brumfield, A. (2007). Investigating the Effects of Magnetic Variations on Inertial/ Magnetic Orientation Sensors. *IEEE Robotics and Automation Magazine*.
- [Bar-Itzhack, 1996] Bar-Itzhack, I. Y. (1996). REQUEST: A Recursive QUEST Algorithm for Sequential Attitude Determination. *Journal of Guidance, Control, and Dynamics*, 19(1):1034–1038.
- [Barralon et al., 2005] Barralon, P., Noury, N., Vuillerme, N., Timsit, L., and Aïme, E. (2005). Classification of Daily Physical Activities from a Single Kinematic Sensor. pages 2447–2450.
- [Bergamini et al., 2014] Bergamini, E., Ligorio, G., Summa, A., Vannozzi, G., Cappozzo, A., and Sabatini, A. (2014). Estimating Orientation Using Magnetic and Inertial Sensors and Different Sensor Fusion Approaches: Accuracy Assessment in Manual and Locomotion Tasks. *Sensors*, 14(10):18625–18649.
- [Blender,] Blender. *Blender*. Available at <http://www.blender.org/>.

- [Bonato, 2003] Bonato, P. (2003). Wearable sensors/systems and their impact on biomedical engineering. *IEEE Engineering in Medicine and Biology Magazine*, 22(3):18–20.
- [Bonato, 2005] Bonato, P. (2005). Advances in wearable technology and applications in physical medicine and rehabilitation. *Journal of neuroengineering and rehabilitation*, 2(1):2.
- [Bonnet et al., 2009] Bonnet, S., Bassompierre, C., Godin, C., Lesecq, S., and Barraud, a. (2009). Calibration methods for inertial and magnetic sensors. *Sensors and Actuators A: Physical*, 156(2):302–311.
- [Borenstein and Feng, 1996] Borenstein, J. and Feng, L. (1996). Measurement and Correction of Systematic Odometry Errors in Mobile Robots. 12(6).
- [Boyd and Vandenberghe, 2010] Boyd, S. and Vandenberghe, L. (2010). *Convex Optimization*, volume 25.
- [Britain and Engineering, 1987] Britain, G. and Engineering, M. (1987). Kinematics of vehicles with directional sliding wheels. 22(4):295–301.
- [Brodie et al., 2008a] Brodie, M., Walmsley, . A. A., and Page, W. (2008a). Fusion motion capture : a prototype system using inertial measurement units and GPS for the biomechanical analysis of ski racing Research Article. (1):17–28.
- [Brodie et al., 2008b] Brodie, M. a., Walmsley, a., and Page, W. (2008b). Dynamic accuracy of inertial measurement units during simple pendulum motion. *Computer methods in biomechanics and biomedical engineering*, 11(3):235–42.
- [Brodie et al., 2008c] Brodie, M. a., Walmsley, A., and Page, W. (2008c). The static accuracy and calibration of inertial measurement units for 3D orientation. *Computer methods in biomechanics and biomedical engineering*, 11(6):641–8.
- [Campion et al., 1996] Champion, G., Bastin, G., and Andrca-novel, B. D. (1996). Structural Properties and Classification of Kinematic and Dynamic Models of Wheeled Mobile Robots. 12(1).
- [Campolo et al., 2006] Campolo, D., Fabris, M., Cavallo, G., Accoto, D., Keller, F., and Guglielmelli, E. (2006). A Novel Procedure for In-field

- Calibration of Sourceless Inertial / Magnetic Orientation Tracking Wearable Devices. In *The First IEEE/RAS-EMBS International Conference on Biomedical Robotics and Biomechatronics, 2006.*, pages 471–476.
- [Campolo et al., 2009] Campolo, D., Schenato, L., Pi, L., Deng, X., and Guglielmelli, E. (2009). Attitude Estimation of a Biologically Inspired Robotic Housefly via Multimodal Sensor Fusion. *Advanced Robotics*, 23(7):955–977.
- [Campolo et al., 2012] Campolo, D., Taffoni, F., Formica, D., Iverson, J., Sparaci, L., Keller, F., and Guglielmelli, E. (2012). A Mechatronic Platform for Assessing Development of Spatial Cognition in Infants. *Journal of Integrative Neuroscience*, 11(1):103–116.
- [Collin, 2014] Collin, J. (2014). MEMS IMU Carouseling for Ground Vehicles. *IEEE Transactions on Vehicular Technology*, 9545(c):1–1.
- [Cooper et al., 2009] Cooper, G., Sheret, I., McMillan, L., McMillian, L., Siliverdis, K., Sha, N., Hodgins, D., Kenney, L., and Howard, D. (2009). Inertial sensor-based knee flexion/extension angle estimation. *Journal of biomechanics*, 42(16):2678–85.
- [Cox, 1991] Cox, I. J. (1991). Blanche—An experiment in guidance and navigation of an autonomous robot vehicle. *IEEE Transactions on Robotics and Automation*, 7(2):193–204.
- [Crassidis et al., 2007] Crassidis, J., Markley, F. L., and Cheng, Y. (2007). A Survey of Nonlinear Attitude Estimation Methods. *AIAA Journal of Guidance, Control, and Dynamics*, 30(1):12–28.
- [Crock et al., 2001] Crock, R. V., Horvat, M., and McCarthy, E. (2001). Reliability and concurrent validity of the movement assessment battery for children. *Perceptual and Motor Skills*, 93:275–280.
- [Cutti et al., 2010] Cutti, A. G., Ferrari, A., Garofalo, P., Raggi, M., Cappello, A., and Ferrari, A. (2010). 'Outwalk': a protocol for clinical gait analysis based on inertial and magnetic sensors. *Medical & biological engineering & computing*, 48(1):17–25.
- [Cutti et al., 2006] Cutti, A. G., Giovanardi, A., Rocchi, L., and Davalli, A. (2006). A simple test to assess the static and dynamic accuracy of an inertial sensors system for human movement analysis. pages 5912–5915.

- [Cutti et al., 2008] Cutti, A. G., Giovanardi, A., Rocchi, L., Davalli, A., and Sacchetti, R. (2008). Ambulatory measurement of shoulder and elbow kinematics through inertial and magnetic sensors. *Medical & biological engineering & computing*, 46(2):169–78.
- [de Vries et al., 2010] de Vries, W. H. K., Veeger, H. E. J., Cutti, a. G., Baten, C., and van der Helm, F. C. T. (2010). Functionally interpretable local coordinate systems for the upper extremity using inertial & magnetic measurement systems. *Journal of biomechanics*, 43(10):1983–8.
- [Dissanayake et al., 2001] Dissanayake, G., Sukkarieh, S., Nebot, E., and Durrant-whyte, H. (2001). The Aiding of a Low-Cost Strapdown Inertial Measurement Unit Using Vehicle Model Constraints for Land Vehicle Applications. *IEEE Transactions on Robotics and Automation*, 17(5):731–747.
- [El-Gohary and McNames, 2012] El-Gohary, M. and McNames, J. (2012). Shoulder and elbow joint angle tracking with inertial sensors. *IEEE transactions on bio-medical engineering*, 59(9):2635–41.
- [Elkaim, 2008] Elkaim, G. Foster, C. (2008). Extension of a non-linear, two-step calibration methodology to include non-orthogonal sensor axes. *IEEE Journal of Aerospace Electronic Systems*, 44:575587.
- [Fernández-Baena et al., 2012] Fernández-Baena, A., Susín, A., and Lligadas, X. (2012). Biomechanical validation of upper-body and lower-body joint movements of kinect motion capture data for rehabilitation treatments. In *Proceedings of the 2012 4th International Conference on Intelligent Networking and Collaborative Systems, INCoS 2012*, pages 656–661.
- [Ferraris et al., 1995] Ferraris, F., Grimald, U., and Parvis, M. (1995). Procedure for Effortless In-Field Calibration of Three-Axis Rate Gyros and Accelerometers. *Sensors and Materials*, 7(5):311–330.
- [Fitzgerald, 2013] Fitzgerald, A. M. (2013). A Practical Guide to MEMS Inertial Sensors. In *Stanford PNT Symposium*.
- [Fong et al., 2008] Fong, W. T., Ong, S. K., and Nee, a. Y. C. (2008). Methods for in-field user calibration of an inertial measurement unit without external equipment. *Measurement Science and Technology*, 19:085202.

BIBLIOGRAPHY

145

- [Fourati et al., 2012] Fourati, H., Manamanni, N., Afilal, L., and Handrich, Y. (2012). A Complementary Sliding Mode Observer Approach for Motions Human Body Segments Capturing by Means of Wearable Inertial and Magnetic MEMS Sensors Assembly. pages 1–12.
- [Foxlin, 2005] Foxlin, E. (2005). Pedestrian tracking with shoe-mounted inertial sensors. *IEEE Computer Graphics and Applications.*, 25(6):38–46.
- [Fuke and Krotkov, 1996] Fuke, Y. and Krotkov, E. (1996). Dead reckoning for a lunar rover on uneven terrain. In *Robotics and Automation, Proceedings IEEE International Conference*, volume Vol. 1, pages 411–416.
- [Gilmore et al., 2010] Gilmore, R., Sakzewski, L., and Boyd, R. (2010). Upper limb activity measures for 5- to 16-year-old children with congenital hemiplegia: a systematic review. *Developmental medicine and child neurology*, 52(1):14–21.
- [Godfrey et al., 2008] Godfrey, A., Conway, R., Meagher, D., and Ólaighin, G. (2008). Direct measurement of human movement by accelerometry. 30:1364–1386.
- [Godwin et al., 2009] Godwin, A., Agnew, M., and Stevenson, J. (2009). Accuracy of inertial motion sensors in static, quasistatic, and complex dynamic motion. *Journal of biomechanical engineering*, 131(11):114501–114505.
- [Gustafsson, 2013] Gustafsson, F. (2013). *Statistical Sensor Fusion*.
- [Han et al., 2010] Han, K.-L., Kim, H., and Lee, J. S. (2010). The sources of position errors of omni-directional mobile robot with Mecanum wheel. *2010 IEEE International Conference on Systems, Man and Cybernetics*, pages 581–586.
- [Hardt von der et al., 1998] Hardt von der, H.-J., Husson, R., and Wolf, D. (1998). An Automatic Calibration Method for a Multisensor System: Application to a Mobile Robot Localization System. In *IEEE International Conference on Robotics and Automation*, number May, pages 3141–3146.
- [Hartley and Zisserman, 2000] Hartley, R. I. and Zisserman, A. (2000). *Multiple View Geometry in Computer Vision*. Cambridge University Press, second edition.
- [Hastie and Friedman, 2009] Hastie, T Tibshirani, R. and Friedman, J. (2009). *The Elements of Statistical Learning*.

- [Henderson and Sugden, 1992] Henderson, S. and Sugden, D. (1992). Movement Assessment Battery for Children. *The Psychological Corporation: London, UK*.
- [Horn, 1987] Horn, B. K. P. (1987). Closed-form solution of absolute orientation using unit quaternions. *Journal of the Optical Society of America A*, 4(4):629.
- [Hunt and Hobbs, 1964] Hunt, G. W. and Hobbs, A. E. W. (1964). Development of an accurate tuning-fork gyroscope, in Symposium on Gyros. In *Proceedings of the Institute of Mechanical Engineers (London)*, pages 1964–65.
- [Huynh, 2009] Huynh, D. Q. (2009). Metrics for 3D Rotations: Comparison and Analysis. *Journal of Mathematical Imaging and Vision*, 35(2):155–164.
- [Ilon, 1975] Ilon, B. E. (1975). Wheels for a course stable self-propelling vehicle movable in any desired direction on the ground or some other base.
- [Indiveri, 2009] Indiveri, G. (2009). Swedish Wheeled Omnidirectional Mobile Robots: Kinematics Analysis and Control. *IEEE Transactions on Robotics*, 25(1):164–171.
- [J.Woodman, 2009] J.Woodman, O. (2009). An introduction to inertial navigation. Technical Report 696.
- [Killpack et al., 2010] Killpack, M., Deyle, T., Anderson, C., and Kemp, C. C. (2010). Visual odometry and control for an omnidirectional mobile robot with a downward-facing camera. *2010 IEEE/RSJ International Conference on Intelligent Robots and Systems*, pages 139–146.
- [Kim and Yi, 2009] Kim, D. Y. and Yi, K. Y. (2009). A user-steered guide robot for the blind. *2008 IEEE International Conference on Robotics and Biomimetics*, pages 114–119.
- [Kok et al., 2012] Kok, M., Hol, J. D., and Sch, T. B. (2012). Calibration of a magnetometer in combination with inertial sensors. In *15th International Conference on Information Fusion (FUSION)*, pages 787–793.
- [Kontaxis et al., 2009] Kontaxis, a., Cutti, a. G., Johnson, G. R., and Veeger, H. E. J. (2009). A framework for the definition of standardized protocols for measuring upper-extremity kinematics. *Clinical biomechanics (Bristol, Avon)*, 24(3):246–53.

BIBLIOGRAPHY

147

- [KUIPERS, 1999] KUIPERS, J. B. (1999). *Quaternions and Rotation Sequences: A Primer with Applications to Orbits, Aerospace and Virtual Reality*. Princeton University Press, New Jersey.
- [KUKA,] KUKA. *Kuka Laboratories GmbH*. <http://www.kuka-labs.com/>.
- [Lamon and Siegwart, 2004] Lamon, P. and Siegwart, R. (2004). Inertial and 3D-odometry fusion in rough terrain - towards real 3D navigation. In *2004 IEEE/RSJ International Conference on Intelligent Robots and Systems (IROS)*, volume 2, pages 1716–1721. Ieee.
- [Lebel et al., 2013] Lebel, K., Boissy, P., Hamel, M., and Duval, C. (2013). Inertial Measures of Motion for Clinical Biomechanics: Comparative Assessment of Accuracy under Controlled Conditions - Effect of Velocity. *PloS one*, 8(11):e79945.
- [Lehmann, 1998] Lehmann, E. L. (1998). *Theory of Point Estimation*.
- [Lötters J.C. et al., 1998] Lötters J.C., Schipperb, J., P.H. Veltink, Olthuisd, W., and Bergveldd, P. (1998). A Procedure for in-use calibration of triaxial accelerometers in medical applications. *Sensors and Actuators A: Physical*, 68(98):221–228.
- [Luinge, 2002] Luinge, H. J. (2002). *Inertial sensing of human movement*. PhD thesis, Twente.
- [Luinge et al., 2007] Luinge, H. J., Veltink, P. H., and Baten, C. T. M. (2007). Ambulatory measurement of arm orientation. *Journal of biomechanics*, 40(1):78–85.
- [Madgwick et al., 2011] Madgwick, S. O. H., Harrison, A. J. L., and Vaidyanathan, A. (2011). Estimation of IMU and MARG orientation using a gradient descent algorithm. *IEEE ... International Conference on Rehabilitation Robotics : [proceedings]*, 2011:5975346.
- [Mahony et al., 2008] Mahony, R., Member, S., Hamel, T., and Pflimlin, J.-m. (2008). Nonlinear Complementary Filters on the Special Orthogonal Group. *IEEE TRANSACTIONS ON AUTOMATIC CONTROL*, 53(5):1203–1218.
- [Mann et al., 1989] Mann, K. A., Werner, F. W., and Palmer, A. K. (1989). Frequency Spectrum Analysis of Wrist Motion for Activities of Daily Living. (2):304–306.

- [Martinelli et al., 2006] Martinelli, A., Tomatis, N., and Siegwart, R. (2006). Simultaneous localization and odometry self calibration for mobile robot. *Autonomous Robots*, 22(1):75–85.
- [McCollum and Peters, 1924] McCollum, B. and Peters, O. S. (1924). A new electrical telemeter. *[United States] Bureau of Standards. Technologic papers*, (247):737–777.
- [Mohd-Yasin et al., 2009] Mohd-Yasin, F., Nagel, D. J., and Korman, C. E. (2009). Noise in MEMS. *Measurement Science and Technology*, 21:012001.
- [Necsulescu et al., 1993] Necsulescu, D. S., Sasiadek, J. Z., Kim, B., Green, D. N., and Ks, C. (1993). Fusion of Inertial and Kinematic Navigation Systems for Autonomous Vehicles. In *IEEE International Conference on Vehicle Navigation and Information Systems*, pages 462–465.
- [NGDC,] NGDC. *National Geophysical Data Center*. <http://www.ngdc.noaa.gov/geomag/WMM>.
- [OGRE,] OGRE. *Object-Oriented Graphics Rendering Engine*. Available at <http://www.ogre3d.org/>.
- [Ojeda and Borenstein, 2002] Ojeda, L. and Borenstein, J. (2002). FLEXnav: fuzzy logic expert rule-based position estimation for mobile robots on rugged terrain. In *Proceedings 2002 IEEE International Conference on Robotics and Automation*, volume 1.
- [Pa et al., 2012] Pa, P., Rohá, J., and Nová, P. (2012). Analyses of Triaxial Accelerometer Calibration Algorithms. 12(5):1157–1165.
- [Papoulis, 2002] Papoulis, A. (2002). *Probability, Random Variables and Stochastic Processes*.
- [Patel et al., 2012] Patel, S., Park, H., Bonato, P., Chan, L., and Rodgers, M. (2012). A review of wearable sensors and systems with application in rehabilitation. *Journal of NeuroEngineering and Rehabilitation*, 9(1):21.
- [Pettenati et al., 2009] Pettenati, S., Stefanini, S., and Volterra, V. (2009). Motoric characteristics of representational gestures produced by young children in a naming task. *Journal of child language*.
- [Picerno et al., 2008] Picerno, P., Cereatti, A., and Cappozzo, A. (2008). Joint kinematics estimate using wearable inertial and magnetic sensing modules.

BIBLIOGRAPHY

149

- [Picerno et al., 2011] Picerno, P., Cereatti, A., and Cappozzo, A. (2011). Gait & Posture A spot check for assessing static orientation consistency of inertial and magnetic sensing units. *Gait & Posture*, 33(3):373–378.
- [Pintelon and Schoukens, 2012] Pintelon, R. and Schoukens, J. (2012). *System Identification: A Frequency Domain Approach*.
- [Purwin and DAndrea, 2006] Purwin, O. and DAndrea, R. (2006). Trajectory generation and control for four wheeled omnidirectional vehicles. *Robotics and Autonomous Systems*, 54(1):13–22.
- [Pylvanainen, 2008] Pylvanainen, T. (2008). Automatic and adaptive calibration of 3d field sensors. *Applied Mathematical Modelling*, 32:575587.
- [Quick, 1964] Quick, W. H. (1964). Theory of the vibrating string as an angular motion sensor. *Transactions of the ASME Journal of Applied Mechanics*, 24:523–534.
- [Ricci et al., 2014] Ricci, L., Formica, D., Sparaci, L., Lasorsa, F. R., Taffoni, F., Tamilya, E., and Guglielmelli, E. (2014). A New Calibration Methodology for Thorax and Upper Limbs Motion Capture in Children Using Magneto and Inertial Sensors. *Sensors (Basel, Switzerland)*, 14:1057–1072.
- [Ricci et al., 2013] Ricci, L., Formica, D., Tamilya, E., Taffoni, F., Sparaci, L., Capirci, O., and Guglielmelli, E. (2013). An Experimental Protocol for the Definition of Upper Limb Anatomical Frames on Children Using Magneto–inertial Sensors. *Proceedings of the 35th Annual International Conference of the IEEE EMBC. Osaka*, 6.
- [Roetenberg,] Roetenberg, D. *Inertial and Magnetic Sensing of Human Motion*.
- [Roetenberg et al., 2005] Roetenberg, D., Luinge, H. J., Baten, C. T. M., and Veltink, P. H. (2005). Compensation of magnetic disturbances improves inertial and magnetic sensing of human body segment orientation. *IEEE transactions on neural systems and rehabilitation engineering : a publication of the IEEE Engineering in Medicine and Biology Society*, 13(3):395–405.
- [Roetenberg et al., 2007] Roetenberg, D., Slycke, P. J., and Veltink, P. H. (2007). Ambulatory Position and Orientation Tracking Fusing Magnetic and Inertial Sensing. 54(5):883–890.

- [ROS,] ROS. *Robotic Operating System*. <http://www.ros.org/>.
- [Russell et al., 2000] Russell, D., Avery, L., Rosenbaum, P., Raina, P., Walter, S., and R, P. (2000). Improved scaling of the gross motor function measure for children with cerebral palsy: evidence of reliability and validity. *Physical Therapy*, 80(9):873–885.
- [Sabatini, 2005] Sabatini, A. M. (2005). inertial sensing to gait analysis. 43(2002).
- [Sabatini, 2011] Sabatini, A. M. (2011). Kalman-filter-based orientation determination using inertial/magnetic sensors: observability analysis and performance evaluation. *Sensors (Basel, Switzerland)*, 11(10):9182–206.
- [Sabatini and Member, 2006] Sabatini, A. M. and Member, S. (2006). Quaternion-Based Extended Kalman Filter for Determining Orientation by Inertial and Magnetic Sensing. 53(7):1346–1356.
- [Sahoo, 2015] Sahoo, S Subramanian, S. C. M. N. S. S. (2015). Design and development of a heading angle controller for an unmanned ground vehicle. *International Journal of Automotive Technology*, 16(1):27–37.
- [Savage, 1998] Savage, P. G. (1998). Strapdown Inertial Navigation Integration Algorithm Design Part 1: Attitude Algorithms. *Journal of Guidance, Control, and Dynamics*, 21(1):19–28.
- [Schell, 2005] Schell, B. (2005). 100 Years of Anschutz Gyro Compasses - 100 Years of Innovations in Nautical Technology. In *Symposium Gyro Technology*, number April, pages 1–20.
- [Shoemake1985, 1985] Shoemake1985, K. (1985). Animating rotations with quaternion curves. *Proc. SIGGRAPH*, 45(85):245–254.
- [Shuster and Oh, 1981] Shuster, M. D. and Oh, S. D. (1981). Three-Axis Attitude Determination from Vector Observation. *Journal of Guidance, Control, and Dynamics*, 4(1):70–77.
- [Taffoni et al., 2009] Taffoni, F., Focaroli, V., Formica, D., Iverson, J. M., Keller, F., and Gugliemelli, E. (2009). Sensor-based technology in the study of motor skills in infants at risk for ASD. *Proceedings of the 4th IEEE RAS/EMBS International Conference on Biomedical Robotics and Biomechatronics (BIOROB 2012)*, 24(3):1879–1883.

BIBLIOGRAPHY

151

- [Tedaldi et al., 2014] Tedaldi, D., Pretto, A., and Menegatti, E. (2014). A Robust and Easy to Implement Method for IMU Calibration without External Equipments. In *International Conference on Robotics and Automation (ICRA), 2014 IEEE*, pages 3042–3049.
- [Tian et al., 2013] Tian, Y., Wei, H., and Tan, J. (2013). An adaptive-gain complementary filter for real-time human motion tracking with MARG sensors in free-living environments. *IEEE Transactions on Neural Systems and Rehabilitation Engineering*, 21(2):254–264.
- [Titterton and Weston, 2005] Titterton, D. H. and Weston, J. L. (2005). *Strap-down Inertial Navigation Technology - 2nd Edition*.
- [TOUM,] TOUM. *The Other Understanding in Movement*. <http://www.toum.it/>.
- [VanMiddlesworth, 2015] VanMiddlesworth, M. Kaess, M. H. F. L. J. J. (2015). Mapping 3D Underwater Environments with Smoothed Submaps. *Springer Tracts in Advanced Robotics*, 105:17–30.
- [Vasconcelos et al., 2011] Vasconcelos, J. F., Elkaim, G., Silvestre, C., Oliveira, P., and Cardeira, B. (2011). Geometric approach to strapdown magnetometer calibration in sensor frame. *IEEE Transactions on Aerospace and Electronic Systems*, 47(2):1293–1306.
- [Vetexinc,] Vetexinc. *Vehicle Technologies Inc.* <http://www.vetexinc.com/>.
- [Vignais et al., 2013] Vignais, N., Miezal, M., Bleser, G., Mura, K., Gorecky, D., and Marin, F. (2013). Innovative system for real-time ergonomic feedback in industrial manufacturing. *Applied Ergonomics*, 44(4):566–574.
- [von Hofsten, 2004] von Hofsten, C. (2004). An action perspective on motor development. *TRENDS in Cognitive Sciences.*, 8(6).
- [von Hofsten and Rosander, 2012] von Hofsten, C. and Rosander, K. (2012). Perception-action in children with ASD. *Frontiers in Integrative Neuroscience*, 6(4):1–6.
- [Wada, 2005] Wada, M. (2005). Omnidirectional Control of a Four-wheel Drive Mobile Base for Wheelchairs.
- [Wahba, 1965] Wahba, G. (1965). A least-square estimate of spacecraft attitude. *SIAM Review*, (7):409.

- [Wakita et al., 2013] Wakita, K., Huang, J., Di, P., Sekiyama, K., and Fukuda, T. (2013). Human-Walking-Intention-Based Motion Control of an Omnidirectional-Type Cane Robot. *IEEE/ASME Transactions on Mechatronics*, 18(1):285–296.
- [Ward and Iagnemma, 2008] Ward, C. and Iagnemma, K. (2008). A Dynamic-Model-Based Wheel Slip Detector for Mobile Robots on Outdoor Terrain. *IEEE Transactions on Robotics*, 24(4):821–831.
- [Welch and Foxlin, 2002] Welch, G. and Foxlin, E. (2002). Motion Tracking: No Silver Bullet, but a Respectable Arsenal. (December):24–38.
- [Wu et al., 2005] Wu, G., van der Helm, F. C., (DirkJan) Veeger, H., Makhsous, M., Van Roy, P., Anglin, C., Nagels, J., Karduna, A. R., McQuade, K., Wang, X., Werner, F. W., and Buchholz, B. (2005). ISB recommendation on definitions of joint coordinate systems of various joints for the reporting of human joint motionPart II: shoulder, elbow, wrist and hand. *Journal of Biomechanics*, 38(5):981–992.
- [Yi et al., 2009] Yi, J., Wang, H., Zhang, J., Song, D., Jayasuriya, S., and Liu, J. (2009). Kinematic modeling and analysis of skid-steered mobile robots with applications to low-cost inertial measurement unit-based motion estimation. *IEEE Transactions on Robotics*, 25(5):1087–1097.
- [Yun and Bachmann, 2006] Yun, X. and Bachmann, E. R. (2006). Design , Implementation , and Experimental Results of a Quaternion-Based Kalman Filter for Human Body Motion Tracking. 22(6):1216–1227.
- [Zhang et al., 2012] Zhang, M., Lange, B., Chang, C.-Y., Sawchuk, A., and Rizzo, A. (2012). Beyond the standard clinical rating scales: fine-grained assessment of post-stroke motor functionality using wearable inertial sensors. *Conference proceedings : 34th Annual International Conference of the IEEE Engineering in Medicine and Biology Society. IEEE Engineering in Medicine and Biology Society. Conference*, 2012:6111–5.
- [Zhou and Hu, 2005] Zhou, H. and Hu, H. (2005). Kinematic model aided inertial motion tracking of human upper limb. In *Information Acquisition, 2005 IEEE International Conference on*, pages 150–155.
- [Zhou and Hu, 2008] Zhou, H. and Hu, H. (2008). Human motion tracking for rehabilitation—A survey. *Biomedical Signal Processing and Control*, 3(1):1–18.